Influence of river reconstruction at a bank filtration site - water quality field investigation and 3D modelling of groundwater flow and heat transport

Weishi Wang

Dissertation

for a doctoral degree "doctor rerum naturalium" (Dr. rer. nat.) in the scientific discipline Hydrogeology

Faculty of Science, University of Potsdam

Institue of Environmental Science and Geography

2021

First Supervisor: Prof. Dr. habil. Sascha Oswald

Second Supervisor: Prof. Dr. habil. Jan Fleckenstein

Reviewer: Prof. Dr. habil. Sascha Oswald

Prof. Dr. habil. Jan Fleckenstein

Prof. Dr.Thomas Grischek

Published online on the
Publication Server of the University of Potsdam:
https://doi.org/10.25932/publishup-49023
https://nbn-resolving.org/urn:nbn:de:kobv:517-opus4-490234

Contents

List of abbreviations

Abbreviation	Description
AOC	Assimilable organic carbon
BDOC	Biodegradable dissolved organic carbon
BF	Bank filtration
DO	Dissolved oxygen
DOC	Dissolved organic carbon
DOM	Dissolved organic matter
ETC	Electron trapping capacity
K	Hydraulic conductivity
LBF	Lake bank filtration
MAR	Managed aquifer recharge
ND	Nedlitzer Durchstich
NOM	Natural organic matter
POC	Particulate organic carbon
PS	polysaccharide
RBF	River bank filtration
SUVA	Specific ultraviolet absorbance
TOC	Total organic carbon

Abstract

Bank filtration is an effective water treatment technique and is widely adopted in Europe along major rivers.. It is the process where surface water penetrates the riverbed, flows through the aquifer, and then is extracted by near-bank production wells. By flowing in the subsurface flow passage, the water quality can be improved by a series of beneficial processes. Long-term riverbank filtration also produces colmation layers on the riverbed. The colmation layer may act as a bioactive zone that is governed by biochemical and physical processes owing to its enrichment of microbes and organic matter. Low permeability may strongly limit the surface water infiltration and further lead to a decreasing recoverable ratio of production wells.The removal of the colmation layer is therefore a trade-off between the treatment capacity and treatment efficiency. The goal of this Ph.D. thesis is to focus on the temporal and spatial change of the water quality and quantity along the flow path of a hydrogeological heterogeneous riverbank filtration site adjacent to an artificial-reconstructed (bottom excavation and bank reconstruction) canal in Potsdam, Germany.

To quantify the change of the infiltration rate, travel time distribution, and the thermal field brought by the canal reconstruction, a three-dimensional flow and heat transport model was created. This model has two scenarios, 1) 'with' canal reconstruction, and 2) 'without' canal reconstruction. Overall, the model calibration results of both water heads and temperatures matched those observed in the field study. In comparison to the model without reconstruction, the reconstruction model led to more water being infiltrated into the aquifer on that section, on average 521 m^3/d, which corresponded to around 9% of the total pumping rate. Subsurface travel-time distribution substantially shifted towards shorter travel times. Flow paths with travel times <200 days increased by ~10% and those with <300 days by 15%. Furthermore, the thermal distribution in the aquifer showed that the seasonal variation in the scenario with reconstruction reaches deeper and laterally propagates further.

By scatter plotting of $\delta^{18}O$ versus $\delta^{2}H$, the infiltrated river water could be differentiated from water flowing in the deep aquifer, which may contain remnant landside groundwater from further north. In contrast, the increase of river water contribution due to decolmation could be shown by piper plot. Geological heterogeneity caused a substantial spatial difference in redox zonation among different flow paths, both horizontally and vertically. Using the Wilcoxon rank test, the reconstruction changed the redox potential differently in observation wells. However, taking the small absolute concentration level, the change is also relatively minor. The treatment efficiency for both organic matter and inorganic matter is consistent after the reconstruction, except for ammonium. The inconsistent results for ammonium could be explained by changes in the Cation Exchange Capacity (CEC) in the newly paved riverbed.

Because the bed is new, it was not yet capable of keeping the newly produced ammonium by sorption and further led to the breakthrough of the ammonium plume. By estimation, the peak of the ammonium plume would reach the most distant observation well before February 2024, while the peaking concentration could be further dampened by sorption and diluted by the afterward low ammonium flow. The consistent DOC and SUVA level suggests that there was no clear preference for the organic matter removal along the flow path.

Zusammenfassung

Die Uferfiltration, eine wirksame Wasseraufbereitungstechnik, ist an Europas großen Flüssen weit verbreitet. Es bezieht sich dabei hauptsächlich auf einen Prozess, wobei das Oberflächenwasser in das Flussbett eindringt, durch den Grundwasserleiter fließt und schließlich durch ufernahe Brunnen gewonnen wird. Beim Einströmen in den unterirdischen Aquifer verbessert sich die Wasserqualität durch eine Reihe von vorteilhaften Reaktionen, die jedoch langfristig zum Auftreten von Kolmation des Flussbetts führen. Aufgrund der Anreicherung von Mikroben und organischen Substanzen bildet sich die Kolmationsschicht einerseits als bioaktive Zone für zahlreiche biochemische Reaktionen; andererseits kann ihre geringe Permeabilität die Infiltration von Oberflächenwasser behindern, welches zur Produktivitätseinschränkung von Brunnen führt. Daher ist das Entfernen der Kolmationsschicht immer ein Kompromiss zwischen Behandlungskapazität und Effizienz. Diese Doktorarbeit zielt darauf ab, die zeitlichen und räumlichen Veränderungen der Wasserqualität und -menge entlang des Fließwegs eines hydrogeologisch heterogenen Uferfiltrat-Standorts nahe einem baulich vertieften Kanal (Ausbaggerung und Ufersanierung) in Potsdam zu untersuchen.

Zur Quantifizierung der durch die Kanalvertiefung hervorgerufenen Änderung auf die Infiltrationsrate, die Laufzeitverteilung und das thermische Feld wurde ein dreidimensionales Strömungs- und Wärmetransportmodell mit zwei Modellszenarien (mit und ohne Baumaßnahmen) erstellt. Insgesamt stimmten die Kalibrierungsergebnisse der Wasserstände und der Temperaturen mit den Beobachtungen überein. Die Modellierungsergebnisse zweier Szenarien zeigten, dass durch die Vertiefung durchschnittlich 521 m^3/d, was etwa 9% der Gesamtpumprate entspricht, mehr Wasser in den Grundwasserleiter geflossen ist. Die unterirdische Fliesszeit verkürzte sich. Die Anzahl der Fliesswege mit Fliesszeiten <200 Tage erhöhten sich um ca. 10% und jene mit <300 Tage um 15%. Darüber hinaus breitete sich die Wärme im Grundwasserleiter tiefer und weiter im Modell mit Baumaßnahmen aus.

Mittels Streudiagrammen von $\delta^{18}O$ und $\delta^{2}H$ konnte das infiltrierte Flusswasser vom landseitigen Grundwasser unterschieden werden, während eine dekolmationsbedingte Erhöhung des Flusswasseranteils in Brunnen durch Piper-Diagramme nachgewiesen werden konnte. Die geologische Heterogenität verursachte erhebliche horizontale und vertikale Unterschiede in der Redox-Zonierung zwischen verschiedenen Strömungsbahnen. Das Redoxniveau verändert sich in verschiedenen Brunnen durch die Baumaßnahme. Die Behandlungseffizienz für organische und anorganische Stoffe blieb unabhänig von der Baumaßnahme erhalten, mit Ausnahme von Ammonium. Dies ist wohl auf die Änderung der Kationenaustauschkapazität im neu ausgebaggerten Flussbett zurückzuführen, das noch nicht

in der Lage war, neu entstehendes Ammonium zu absorbieren, was zu einem Fortschreiten der Ammonium-Fahne führt. Schätzungsweise erreicht das Maximum der Ammonium-Fahne den entferntesten Brunnen vor Februar 2024, wobei sich die Konzentration durch Sorption und Vermischung mit nachströmendem Wassser verringern sollte. Das gleichbleibende DOC- und SUVA-Niveau deutete darauf hin, dass es keine Bevorzugung beim Abbau organischer Substanzen entlang des Fließwegs gab.

Chapter 1 Introduction and Motivation

1.1 The history of bank filtration and current application around the world

Groundwater is specified as the water exists below the land surface. Groundwater holds approximately one-third of the total global freshwater and acts as the 'planet's largest reservoir' (Giordano, 2009; Tuinhof and Heederik, 2002). Groundwater is estimated to be the drinking water source for 1.5 to 3 billion people due to it's stability with regards to changing weather patterns and it carrying less pollution (Holley et al., 2016; Kundzewicz and Döll, 2009). Gleeson et al. (2012) estimated that 1.7 billion people are facing groundwater availability related issues. Due to an increasing demand and exploration rate, an aggregate deficiency of the groundwater resources has been observed globally. Estimated by Döll et al. (2014), the groundwater depletion has been doubled from 1960 to 2000, while from the year 2000-2009, 15% of abstracted groundwater was non-renewable. Over-pumped groundwater could not be recharged in time which creates further troubles in water table recovery. Additionally, the sinking groundwater table may cause calamitous consequences on hydrological- and eco-system (Casanova et al., 2016; Wada et al., 2010).

Aquifer recharge is of significant influence on the aquifer storage. Natural aquifer recharge may be influenced by the seasonal and climatic change, and limited by its capacity (Tuinhof and Heederik, 2002). Artificial recharge enhancement could be an excellent option to increase the groundwater infiltration and further replenish the aquifer (Casanova et al., 2016). Dillon (2005) described Management of aquifer recharge (MAR also known as Managed Aquifer Recharge) as " Intentional banking and treatment of water in aquifers." Tuinhof and Heederik (2002) mentioned the whole process as "Management of Aquifer Recharge and Subsurface Storage (MAR-SSS)." Other names could also be found in other studies like "soil aquifer treatment" (Schijven, 2002). MAR is a technique featuring as a predetermined artificial recharge to aquifers aiming at consecutive recovery (Dillon et al., 2010). Tuinhof and Heederik (2002) listed the different methods with actual projects around the world besides a detailed explanation. Dillon (2005) further added a graphic illustration on some of the main processes. Casanova (2016) later categorized the MAR techniques by the difference in the way of recharge, which are separately: 1) Infiltration Methods, 2) Direct Injection method, and 3) Filtration method. Riverbank Filtration (RBF) is an induced recharge method and categorized as the primary technique in filtration. It is typically applied when the surface water is not qualified for direct water supply (Dillon et al., 2002; Mustafa et al., 2016).

"Surface water, penetrating the river bed and further proceeding to the aquifer either driven by natural or high capacity pumping wells of a certain distance from the waterbody, was

called riverbank filtrate (RBF)" (Abdel-Lah, 2013; Dillon, 2005; Hiscock and Grischek, 2002; Kuehn and Mueller, 2000; Ulrich et al., 2015a). Functioning as natural reactive barrier, bank filtration improves the raw water quality via physical, biological, geochemical and hydrogeological processes of different turnover rates, results into the recovered water of higher and more stable quality (Dillon et al., 2002; Gross-Wittke et al., 2010; Mustafa et al., 2016). RBF was firstly adopted in Glasgow Waterworks, the UK, in 1810 on the river Clyde (Ray et al., 2003), but it was used centuries before and unnamed (Kuehn and Mueller, 2000). In 1892, Robert Koch found that with the same water source from the Elbe river, the city of Altona showed a lower incidence of Cholera than Hamburg simply by water filtration process (Ray, 2002a). This resulted in the adoption of RBF as either a replacement or a supplement process in the drinking water industry (Ray et al., 2003).

Figure. 1.1 is a schematic of the RBF process. Hiscock and Grischek (2002) concluded the possible side effect of RBF as the dissolution of iron and manganese concentrations, the formation of hydrogen sulfide and other malodorous sulfur compounds driven by redox-reactions. In the following subsections international applications of RBF will be described.

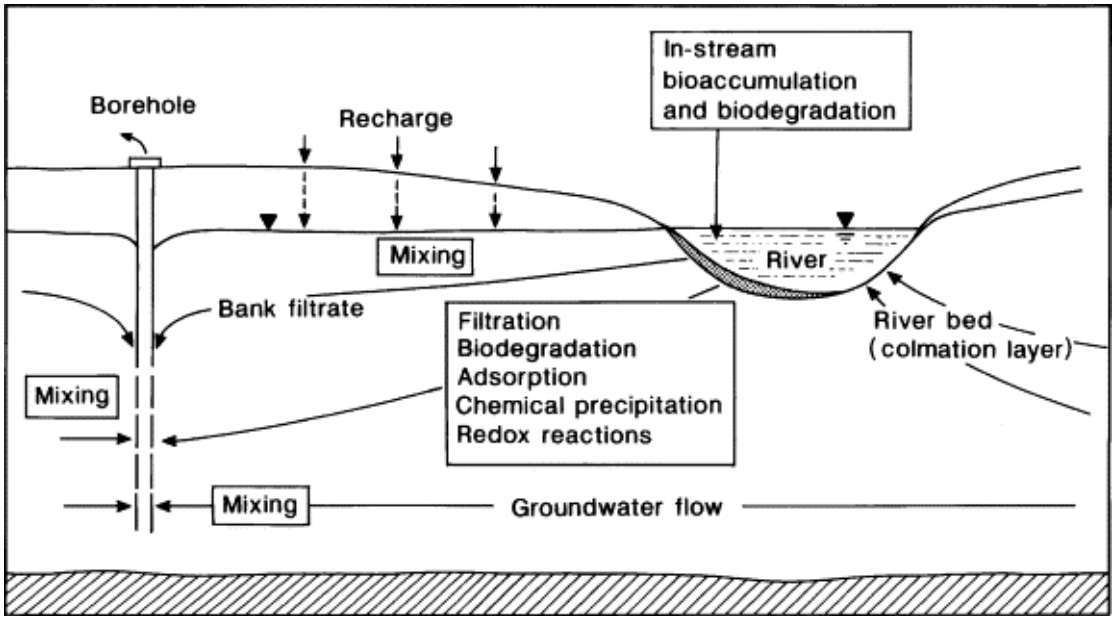

Figure.1.1 The bank filtration processes that will affect the water quality, adopted from Hiscock and Grischek (2002).

1.1.1 In Europe

In Europe, RBF works as the cheapest, most efficient technique and has been widely applied in the past decades (Polomčić et al., 2013; Ray, 2008; Ray et al., 2003). Historically RBF has been used without further treatment (Kuehn and Mueller, 2000), (e.g., in the Lower Rhine region during the period of 1870-1950 (Schubert, 2002)). Currently RBF works as an effective pre-treatment method (Hiscock and Grischek, 2002) and has provided 50% of

potable water in the Slovak Republic, 45% in Hungary, 5% in the Netherland, and 16% in Germany. Locally, RBF could act as the main technique and is already common in some areas (e.g., in Berlin, RBF contributes 75% of drinking water). For cities along major rivers in Europe, RBF was taken as the prime treatment method for drinking water supply (Ray, 2002b) and has been used along the Elbe (Fukada et al., 2003; Grischek et al., 1998; Grischek and Paufler, 2017),the Oder (Massmann et al., 2004, 2003a), the Rhine (Schubert, 2002; Sharma et al., 2012), and along the Danube (Fiedler et al., 2018). Lake filtration is also well adopted in Germany. Intensive investigations have been carried out at the Lake Tegel (Gross-Wittke et al., 2010; Grünheid et al., 2005; Henzler et al., 2016, 2014; Maeng et al., 2010; Massmann et al., 2008b) and lake Wannsee (Kohfahl et al., 2008; Massmann et al., 2008b, 2008a).

1.1.2 In the US

In the US, the use of RBF was also adopted approximately 70 years ago for drinking water supply (Ray, 2002a; Ray et al., 2003). Not as popular as its broad application in Europe, RBF was taken as a possible low-cost alternative or supplement technique for pathogen removal in the US (Ray et al., 2003), especially for cysts and oocysts, followed by a decrease of turbidity and DOC (Grünheid et al., 2005). Regulated to "the Interim Enhance Surface Water Treatment Rule" (US Environmental Protection Agency, 1998), the concept of 'groundwater under the direct influence of surface water' (GWUDISW, aka GWUDI) was introduced in RBF system (Sheets et al., 2002). Evaluated by microscopic particulate analysis method (US Environmental Protection Agency, 1992), groundwater at the risk of being exposed to the surface water born pathogen would be categorized as GWUDI (Ray, 2002a; Sheets et al., 2002). Once the RBF system is defined as GWUDI, the following water treatment process would be required the same as for surface water (Sheets et al., 2002). RBF system excluded from GWUDI would also be required with further assessment for pathogen and chemical breakthrough during high flow periods (Ray, 2002a). Investigations in the US have also been applied along major rivers, e.g., the Great Miami River (Sheets et al., 2002), the Illinois River (Ray, 2004, 2002b).

1.1.3 In Asia

Asia has many cities with higher population densities than in Europe or the US (Ray, 2008). RBF has been used with less popularity in Asia as it is in developed countries (Hu et al., 2016). In South Korea, even with a thinner alluvial aquifer, RBF has also been used as a cost-effective method (Ray, 2008). RBF has been used since 2001 on the Han river (Lee and Lee, 2010), and investigations have also been carried out along the river Nakdong (Kwon, 2015a; Lee et al., 2009). Countries with very high population, such as India and China, both of them are facing a water crisis due to the drastic declining groundwater table. As a vital source,

groundwater takes up 18.3% of total water supply in China (Hu et al., 2016) and, separately, 65% of irrigation water, 85% of domestic water supply in India (Livingston, 2009). Taking into consideration both the quantity and quality, RBF is an excellent alternative technique and further direction. In China, since the first application RBF site in the 1930s, 300 RBF sites have been on operation in the 2000s (Hu et al., 2016). Investigations have been carried along the Kuihe river (Wang et al., 2007; Wu et al., 2007), the Liao river (Su et al., 2018, 2017) and other places (Pan et al., 2018; Wang et al., 2016). However, Hu et al. (2016) stated that RBF in China is still in the early stages, and further studies would be necessary. Similar to China, RBF has been adopted in India (Ray, 2008). The potential sites and application of RBF have been well described in the study of Sandhu et al. (2011a). A survey by Sandhu et al. (2019) demonstrated water quality improvement among existing RBF sites in India motivating it's use at potential new sites. Further investigations have been applied in the Ganga River (Sandhu et al., 2011b; Ojha et al., 2013), along Yamuna River (Groeschke et al., 2017; Singh et al., 2010), along Alaknanda river (Gupta et al., 2015; Sharma et al., 2014) and other places (Dash et al., 2008).

In countries in southeast Asia, even with the surface water as the primary water resource, the increasing water demand and pollution also drove a growing interest in using RBF. In Thailand, investigations have been carried out along the Ping River (Archwichai et al., 2015; Srisuk et al., 2012), and in Malaysia, the research activities have been directed towards water quality improvement (Abd Rashid et al., 2015; Othman et al., 2015; Shamsuddin et al., 2014) and estimation of travel times (Mustafa et al., 2016).

1.1.4 Other studies around the world

In Africa, RBF is still at the initial phase of its development (Umar et al., 2017). Investigations are mainly focused in Egypt along the River Nile (Shamrukh and Abdel-Wahab, 2011, 2008), while projects are also set up in Jordan (Umar et al., 2017). Recent investigations (Ghodeif et al., 2018; Paufler et al., 2018) showed a newly set-up RBF site and its quality improvement in its beginning stage. Feasibility assessment has also been done in Malawi and Kenya according to the review by Sharma and Amy (2009). In South America, studies of an LBF (Lake bank filtration) site (Romero-Esquivel et al., 2017; Romero et al., 2014) have been carried out with a focus on the water quality improvement and cyanobacteria removal. A study by Blavier et al. (2014) in Bolivia was adopted to predict the exploration quantity and the treated water quality. In Australia, Dillon et al. (2002) has also carried out RBF related investigations, while more studies are about the MAR system.

1.2 Water Quality Improvement by Riverbank Filtration

As a combined effect of different processes, Ray et al. (2002a) summarized the water quality improvement process as "physical filtering, microbial degradation, ion exchange, precipitation, sorption, and dilution." Sharma and Amy (2009) further added the more general "complexation and redox reaction." The beneficial attenuation processes mainly act on suspended solids, biodegradable compounds, other DOC or bacteria, viruses, parasites (Hiscock and Grischek, 2002), pharmaceuticals (Bradley et al., 2014; Drewes et al., 2003; Heberer et al., 2004; Massmann et al., 2006), pesticides (Ray et al., 2002b), residues of explosives (Zheng et al., 2009), etc.

1.2.1 Microbe removal during Riverbank Filtration

Surface water contains different pathogenic microorganisms from wastewater discharge or surface run-off (Schijven, 2002; Tufenkji et al., 2002), while subsurface media might also carry them (Ray et al., 2002a). A significant function and the impetus of RBF is the removal of pathogens, including bacteria, viruses, protozoa (Ray et al., 2002a), cyanobacteria and cyanotoxins (Romero et al., 2014). Along the flow paths, the microorganisms can attach to porous medium and get deactivated prior to arriving at the pumping well. Additionally the microorganisms are subject to little detachment rate and relatively slow groundwater flow (Schijven et al., 2003). Schijven et al. (2003) articulated various processes of this inactivation, straining, and sedimentation in pores. Dilution by pristine groundwater, diffusion, and dispersion might also contribute to decreasing the concentration, albeit not removal. RBF is a site-specific process with multi influential factors and therefore there is a lack of protocol on assessing the removal efficiency of pathogenic microorganisms (Tufenkji et al., 2002).

Field studies have been performered around the world focusing on different pathogenic species. Virus removal by soil passage is the best understood process of removing pathogenic species through Schijven and Hassanizadeh (2000). However the removal efficiency varies with many influential factors, including 1) subsurface structure (composition, heterogeneity, etc.), 2) environmental condition (e.g., DOC concentration, pH, temperature, etc.), and 3) virus type (isoelectric point, hydrophobicity, size, shape, and structure, etc.) (Keswick and Gerba, 1980; Schijven, 2002; Schijven and Hassanizadeh, 2000). Three RBF sites in the USA showed a removal rate of more than two log-units for Male-specific Bacterio-phage and more than four log-units for somatic Bacterio-phage within a similar distance (Weiss et al., 2005). Bacterial removal strongly depends on the material properties of the soil passage, and coarse-grained aquifer might perform poorly in bacteria removal (Schijven et al., 2003). Field observation investigations are consistent with this conclusion. In India, surface water could be highly contaminated by bacteria, while the removal efficiency of total coliform bacteria could vary from 1.3 to 5 log-unit (Cady et al., 2013; Dash et al., 2010, 2008; Sandhu et al., 2011b)

regardless of the influence from monsoons. Harvested water may still show much higher bacterial concentration than the drinking water standard and need further treatment (Singh et al., 2010). It is believed that the process of the protozoa removal is comparable with the removal of virus, however, to a different extent (Schijven and Hassanizadeh, 2000). The main concern of pathogenetic protozoans would be Cryptosporidium and Giardia, which threaten human health the most (Schijven and Hassanizadeh, 2000). However, they are generally with a much lower concentration than other microorganisms in surface water. Direct sampling results of protozoa before the year 2002 have been reviewed by Berger (2002) for the recorded outbreak of protozoa. Schijven et al. (2003) listed the microbial occurrence from four large RBF sites in the USA from the information supported by ICR (Information Collection Rule), in which no Cryptosporidium was found, while positive samples were found both for Giardia and Enterovirus albeit the occurrence is low.

1.2.2 NOM

Natural Organic Matter (NOM) is often used as a synonym of Total Organic Carbon (TOC), given the typical insignificant share of the organic contaminants (Leenheer and Croué, 2003). NOM can also be categorized into different subgroups. It consists of dissolved and particulate, humic, and nonhumic organic matters (Tufenkji et al., 2002). Filtered by a membrane with a pore size of 0.45 micrometer, the retained part is called as particulate organic carbon (POC), while the fraction which goes through is called as dissolved organic carbon (DOC) (Leenheer and Croué, 2003). It could also be subdivided as a biodegradable fraction and a refractory fraction, and the biodegradable organic matter (BOM) are mainly measured by the AOC bioassay and BDOC assay (Escobar and Randall, 2001).

The removal efficiency of NOM is also site-specific. Based on previous studies, Greskowiak et al. (2005) summarized that the removal rate of the DOC is about 30 – 50% in the first decimeters of the subsurface passage. However, the decrease of DOC could be as low as 10 - 20%, e.g., (Ludwig et al., 1997; Romero-Esquivel et al., 2017). As a general mixture, the degradation efficiency among different components in DOC also varies. Using liquid chromatography with organic carbon detection (LC-OCD), Grünheid et al. (2005) found that the polysaccharide (PS) showed the highest degradation efficiency, while low molecular weight acids, humic substances, and its building blocks only degraded partially. Another conclusion by Grünheid et al (2005) based on the specific UV absorbance (SUVA) is that the consumption of aliphatic hydrocarbons are prioritized under aerobic conditions, while aromatic and double-bond structures are preferentially used under the anaerobic condition. A similar result was also observed in an earlier study about the Soil-aquifer Treatment (SAT) field in the USA in the vertical direction (Drewes and Fox, 1999). Sorted with different molecular weight, Sontheimer (1991) reported that after RBF treatment, 70% of the DOC

with the molecular weight between 800-1500 g/mol was removed. However study by (Ludwig et al., 1997) showed that along the flow path, the proportion of larger molecular weight (>10000 g/mol) shrank the most in the composition of DOC, while the fraction of middle molecular weight (1000-10000 g/mol) remained stable.

During the chlorine-used disinfection process NOM could form halogenated disinfection by-products (DBPs) (Singer, 1999). When the disinfection method includes ozone the oxidation by-product could contribute to the regrowth of microorganism and biofilm (Singer, 1999). DBPs have potential genotoxicity and carcinogenicity (Richardson et al., 2007) therefore the removal efficiency of NOM in RBF is a significant concern. Specific ultraviolet absorbance (SUVA) is easily measured and widely adopted as a surrogate for forecasting the formation potential of DBPs (Hua et al., 2015; Singer, 1999). It is defined as the ratio between the UV absorbance at 254 nm and the DOC concentration (Leenheer and Croué, 2003). Higher SUVA value indicates a larger portion of aromatic compounds in the DOC, which is in general thought as the primary precursor for DBPs (Leenheer and Croué, 2003; Singer, 1999). During the RBF process, the changing of the SUVA value is very much site-specific. The decrease was shown in the Lagoa do Peri in Brasil (from 2.3 ± 0.2 to 1.9 ± 0.8 L/(mg·m)) (Romero-Esquivel et al., 2017) and the River Thames in England (Ascott et al., 2016). An increase has been found in the South Platte River in Colorado, USA (from 1.6–2.0 L/(mg·m) to 2.0–2.6 L/(mg·m)) (Regnery et al., 2015) and the Cedar River in Iowa, USA (Hoppe-Jones et al., 2010). Constant SUVA values have been observed in the Mathura section of the River Yamuna in India (Singh et al., 2010). Redox condition could also be an influential factor on the SUVA value, as different investigations (Drewes and Fox, 1999; Grünheid et al., 2005) have observed an initial increase in the oxic zone and further decreased in the anoxic soil passage. This initial increase and then decrease was explained via the preferential consumption of aliphatic carbon during the aerobic zone, and aromatic and double-bond structures were more involved in the reaction in the anaerobic zone.

Removal of organic micropollutants (OMP) is also a beneficial effect by the treatment process of RBF. Studies on OMPs includes pharmaceutical residues, endocrine disruptor, personal care products (PPCPs), and household chemicals (Hoppe-Jones et al., 2010). By the increasing accuracy of the analytical method and equipment, the detection limit could reach lower than 1µg/l (Grünheid et al., 2005). Since the 1990s, pharmaceuticals have been detected in the aquatic environment (Löffler et al., 2005), and studies have shown that bank filtration could degrade some of the pharmaceutical residues as well as other micropollutants (Grünheid et al., 2005; Hamann et al., 2016; Henzler et al., 2014; Maeng et al., 2010). Studies on pharmaceutical residues mainly focused on the influential factors, e.g., redox condition (Drewes et al., 2003; Kovačević et al., 2017; Massmann et al., 2006), traveling distance

(Bradley et al., 2014; van Driezum et al., 2019), temperature (Maeng et al., 2010; Regnery et al., 2015), and hydrological events (Ray et al., 2002b). Besides pharmaceutical residues, other studies vary by the difference of the local focus, e.g., herbicide (Ray et al., 2002b), explosive chemicals (Zheng et al., 2009) and organophosphates (Stepien et al., 2013).

1.2.3 Temperature

RBF can also change the temperature of harvested water which is considered as a benefit. Surface water temperature has great diurnal and seasonal variation. Seasonally the sinusoidal pattern peaks in summer, bottoms in winter, while the diurnal temperature is mainly high in the daytime and low at night. For groundwater in a shallow aquifer (depth of 10-20 m), the temperature, in general, would be relatively stable and 1 °C to 2 °C higher than the local mean annual air temperature (Domenico and Schwartz, 1998). At a bank filtration site, the downward component of infiltrating river water brings the cyclic temperature signal to a greater depth (Kalbus et al., 2006). However, further along the traveling path, both the diurnal and the seasonal temperature pattern would be flattened and finally equals the environment temperature in the shallow aquifer. Most RBF sites are at depths of the shallow aquifers thus the water harvested from pumping wells would become stable and slightly higher than the annual mean temperature. Taking the site in this research as an example, the infiltrated water sampled close to the pumping wells is stable at around 11.2 °C. Even further treatment and distribution process will influence the final result, it still alleviates the seasonal dynamics and supplies cool water source in summer and relatively warm water in winter.

1.3 Redox reactions and redox zonation

Functioning as a reactive barrier, bank filtration improves the raw water quality via the biological, geochemical and hydrogeological processes of different turnover rate (Gross-Wittke et al., 2010). Redox reactions are primarily driven by the consumption of NOM, mediated by the microbiological activities, and couple the most efficient electron donors and acceptors (Domenico and Schwartz, 1998; Kedziorek and Bourg, 2009; Massmann et al., 2004). Along with the redox reaction, the electron acceptor can change due to the consumption of oxygen and further lead to the formation of redox zonation (Massmann et al., 2008a). However, displeasing consequences might also arise along with the flow path, such as dissolved manganese concentration (Hiscock, 2005). As it is shown in Fig. 1.2, in closed groundwater system, the electron acceptors for the redox reaction of organic matter would follow a sequence of O_2, NO_3^-, Mn(IV), Fe(III), SO_4^{2-}, CO_2 by the energy yield from high to low (Champ et al., 1979; Chapelle, 2001; Robert A. Berner, 1981).

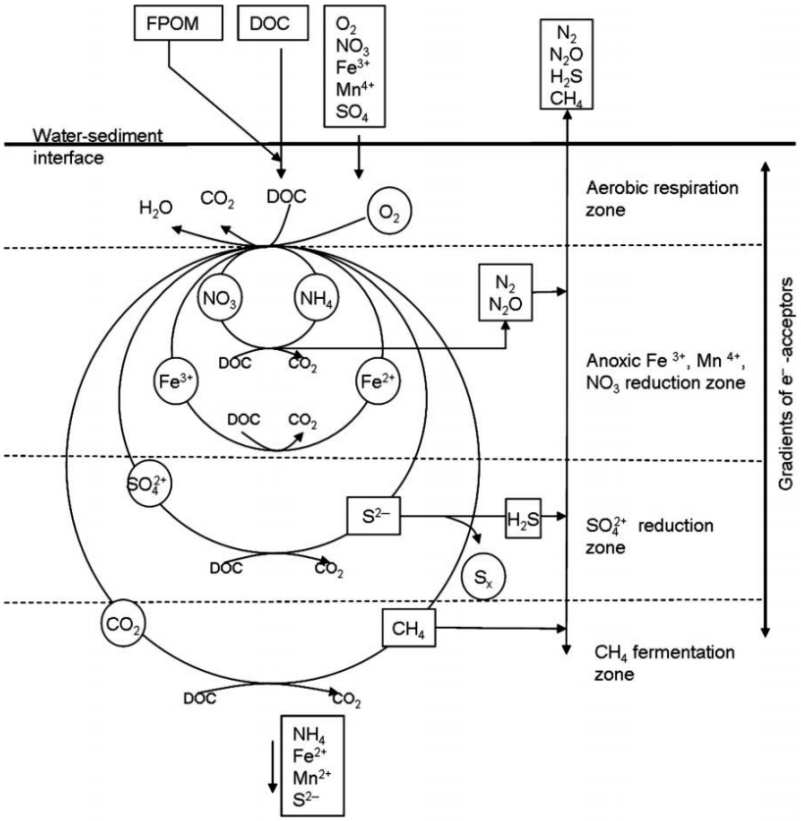

Figure. 1.2 Schematic display on redox processes in the RBF site of a closed system (Andreae et al., 1991; Gross-Wittke et al., 2010).

As shown in Fig. 1.2, along with the gradients of e^- acceptors, the redox zone could be categorized as i) aerobic respiration zone, ii) anoxic Fe^{3+}, Mn^{4+}, NO_3^- reduction zone, iii) SO_4^{2+} reduction zone and iv) CH_4 fermentation zone. Another study by Champ et al. (1979) categorized the redox zonation as 1) oxygen-nitrate, 2) iron-manganese, 3) the sulfate reduction zone, and 4) the methane fermentation zone. Kedziorek and Bourg (2009) listed the table in their research and added the number of electrons involved per atom or molecule (Table 1.1). Simultaneous reaction on different electron acceptors could happen as well. For example, nitrate and manganese (Bourg and Bertin, 1994; Oren et al., 2007) and iron and manganese (Massmann et al., 2004). Thus the border for these redox zones is also not a clear-cut (Massmann et al., 2004). In RBF, the stratification of redox zonation could happen not only in the horizontal direction but also in the vertical, e.g., a study of an RBF site at Lake Wannsee in Berlin showed a vertical stratification of redox zonation and was strongly influenced by the temperature change (Massmann et al., 2008a).

Table 1.1 Successive order of electron acceptors in RBF (adopted from Kedziorek and Bourg, 2009).

Processes	Reaction	Electrons involved
Respiration	$CH_2O + O_2 \rightarrow CO_2 + H_2O$	4
Denitrification	$\frac{5}{4}CH_2O + NO_3^- + H^+ \rightarrow \frac{5}{4}CO_2 + \frac{1}{2}N_2 + \frac{7}{4}H_2O$	5
Mn reduction	$\frac{1}{2}CH_2O + MnO_2(S) + H^+ \rightarrow Mn^{2+} + \frac{3}{2}H_2O + \frac{1}{2}CO_2$	2
Fe reduction	$\frac{1}{4}CH_2O + 2H^+ + Fe(OH)_3(S) \rightarrow Fe^{2+} + \frac{11}{4}H_2O + \frac{1}{4}CO_2$	1
Sulfate reduction	$2CH_2O + SO_4^{2-} + H^+ \rightarrow HS^- + 2CO_2 + 2H_2O$	8

1.3.1 Temperature effect on redox zonation

Temperature is a crucial factor controlling redox reactions and enzyme activity, while its variation range is essential in monitoring of the RBF site (Maeng et al., 2010; Miettinen et al., 1996; Umar et al., 2017). Fed by heating and cooling of surface water, the downward component of infiltrating river water brings the seasonal temperature signal to a greater depth (Kalbus et al., 2006). Besides the short-term fluctuations of the daily temperature signal in the stream bed itself (e.g., Munz & Schmidt 2017), seasonal temperature changes strongly affect the bioactivity of microorganism and show an impact on redox conditions (Massmann et al. 2008).

Some investigations have demonstrated that there is a temperature threshold on bioreaction. Temperature thresholded bioreaction means that when the environment temperature is below the threshold the bioreaction will be strongly constrained. Bourg and Bertin (1994) found in their study that the temperature needs to be above 10 °C to trigger the solubility of Mn. Investigations at other sites (Massmann et al., 2008a, 2006; Prommer and Stuyfzand, 2005) have shown that when the temperature falls below 14 °C, the biodegradation is greatly constrained. Miettinen et al. (1996) studied an RBF site of Finland demonstrating that enzyme activities decreased by the influence of seasonal temperature along the transect of the flow path to a groundwater production well.

The seasonal temperature cycle can also lead to the corresponding dimensional changes in the redox zonation; however, the variation range could be of distinct difference. An extreme case has been observed at an artificial recharge site (Massmann et al., 2006), where the aerobic condition predominated between the river and the pumping well in winter, while in summertime the oxygen was consumed as electron acceptor within the first meter below the river bottom and followed by the prevailing anaerobic condition. A similar result has been observed at an RBF site along the Rhine river (Sharma et al., 2012). In the other direction, the oxic zone could be limited to a very narrow range. A study by Massmann et al. (2004) showed that even with the traveling time of less than one day, there is still no DO and nitrate

observed in the observation wells, which suggested the oxic zone is limited to the short depth below the river bed and short distance to the waterbody. Other studies (Kedziorek et al., 2008; Su et al., 2018) have also observed the seasonal dynamic of the redox zones, while the variation is between the abovementioned two extreme cases.

1.3.2 Electron donors (POC and DOC)

The biological reaction includes the elimination of biodegradable compounds in both particulate (POC) and dissolved (DOC) form (Brugger et al., 2001) and strongly depends on the redox condition and temperature (Gross-Wittke et al., 2010). The traveling time is strongly influential on the degradation of NOM and can be site-specific. Sontheimer (1980) demonstrated that the decrease of DOC level with the increase of traveling time along the Rhine river in three different water utilities. Miettinen et al. (1994) demonstrated that for a Finnish waterworks, the long infiltration path resulted in a much larger declining TOC and chemical oxygen demand (COD) compared with shorter infiltration paths. Along one traveling path, Ludwig et al. (1997) showed that the two-thirds of the decrease in DOC happened in the first few meters. Schubert (1992) demonstrated that the DOC level below the riverbed (0.6 m below) is similar to the sample taken from observation wells adjacent to the harvest wells. A possible explanation could be that, after investigating the research field under different redox conditions, the anoxic-anaerobic condition showed slower DOC mineralization along the whole flowing process. In contrast, the oxic condition is observed to have an intensified removal in the beginning but will plateau along the rest process of flowing (Jekel and Gruenheid, 2005). The purification is not only along the horizontal flow but also effective in the vertical direction (Drewes and Fox, 1999; Wang et al., 2007).

Particulate organic carbon (POC) has been suggested as the extra electron donor to explain the massive consumption of the electron acceptors (Doussan et al., 1997; Grischek et al., 1998). For POC, both hydrolysis and solubilization would be required before it is utilized as the electron donor by the microorganism in the redox zonation (Doussan et al., 1997). POC could be attributed to the infiltrated surface water, the riverbed sediment, and the aquifer matrix (Grischek et al., 1998; Hoppe-Jones et al., 2010). The same results have been shown in other studies, e.g., (Grünheid et al., 2005; Hoppe-Jones et al., 2010; Romero-Esquivel et al., 2017). For the contributing ratio between POC and DOC, Kedziorek et al. (2008) demonstrated via modeling that the share of POC in the redox reaction increased with the traveling distance. However, Brugger et al. (2001) found that the POC is the primary electron contributor instead of DOC even within the riparian zone. So far, there is no concrete conclusion on the preference of the electron donor in the redox reaction. Greskowiak et al. (2005) showed that the POC could be preferred over DOC when it was highly degradable for

the redox reaction. A similar conclusion was summarized by Kedziorek et al. (2008), in which the remaining part of the DOC after the long traveling time was less degradable than the POC. As an essential source of electron donor, the limitation of POC availability could also be risky for the removal of nitrate (Grischek et al., 1998).

1.4 Influence of hydraulic connection on Riverbank Filtration performance

The hydraulic connection between the river and the flow field in the RBF site is a decisive factor influencing the treatment efficiency. Hiscock (2005) categorized the main treatment processes of RBF into two spatial zones: 1) the colmation layer with great biological activity but relative short residence time and 2) the flow path to the harvest wells with lower degradation ability but longer traveling time. Together they control the infiltration rate from the surface water, the dilution effect of the origin groundwater, the traveling time, and further the temperature propagation and bioreactions. The colmation layer is predominately mediated by the clogging and declogging effect. The preceeding flow path is influenced by the hydrogeological heterogeneity. The following literature review is presented in order of 1) clogging; 2) declogging; 3) hydrogeological heterogeneity.

1.4.1 Influence from riverbed clogging

The ideal riverbed should reach a balance between the optimal infiltration rate to the aquifer and the retardation of the pathogen transport (Ray, 2002b)). This has not yet been described adequately via physical parameterization. Riverbed structure could be decided by the local geological conditions, physical attributes of the sediment, the river flow velocity, and the infiltration velocity (Cunningham et al., 1987; Wett et al., 2002). Riverbed structure is a controlling factor that influences the RBF treatment capacity (Hiscock, 2005). Clogging is a sensitive factor on the RBF site as it works on other filters (Gutiérrez et al., 2018). As an essential source of uncertainty for site planning (Schubert, 2006), clogging is almost inevitable during the long-lasting operation of bank filtration, which would also strongly influence the sustainability of the RBF site (Zhang et al., 2011). Clogging would decrease the riverbed hydraulic conductivity and then lead to a more sluggish surface water infiltration and a decreasing recoverable ratio of production wells (Ulrich et al. 2015; Farnsworth & Hering 2011; Grischek & Bartak 2016; Schubert 2002; Massmann et al. 2008). Taking the RBF site in Düsseldorf as an example, a colmation layer of 10 cm thickness was found in the riverbed, containing iron, manganese, copper, zinc, lead and mineral oil (Wilderer et al., 2013). Another example of the riverbed sediment core samples in Lille, France, showed that the iron oxides were up to 5 percent and that remobilization could occur (Bourg et al., 1989). Clogging happens both on the riverbed surface and the deeper internal space of the porous media (Gutiérrez et al., 2018). The external clogging forms on the interface between the

aquifer and the surface water, while the internal clogging happens when fine particles infiltrate get stuck in the deeper interstitial space (Du et al., 2014; Gutiérrez et al., 2018; Schälchli, 1992; Wett et al., 2002). There are four clogging mechanisms involved in building up the colmation layer: physical, mechanical, chemical, and biological (Gutiérrez et al., 2018). They made a general review on the studies focusing on the different mechanism and summarized the factors showed an influence on the clogging process, although in practice, the clear distinguish among those clogging types is still under researching (Ulrich et al., 2015b). Ulrich et al. (2015) demonstrated that at an RBF site in Sonoma county, California, US, the biotic process contributed more in the clogging process than any abiotic process. Another study in the US showed the clogging might be more regulated by the degradation of the aquatic vegetation in comparison to other factors (Goldschneider et al., 2007).

Increases in clogging lead to the decrease of hydraulic conductivity in the riverbed. Field studies have investigated the thickness of the clogging layer and its small hydraulic conductivity compared with the aquifer, however, the time scale for the clogging is hard to summarize. Investigation on two cross-sections of the Danube river showed that the riverbed sediment thickness varies between 5 cm to 20 cm, while the hydraulic conductivity is around two orders of magnitude smaller than the K-value of aquifer sediment (Battin and Sengschmitt, 1999). Another field study by Thullner et al. (2002) demonstrated that the hydraulic conductivity in the clogging layer decreased by at least two orders of magnitude. In an artificial pond, Greskowiak et al. (2005) demonstrated that a clogging layer decreased the surface water infiltration rate from 3 m/d to 0.3 m/d. A later study by Hoffmann and Gunkel (2011) also showed the hydraulic conductivity on the top 2 cm was up to two orders of magnitude lower than the previous measurement. Lab investigations allow the investigation of the temporal dimension in the clogging process. Schälchli (1992) demonstrated in their flume experiment that the hydraulic conductivity of the top layer with 0.15 m depth decreased by one order of magnitude after 100 hours, while there was little to no change along the rest of river bed. The similar result displayed in the study of biological clogging by Vandevivere and Baveye (1992), that after introducing the glucose and bacteria from the top, the hydraulic conductivity dropped by almost two orders of magnitude in four days in the first 3 mm, however the hydraulic conductivity dropped by much smaller amounts at lower depths. Engesgaard et al. (2006) also showed the decrease of hydraulic conductivity by the two orders of magnitude in eight days and ended up with a reduction of more than three orders of magnitude in 40 days. In summary, the clogging on the top few decimetres has a hydraulic conductivity decrease by one to three orders of magnitude, and the formation of the top layer clogging needs days or even tens of days.

1.4.2 Influence from declogging

Although clogging is not a desirable process for the RBF water quantity, it is beneficial for water quality improvement. The bioactive clogging layer is rich in organic material and is the first place where the degradation and adsorption occurs. It is essential for the purification process (Hiscock, 2005; Romero et al., 2014; Schubert, 2006). Most research on the declogging process has been focused on improving the infiltration rate and possible change in treatment efficiency. The clogging layer can be partly removed by flood events or natural flow, restoring higher riverbed hydraulic conductivity (Gutiérrez et al., 2018; Levy et al., 2011). The field investigation by Mutiti and Levy (2010), demonstrated storm events could increase the hydraulic conductivity maximally by one order of magnitude, however this is still smaller than increases in hydraulic conductivity at the sand filtration system. Another field study (Gollnitz et al., 2004) suggested that scouring would not influence the water quality in the harvest well. Levy et al. (2011) demonstrated in the same location, that a total height of 0.42 m sediment removal in seven months, and the maximum increase on hydraulic conductivity was only 50%. An RBF field along the Thames river in the United Kingdom, demonstrated that the water quality worsened due to flooding and inundation events and that the recovery of the treatment ability took approximately six weeks (Ascott et al., 2016). Another investigation at an RBF site along the Danube river in Austria, demonstrated that a flooding event drove larger riverine bacteria into the groundwater system compared with normal discharge conditions but this did not influence a closeby (550m) pumping well (van Driezum et al., 2018). Berger (2002) described that in the flooding period, the removal rate of protozoa is lowerdue to the scouring effect. A laboratory study by Gutiérrez et al. (2018) showed that under a natural flow condition the infiltration velocity could be recovered to 84-96% within 1-7 days. The study also demonstrated that flooding events could change the water quality. Gupta et al. (2009) demonstrated in their study that the flood scouring would not influence the colloid removal in the pilot-scale experiment.

At a MAR site, the clogging layer could be removed by remedial techniques including scraping, disking, and tillage (Bouwer, 2002). Greskowiak et al. (2005) studied the hydrogeochemical changes in an operation cycle of a MAR site in the Lake Tegel, Berlin, Germany, where the declogging is done mechanically with a dredging depth of 10cm. At the end step of one operation cycle, the scraping of the clogging layer would drive the infiltration rate from almost zero back to around 2 m/d and fully saturate the unsaturated zone below the pond bottom. However, there was no conclusion on whether the declogging would worsen the treatment efficiency. A study by Grischek et al. (1998) highlighted a possible negative influence from declogging, where the removal of the POC pool might limit the denitrification efficiency. Another study by Escalante et al. (2015) demonstrated the technical record on how

to remove the clogging layer by tractor and excavator. However, there are only relatively few studies on the clogging removal of RBF sites.

1.4.3 Influence from hydrogeological conditions

Traveling distance is a crucial issue on the NOM removal efficiency with a site-specific effect (see section 1.2.2). Hiscock (2005) described the flow path after the colmation layer as having low degradation and sorption but high mixing processes. The traveling time is often adopted in the guidelines as an essential requirement for setting up an RBF site, (e.g., 60-day is assumed as a threshold for the pathogenic bacteria removal in Netherland (Schijven et al., 2003)). Most recorded RBF wells are located at alluvial aquifers (Ray, 2002b). In these RBF wells the traveling time is strongly depended on the local hydraulic conductivity while the different flow path is decided by the geological heterogeneity. Champ et al. (1979) subdivided the redox process in groundwater as a closed or open system. The main difference between an open and a closes system is that the reaeration process in the open system would keep the aquifer in aerobic condition. After investigating an RBF site at Liao River, China, Su et al. (2018) concluded that distribution of the redox zonation and its extent would be dominated not only by the hydraulic conductivities at the riverbed but also the aquifer.

Theoretically, the distribution of the redox zonation along the aquifer is often the result of both temperature and hydrogeological conditions. In the summertime, the warmer temperature of the surface water travels further in conductive aquifers, which strengthens the bioreaction along the flow path and narrow down the oxic zone. However, the shorter residence time might be insufficient for redox reactions. This allows the further traveling of both pollutants and electron acceptors (DO, nitrate) which drives the oxic zone to a larger distance. Therefore the redox zonation in summer is the equilibrium state by the coaction of the abovementioned conditions. In wintertime, the oxic zone enlarges due to the faster traveling time together with the low bioreaction rate according to the cold temperature. For aquifers with low conductivity, the oxic zone is squeezed into a much smaller dimension due to the long travel time, both in summer and winter.

The redox zonation is not only site-specific but also heterogeneous within one RBF site. This local heterogeneity may drive the redox zone distribution to have a distinct pattern along the different flow paths. Kedziorek et al. (2008) demonstrated at an RBF site at the Lot river in France that asubstantial difference of DO and nitrate concentration between two observation wells. The more distant well showed fewer electron acceptors consumption while a closer well showed much lower DO and nitrate concentration.

In bank filtration the groundwater table re-aeration process along the flow path also influences the redox zone distribution. Kohfahl et al. (2008) compared the different aeration

source by modeling simulation demonstrated that the oscillation of the groundwater table controlled by the pumping activity is one of the most important reaeration processes. This oscillation drove the redox zonation to be stratified vertically. An inversed redox zonation distribution was also observed in the study by Su et al. (2018) at an RBF site beside the Liao River inChina. The oxic zone was located at the bottom layer with more reductive zones situated at shallower depths. Another extreme case of a very long oxic zone was observed in the river Danube (van Driezum et al., 2019) where the suboxic zone extended until more than 500m from the riverbank.

1.5 Using temperature as a tracer

Along the propagation path, the amplitude of the temperature signal from the surface water will be damped gradually and the peak will be shifted to later times. Based on this feature, cross-correlation analysis has been used for estimating the travel time between observation wells and river channel (Hoehn and Cirpka, 2006; Sheets et al., 2002; Vogt et al., 2009). Mathematically, heat propagation could be described by a Conduction-Convection Equation (Domenico and Schwartz 1998) which shares a great degree of analogy with the Advection-Dispersion Equation of solute transport (Anderson, 2005; Hecht-Méndez et al., 2010; Kalbus et al., 2006). Compared to hydraulic conductivity, which may vary by orders of magnitude, thermal conductivity is much less sensitive to changing grain size. This promises less predictive uncertainty and higher accuracy in flow calculations compared to hydrometric methods (Rau et al., 2014; Stonestrom and Constantz, 2003). Investigations were undertaken in quantifying the vertical flux in riverbed sediments by applying analytical (e.g., Keery et al., 2007; Luce et al., 2013; Stallman, 1965; Suzuki, 1960) or numerical solutions (e.g., Koch et al., 2016; Munz and Schmidt, 2017) to the 1D advection-conduction equation, and further comparison with either surface-based estimation (Constantz et al., 2002; Ronan et al., 1998) or physical methods (Zamora et al., 2008) of channel losses or with other tracers (Xie et al., 2016). Analytical evaluation of the diurnal temperature variation furthermore allows the identification of horizontal water flux in riverbed sediments (Munz et al., 2016), which is of primary importance for hyporheic exchange and bank filtration.

Combined water head and temperature patterns could be used for estimating aquifer permeability (Stallman 1963). Research by Bravo et al. (2002) and Munz et al. (2017) illustrated that by considering heat transport, the model non-uniqueness could be reasonably constrained and the accuracy of flux estimation could be improved. Numerical models of different dimensions and extent have been adapted and calibrated against both temperature and water head data. In two-dimensional cases, Mutiti and Levy (2010) demonstrated that an increasing trend of riverbed hydraulic conductivity was preceded by extreme hydrologic events. Burow et al. (2005) used a series of best-fit scenarios to quantify the seepage rate and

further estimate the potential dissolved organic carbon (DOC) loads. By adopting a two-dimensional combined flow and heat transport model from a three-dimensional flow model, Nützmann et al. (2014) achieved a refined picture for investigating the groundwater-surface water exchange process at the River Spree. In a three-dimensional case, Masbruch et al. (2014) investigated the groundwater and heat transport in Snake Valley, USA, using a three-dimensional, steady-state model. With respect to transient modelling, Mastrocicco et al. (2011) compared the changes in parameters with a natural gradient test. Colombani et al. (2015) recently coupled heat and a salt tracer together to depict aquifer properties on a small scale in a forced gradient test. At a larger scale, research by Karan et al. (2014) has demonstrated the modelling of water exchange in a heterogeneous flow field and specified the effect during rainfall-runoff events. The temperature distribution is of interest also for the degradation of compounds introduced by recharging groundwater from infiltration ponds and was simulated (e.g., Engelhardt et al., 2014). In investigating managed aquifer recharge, Vandenbohede and Van Houtte (2012) illustrated the change of groundwater residence times in a Belgian dune area based on a flow and mass transport model (Vandenbohede et al., 2008). Seibert et al. (2014) simulated the dynamics of chloride and heat distributions for the injection of treated wastewater into a heterogeneous aquifer. Such changes are also the case for bank filtration, and as Liao et al. (2014) stated, the most thorough way to interpret tracer investigations would be a spatially-explicit modelling of coupled "river-groundwater" and "flow and transport". This was the approach of the recent work, though not for bank filtration, by Reeves and Hatch (2016) in a synthetic study and by Munz et al. (2017) for a reach of a small river based on field data. Few studies so far have used heat as a natural tracer for the numerical modelling of bank filtration (Henzler et al., 2016) and almost none have investigated its details with 3-D modelling of flow and heat transport, especially in areas with geological heterogeneity.

1.6 Motivation and research question

In this dissertation we focus the study area at an RBF site along a human-made canal at Nedlitz, Potsdam, Germany. Similar to surrounding RBF sites, this canal is built on a quaternary aquifer that contains highly heterogeneous glacial till deposits. Therefore, the local groundwater field is also complicated. In order to increase the boat bearing capacity of the canal it was reconstructed by deepening and reconstructing the canal bottom and setting up a new bank protection area. The dredging included a 0.5-meter excavation and extra material replacement reaching a depth of around 2 meters. The original protection material of the bank was also removed and replaced. These construction changes to the canal were likely to influence the flow field, thermal field, and further the redox reaction along the flow paths. As it has been shown in the literature review, no study could be directly taken as reference for

this project. For RBF sites, previous investigations were mainly about clogging and natural declogging processes. For MAR pond and slow sand filtration systems artificial declogging was primarily focused on the removal of the external clogging and did not typically reach the deeper area, let alone the meters of change on the surface water bottom. This dissertation is focused on the influence of the canal bed reconstruction on the water quantity, thermal field, and water quality analysis, superposed by the great hydrogeological heterogeneity in the flow field. The following part of this monography is categorized into four chapters, 1) Study area and method, 2) Results of field observations including water chemistry , 3) Result of groundwater flow and heat modelling, 4) Discussion and conclusion.

The study area and method section state the sampling related issues, the hydrogeological condition of the investigation field, the method used for further data analysis, and the setting up of the geological model for future modelling work. The study area section includes 1) sampling events, which introduces the different sampling items, sampling equipment, sampling frequency, and the sampling result; and 2) the local hydrological and geological condition, which is the basis for future modelling work. The research method focuses on the formula of heat transport, the step of stable isotope data analysis, the formulas for calculating the SUVA and the ETC. The last section concerns the process for setting up the FEFLOW model

The water chemistry study covers the analysis of the cations, anions, DOC, temperature profiles, and stable isotope. Temperature profiles are used to illustrate the distinct flow path in the near-bank wells caused by the local heterogeneity. Both the stable isotope result and the main cations and anions analysis are used to distinguish the source of the groundwater. The concentration of electron acceptors, together with DO are used to evaluate the redox zonation distribution affected by the local heterogeneity and the canal bed reconstruction. The change caused by the reconstruction on different electron acceptors and DOC is assessed by the statistic test.

The fluid model is carried out using FEFLOW which was based on the geological model. It is subdivided into a groundwater flow model and a heat transport model. The groundwater flow model includes a steady state and a transient state model. The steady state model would be focused on a global picture of the flow field and acts as the basis for the transient model calibration. The transient state model highlights the observation points between the canal and the production wells, calibrating the model by changing the hydraulic conductivities of the geological components. The canal reconstruction is included in the transient model in a lumped way. Since neither the elevation change nor deleting the element is feasible during the simulation, the influence of the reconstruction is represented by the change of conductance in

the canal bed. It is further compared with an assumed scenario without reconstruction. The change of the infiltration rate and traveling time is also quantified. The heat transport model is based on the transient model and evaluates the thermal field due to the seasonal surface water change and air temperature change. Similar to the transient fluid model, two scenarios of with and without hydraulic conductivity change are compared to show the influence of the riverbed reconstruction.

The last section is a summary of the abovementioned chapters and further concludes the water quantity and quality change brought by the canal bed reconstruction. Discussion is categorized into five separate sections: 1) the flow field, 2) redox zonation, 3) treatment efficiency, 4) the rehabilitation and reclogging process and 5) heat transport model. Comparisons with other investigations are also made in the last section. The shortcomings of the research with respect to modelling accuracy, the sampling frequency, and sampling items are summarized, and recommendations are given to future studies.

Chapter 2 Study area and method

In this chapter, the section 2.1 (except the Water chemistry data and stable isotope data sampling), part of section 2.2.2, and the section 2.3 are mainly adopted from the published article 'Impact of river reconstruction on groundwater flow during bank filtration assessed by transient three-dimensional modelling of flow and heat transport' by Wang et al. (2020), which can be accessed online as https://doi.org/10.1007/s10040-019-02063-3.

2.1 Study Area

The study site is located in Potsdam (Brandenburg, Germany), where a riverbank filtration-based waterworks is operated south of a human-made canal. The canal acts as the shortcut between Lake "Weisser See" and Lake "Jungfernsee" (Fig. 2.1b), which is part of the Lower Havel shipping route (Untere Havel-Wasserstraße) connecting Berlin with the lower River Havel, sidestepping the city of Potsdam. Nearby, there are three other lakes, as is shown in Fig. 2.1c. Aiming at higher capability for boat-bearing, a reconstruction work, including renovation of the canal bottom and the canal bank, has been accomplished. Overall, it took place from 17th June 2013 until 19th May 2014. Based on the engineering schedule, the canal bottom was sectioned into four operational segments for performing the reconstruction works, and the particular period of reconstruction works is shown in Fig. 2.1b and the more detailed schedule is listed in Table S2.

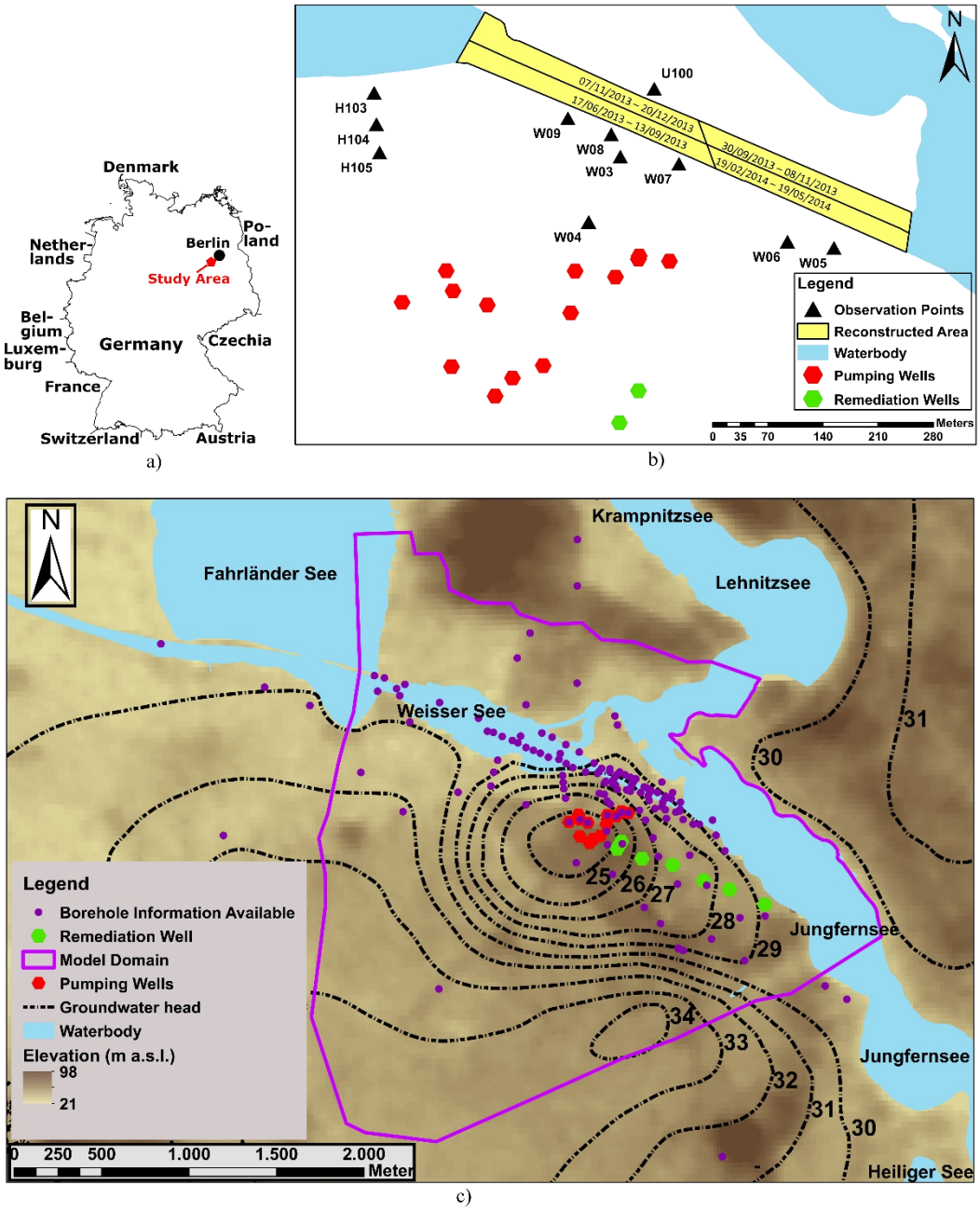

Figure 2.1. a) Location of Potsdam in Germany. b) Location of observation wells and pumping wells beside the canal "Nedlitzer Durchstich" (yellow area, divided based on the effective schedule of reconstruction). c) Study area with groundwater equipotential lines (m.a.s.l.) of the uppermost aquifer, location of pumping and remediation wells, and the location of all borehole profiles used to design the geological model structure. Background map of DEM was adopted from NASA's Land Processes Distributed Active Archive Center (LP DAAC) (2019) accessed on 24 September 2019.

A detailed sketch of the canal cross-section before and after reconstruction is shown in Figure 2.2. The reconstruction work directly deepened the canal by 0.5 m, and further modified replaced the canal bed by adding more permeable material up to a depth of 2 meters. The canal bank renovation started earlier than the bed reconstruction and continued along with the

entire time frame. It kept the slope of the bank towards the canal bottom and replaced the original protection material on the bank with new ones. As it has been shown in the previous discussion, the external clogging layer was mainly within a depth of decimeters, while the internal clogging is also within meters. The abovementioned renovation work has wholly removed the external clogging area and replaced the internal clogging area with much more conductive material during a short time frame. Together, it would drastically change the hydraulic condition and the infiltration pattern.

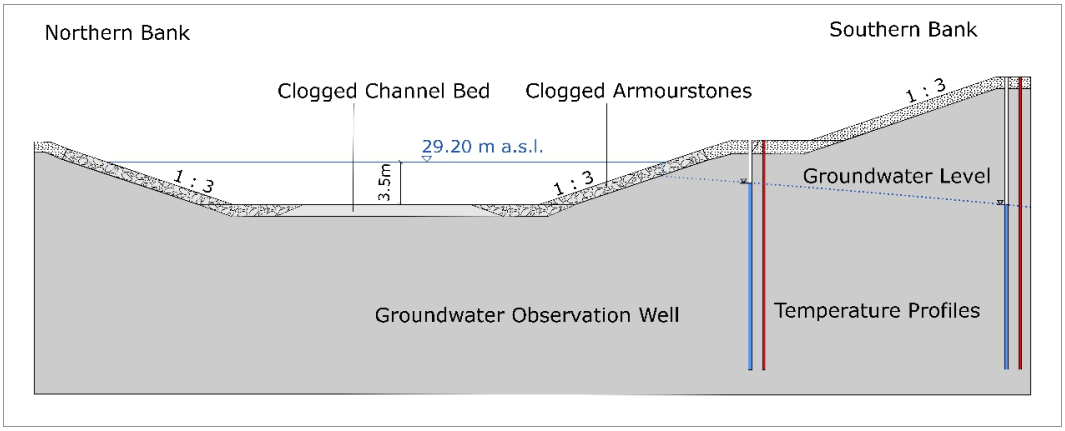

(a)

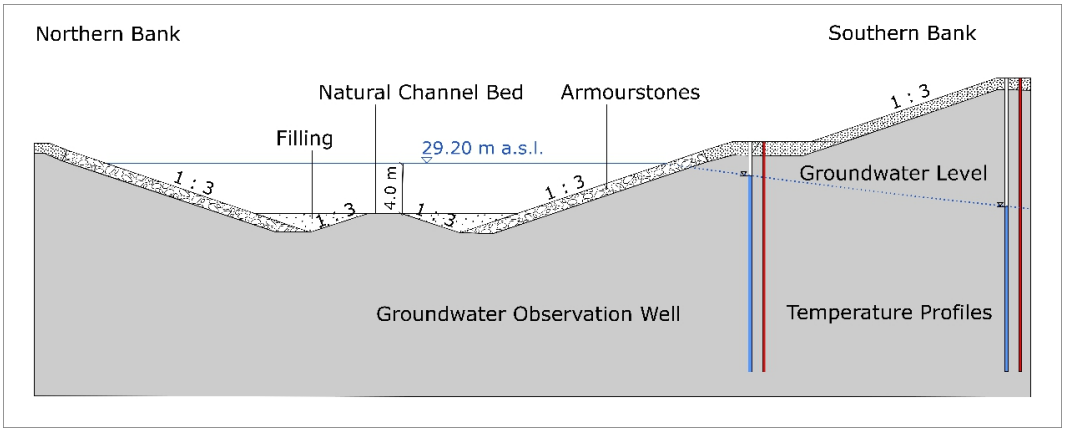

(b)

Figure 2.2 a) The canal cross-section profile before reconstruction and b) after reconstruction (adapted from Doettling, 2014)

2.1.1 Sampling Events

Hydrological data and Temperature data sampling

The water level in the canal was adopted from two sampling stations separately in the up and downstream of the canal. Due to the data availability, the data of the upstream station was adopted before the date of 3rd Dec 2013, where the measurement of the downstream station continued until the end of December 2014. The two measurement time series was with a

difference of only centimeters, and no bias correction was made. The temperature of the canal for the research period was retrieved from two stations as well. Temperature data before October 2012 were derived from a gauging station around 6 km upstream, in a parallel branch of the river Havel flowing through the city of Potsdam. After that time point, the temperature was adopted from the same downstream logger as the water head measurement. The two temperature time series showed good data consistency and thus were used in combination to define the canal temperature for the entire simulation period. Daily precipitation and air temperature (2 m above ground) were measured at the nearby Leibniz Institute for Agricultural Engineering and Bioeconomy (ATB) about 2 km west of the study site.

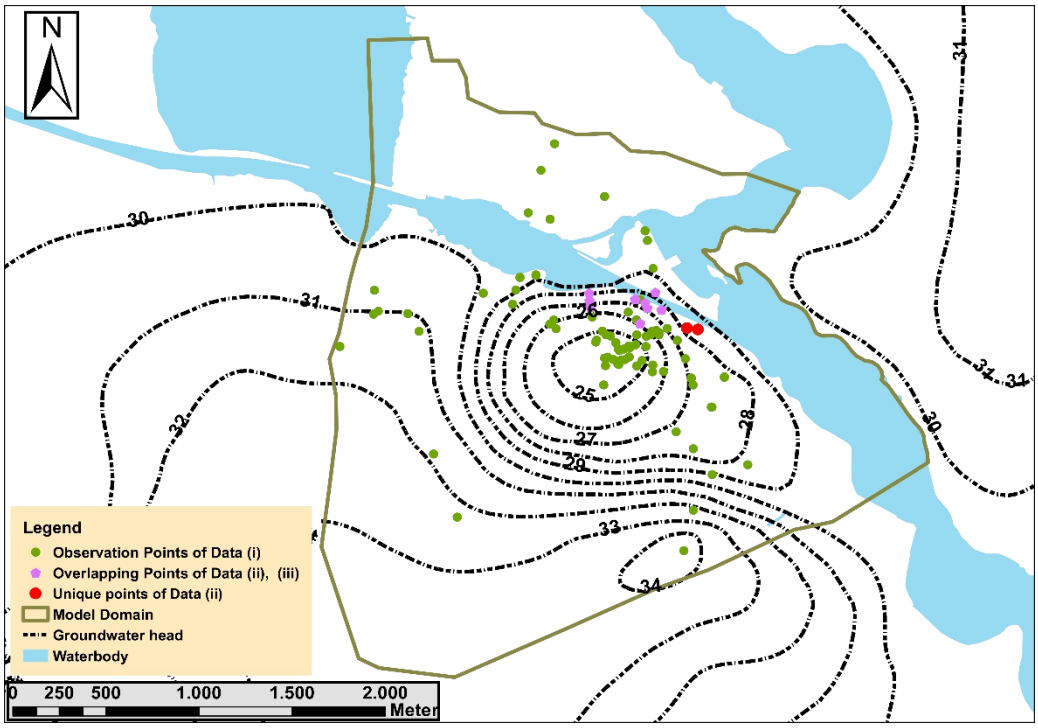

Figure 2.3 Observation points of different data groups.

For the groundwater sampling of the temperature and water head data, there are in total of 104 groundwater observation wells included within the study area. They could be further grouped into three categories according to their sampling frequency and sampling procedure, while the distribution of them is shown in Fig. 2.3 and Fig. 2.1b:

(i) Water heads were measured in 89 observation wells distributed within the study site (green points in Fig. 2.2) in mid-April 2012. The filter screens are mostly 2 m long, while the bottom elevation varies from 19 to 34 m. These water heads were used in the latter study as the calibration targets for a numerical steady-state flow model.

(ii) Water heads and temperatures were measured continuously at 15 observation wells using automatic data loggers with time intervals varying between 5 minutes to 6 hours (Rugged

TROLL 100, In-Situ®, United States) with an accuracy of ± 0.01 m for water head and ± 0.3 K for temperature. Measurements took place from June 2009 to December 2014. Most of these observation wells (except U100) are located between the canal and the pumping well group, and some of them are situated along the canal banks (Fig. 2.1b). Some of the observation wells (W03, W04, W07, and W09) comprise two adjacent wells with different filter screen elevation, which is denoted by HIGH (upper well screen) and LOW (lower well screen) (Table 2.1). For the observation wells W03, W07 and W09, the data loggers in HIGH and LOW were set at the same elevation. These water heads were used as calibration targets for a transient flow model.

(iii) Representative groundwater temperatures were measured in 12 observation wells weekly or biweekly, over 18 months from June 2013 to December 2014. Except for two additional measurements in W05 and W06, the sampling points are identical to the group (ii). These temperatures were used as calibration targets for the heat transport model.

Table 2.1. Configuration of the observation wells located between the canal and the pumping well group (except U100 which is located at the northern bank), sorted with increasing distance to the canal; and the number of hydrochemical and DOC samples analyzed, subdivided into the ones before reconstruction started and the one after the start of the reconstruction.

Well Name	Well Name (abbreviation)	Elevation (m a.s.l.)		Distance to the canal (m)	Hydrogeochemical analysis sample number		DOC sample number	
		Data logger	Screen Bottom		Before Reconstr	After Reconstr	Before Reconstr	After Reconstr
U100	U100	20.4	-1.21	16	12	10	12	18
$W03_{HIGH}$	W03H	20.5	18.8	33.9	20	15	20	23
$W03_{LOW}$	W03L	20.6	-0.2	35	20	18	20	20
$W04_{HIGH}$	W04H	20.5	20.1	126.2	19	17	19	25
$W04_{LOW}$	W04L	16.5	0	127.3	19	16	19	24
$W07_{HIGH}$	W07H	25.1	23.3	13.2	8	18	8	26
$W07_{LOW}$	W07L	25.1	17.8	13.5	8	18	8	26
W08	W08	22	17.8	13.5	8	18	8	26
$W09_{HIGH}$	W09H	26.5	22.7	16.3	8	13	8	21
$W09_{LOW}$	W09L	26.4	16.6	16.7	8	17	8	25
Canal	--	--	--	0	40	18	45	32

Water chemistry data and stable isotope data sampling

The water samples were collected by field sampling campaigns with different sampling activities. In situ measurement started at different times for different points. Measurement for W03 and W04 began from July 2007, U100 from August 2009, and W07, W08, W09 from September of 2010. The time step started with three months, became weekly from March 2013, and switched to biweekly and monthly until February of 2017. Stable Isotope sampling

overlapped with *in situ* measurement starting from March 2013 to September 2014. The sampling frequency for analysis of the dissolved organic carbon, the dissolved cations and anions were less than *in situ* measured data. Also, there was a long sampling gap between October 2014 and September 2015 (Table S1). The total number of SW sampling for DOC was more than the cation and anions (Table 2.1). In situ temperature measurement with multi-depth was with a frequency of one month, started from May 2015 to April 2016.

Temperature, DO, and pH values were measured *in situ* by the multi-parameter portable meter (WTW ProfiLine Multi 3320, Germany). For temperature measurements in different depths, temperature sensors were applied and put in the observation wells carefully, avoiding the possible mixing effect. The temperature data was read once per meter until it reached the well bottom. The concentrations of the cations and anions (Cl^-, SO_4^{2-}, NO_3^-, NO_2^-, HCO_3^-, Na^+, Ca^{2+}, NH_4^+, Fe^{2+}, K^+, Mn^{2+}, Mg^{2+}) were measured by Ion Chromatograph DX-120 (Dionex Corporation); the DOC was measured by TOC-5050A, (Shimadzu) (filtered through 0.45 µm). Analyses were performed by the Labor für Wasser und Umwelt GmbH, Bad Liebenwerda until September 2014, and then by the Geochemisches Gemeinschaftslabor, Technische Universität Berlin until July 2017. The ionic balance error for observation wells varied from 0.7% to 1.5% in Labor für Wasser und Umwelt GmbH, which was fulfilling the criteria of 5% (Hiscock, 2005). The concentration of HCO_3^- is not available in the lab of Geochemisches Gemeinschaftslabor, and therefore, it was calculated by the imbalance of equivalents between the cations and anions. Measurement results of nitrate were frequently noted to be smaller than the limit of detection (1 mg/L before September 2014, 0.375 mg/L after the September 2014). For the measurements of those cases, half of the limit value was adopted.

2.1.2 Hydrological Condition

Precipitation and groundwater recharge

During the research period, the average annual precipitation varied between a minimum value of about 382 mm in 2011 and a maximum amount of 663 mm in 2010. For 2013 and 2014 the annual precipitation was about 468 mm and 436 mm, respectively. On average, 122 rainy days per year occurred between May 2009 and May 2015. The highest rainfall magnitudes and intensities were observed mainly in July/August each year. The maximum rainfall intensity was 42.8 mm/d. Also, for high rainfall intensities, no surface runoff was noticed at the study site, and thus also high intense precipitation was assumed to recharge into the aquifer without substantial losses at the surface.

The level of groundwater recharge was estimated based on a large-scale conceptual model (https://maps.brandenburg.de/WebOffice/synserver?project=Hydrologie_www_CORE&client=core). In the study area, the evaluated ratio of (Precipitation - Actual evapotranspiration) /

Precipitation between 1991-2010 varied from 18.7% ~ 19.7%, and a rounded-up value of 20% was taken as a fixed recharge ratio in the following modeling work. Correspondingly, the estimated yearly groundwater recharge ranged between 76.1 mm/year in 2011, as the driest year, and 138.2 mm/year in 2010, as the wettest year.

The pumping rates at the waterworks slightly varied between 6000 m^3/d and 7000 m^3/d, including a series of protection wells. Since July 2014, an extra remediation pumping (~2090 m^3/d) located east of the pumping wells of the waterworks (Fig. 1c) was started but was not related to the canal reconstruction measures. Overall, groundwater recharge in the catchment area of the waterworks plays only a minor role due to the substantial contribution of river bank filtration to the water balance.

2.1.3 Geological Condition

The research area is placed on highly heterogeneous glacial tills, which is similar to studies in the nearby area, (e.g., Waterworks Tegel (Berlin, Germany) (Henzler et al., 2014; Henzler et al., 2016; Wiese and Nützmann, 2009)). The geographical features of the area are described broadly based on a geological report on the Lower Havel waterways (Hydrogeologie GmbH, 1993). Surface elevation is, on average, 30 m a.s.l. (meters above sea level) in the lowlands of the River Havel, while some hilly areas lie within the range of 40-50 m a.s.l., only a few hills reach a height of 80 m. The RBF site takes place mainly through Quaternary aquifers, which are semi-confined aquifers stratified by glacial till layers from the later Pleistocene. Featured as relatively impermeable material, the glacial tills - from the bottom to the top - were formed in the Saale I glacial period, Saale II glacial period and Weichsel I glacial period, but the structure and extent are substantially different between them. The glacial tills of Saale-I (SI-GT) and Saale-II (SII-GT) cover most of the study area and join at some places that form thicker glacial blocks. The youngest glacial till formed in the Weichsel I glaciation (WI-GT) is the utmost glacial till of the study area and is not as continuous as the two former glacial deposits. This is likely due to periglacial processes and erosion during the Holocene. Especially in the area below the NDthe glacial till exists as a single lens and covers half of the area of the canal bottom. Sand exists above the WI-GT, while mud, silt and lake chalk show up at the lakes' bottom. Stratified by semi-permeable glacial tills, the shallow aquifers could be divided into four layers by their relative locations, which is a sandy aquifer (i) above WI-GT; (ii) between WI-GT and SII-GT (iii) between SII-GT and SI-GT and (iv) below SI-GT. At the bottom of the deepest of these Quaternary aquifers, a Miocene layer consisting of silt, fine sand, lignite, and clay exists, which separates these shallow aquifers from the deeper aquifers. Water exchange might occur at some locations due to the existence of hydrogeological windows possibly formed by erosion during the Pleistocene.

One hundred forty-five drilling wells together with nine geological cross-sections were available as the basis for constructing the geological model (Fig.2.1c), while the drilling information was not evenly distributed over the area. Most of the known boreholes were located between the channel bank and pumping wells. Little information was available for the southern and western parts of the study area. This asymmetrical distribution of geological data led to uncertainty for the shape delineation of geological structures in the southwestern hinterland but coincided with the objective of the study of focusing on the area between the waterworks and surface waters. Sixty-seven drillings nearby the canal reached shallow depths only (from 2.4 m to 23.23 m a.s.l.). Another 78 boreholes reached deeper layers. Few of the drillings reached down to the Miocene layer. This implied that the uncertainty in the geological structure increased with depth. Another uncertainty for the geological categorization was heterogeneity and discontinuities because the unconsolidated structure of the Quaternary layers might have well been modified by erosion after its formation. The final result of the geological model is shown in Fig. 2.4 below, where all the glacial tills, sapropel and silt were represented by the colored units.

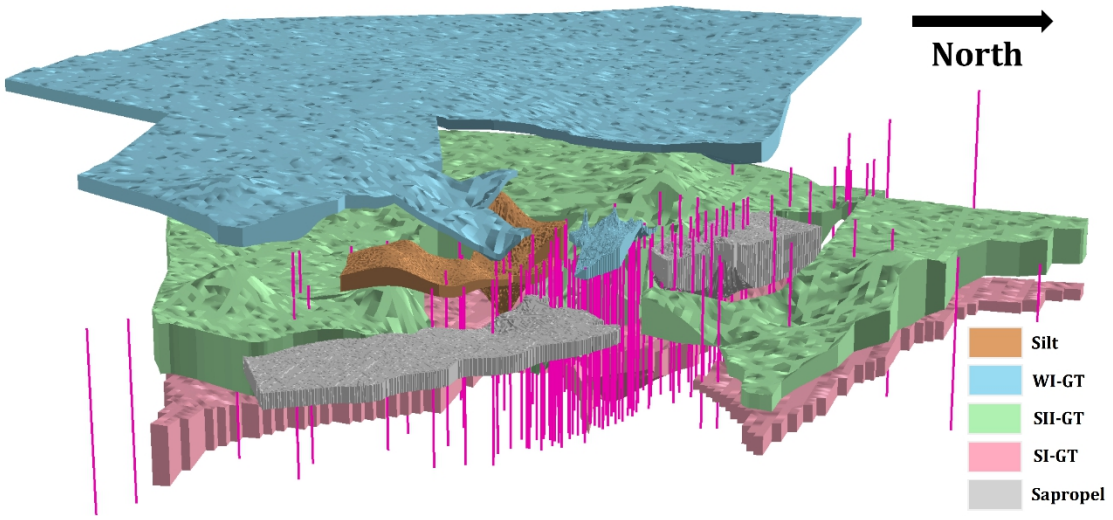

Figure 2.4. Geological model as represented in FEFLOW, showing the units confining the sand aquifers in between them; view from the northeast towards the waterworks in the center.

2.2 Research Methods

The study on the influence of the canal bed reconstruction and the local heterogeneity on the RBF site could mainly be subdivided into a water chemistry study and a modeling study. For the water chemistry analysis, the investigation was focused on both general flow field characterization and redox zonation. At first, both stable isotopes and cation/anion were used to characterize the different flow paths and their change caused by the canal bed reconstruction. Based on the sampling result, the main ions were expressed in the form of the

trilinear diagram (Piper, 1944), which is commonly adopted in hydrochemistry study (Fetter, 2018). The charting was done with *GW_Chart*, developed by USGS (Winston, 2000). Redox condition in the aquifer was characterized by means of presence or absence of redox-sensitive species (dissolved oxygen, nitrate, dissolved manganese or iron and sulfate) as proposed by different studies (Champ et al., 1979; Massmann et al., 2008b). The comparison of change of electron acceptors were classified into two groups that are before and after the reconstruction. With the potential seasonal dynamic of DO and NO_3^-, the temporal behavior is of interest as a complete time series. For the electron acceptors Fe^{2+}, Mn^{2+}, SO_4^{2-} and NH_4^+, few studies so far have shown the seasonal dynamic, and the sampling frequency in our study also allows for monitoring seasonal dynamics however it is still too limited in describing the sub-monthly dynamic of the ions. Violin plots were adopted to analyze the variation of these anions and cations only separated into the category before (before 17th June 2013) and after (after 17th June 2013) the start of reconstruction. In subsequent, but separate studies, the transport and fate of organic micropollutants at this RBF site have also been investigated (Munz et al., 2019; Barkow et al., 2020).

In this method section, the usage of water stable isotope data, the calculation of the electron trapping capacity (ETC), and the specific ultraviolet absorbance (SUVA) will be introduced. The modelling study will be presented stepwise, by order of steady state fluid model, transient state fluid model, and heat transport model. Since the model was built on FEFLOW, version 6.1 (Diersch and Kolditz, 2002), and as this is a widely adopted modelling tool, the theory of fluid transport will be omitted, and only the heat transport theory will be introduced in section 2.2.2.

2.2.1 Stable isotope and water chemistry data

Stable isotope

Being part of the water molecule, both hydrogen and oxygen isotope ratios could act as tracers for water sources investigation during surface water–well interaction (Hunt et al., 2005). Krauskopf and Bird (1995) summarized three main mechanisms on isotope separation, including (1) physical properties, (2) exchange reactions, and (3) reaction rate. While Freeze and Cherry (1979) mentioned that in shallow groundwater systems, with normal temperature, both ^{18}O and ^{2}H concentration could be taken as the characteristic property of subsurface flow after the water flow below the soil zone. The measured concentration of both ^{18}O and ^{2}H are expressed by the notation of δ values (in parts per thousand or ‰), with the formula below:

$$\delta = \frac{R_{sample} - R_{standard}}{R_{standard}} \cdot 1000 \qquad (1)$$

In which the $R_{standard}$ denotes the V_{SMOW} (Vienna Standard Mean Ocean Water), for which $\delta^{18}O$ and $\delta^{2}H$ equals to 0 (Hiscock, 2005). Featured as a different source, the pristine groundwater from further north and the newly infiltrated water from the canal might act as two end members to show the difference in the plotting. With different mixing ratios, the concentration observed in the wells can vary in between. A second-order parameter of deuterium excess *d* was adapted to show the difference in plotting, with the formula:

$$d = \delta^{2}H - 8 \cdot \delta^{18}O \quad (2)$$

Electron trapping capacity (ETC)

For the quantification of oxidation capacity, previous studies (Barcelona and Holm, 1991; Heron et al., 1994) have suggested a method which simply summed up all the electron acceptors weighted by the involved electron number. By only keeping the oxygen and nitrate in the formula, Kedziorek and Bourg (2009) proposed a follow-up concept - Electron trapping capacity (ETC). ETC could be used as an indicator to identify conditions favoring the reductive dissolution of manganese and iron. The redox potential is not adequate to quantify a range on the releasing of manganese and iron in the aquifer. Therefore the ETC represents the quantity of electrons that O_2 and NO_3^- are capable of trapping as groundwater moves from oxidizing conditions to the Mn and Fe reducing environment. The higher the ETC, the less reductive the conditions and the lower the probability of dissolution of manganese or iron oxyhydroxides (Kedziorek and Bourg, 2009). Based on the review of previous studies, Kedziorek and Bourg (2009) proposed the calculation formula of ETC as:

$$\mathrm{ETC} = 4[\mathrm{O_2}] + 5[\mathrm{NO_3^-}] \quad (3)$$

The $[\mathrm{O_2}]$ and $[\mathrm{NO_3^-}]$ stand for the molar concentration of dissolved oxygen and nitrate, and therefore, the ETC is expressed by the unit of molar concentration. The threshold ETC values for manganese and iron dissolution are summarized based on both lab and field data and are 0.2 mM (manganese dissolution) and 0.1 mM (iron dissolution), respectively.

Specific ultraviolet absorbance

Specific ultraviolet absorbance (SUVA) is simply defined as the ratio between the UV absorbance at 254 nm and the DOC concentration (Leenheer and Croué, 2003), as it is shown in the formula below. It is a simple approach to differentiate the composition within the DOC since humic substances and aromatic compounds usually shows higher absorption at the wavelength of 254nm (Weishaar et al., 2003). Therefore, higher SUVA value stands for a higher weight of the aromatic compound composition in the DOC.

$$\mathrm{SUVA} = \frac{\mathrm{UV}_{254}}{\mathrm{DOC}} \tag{4}$$

Where the UV_{254} stands for the UV absorbance at 254 nm by the unit of m^{-1}, and the DOC stands for the dissolved organic matter concentration by the unit of $mg \cdot L^{-1}$.

2.2.2 Heat transport model in FEFLOW

Mass and heat transport share more features in common and analogous partial differential equations could be applied to both in subsurface flow (Hecht-Méndez et al., 2010). In FEFLOW (Diersch and Kolditz, 2002), it is described as

$$\frac{\partial}{\partial t}\left[\left(\varepsilon\rho^f c^f + (1-\varepsilon)\rho^s c^s\right)T\right] = Q_T - \frac{\partial}{\partial x_i}\left(\rho^f q_i^f c^f T\right) + \frac{\partial}{\partial x_i}\left(\lambda_{ij}\frac{\partial T}{\partial x_j}\right) \tag{5}$$

Where t is the time; ε is the effective porosity; ρ^f and ρ^s are the densities of the liquid and solid phases, respectively; c^f and c^s are the heat capacities of the liquid and solid phases, respectively; T is the temperature; x_i and x_j stand for the distance from the origin of the coordinates at i, j stands for direction; q_i^f stands for the Darcy velocity component of the i direction; λ_{ij} stands for the total effective thermo-dispersion tensor, and Q_T stands for the source-sink term.

Formula 5 states that the change of heat stored in a control volume (the first term on the left-hand side) results from the joint action of the source-sink term, the convection of heat in the fluid phase and the total effective thermo-dispersion of both phases (as the terms on the right-hand side). The effective thermo-dispersion term is approached in the form of Fourierian heat flux in both solid and liquid phases governed by Fourier's law. As a sum parameter, λ_{ij} includes three components, and the relationship can be shown as (Diersch and Kolditz, 2002)

$$\lambda_{ij} = \lambda_{ij}^{cond_f} + \lambda_{ij}^{cond_s} + \lambda_{ij}^{disp_f} \tag{6}$$

where $\lambda_{ij}^{cond_f}$, $\lambda_{ij}^{cond_s}$ are the conductive portion of the thermo-dispersion tensors in the fluid and solid phases, and $\lambda_{ij}^{disp_f}$ is the dispersive part of the thermo-dispersion tensor in the fluid phase.

In FEFLOW, the source-sink term, volumetric heat capacity, and heat conductivity are defined separately for different phases, while the effective porosity and longitudinal and transversal dispersivities are set for the bulk porous medium. Effective porosity mainly controls the volumetric ratio between the solid and liquid phases, which is a difference in solute transport. Taking water as the liquid phase, its physical parameters relevant to heat transport are known, while parameters of the solid phase could vary and have been subjected to calibration within the bounds of a reasonable parameter range.

2.3 FEFLOW Model Set-up

The modelling domain is based on the groundwater head contour map, which was interpolated based on water heads measurements of mid-April, 2011, according to the environmental agency (MLUL Brandenburg), as it is shown in Fig. 2.1c. Another interpolation of the measurements from mid October 2011 generally featured the same shape, while the water head was globally 1 meter higher. The constant pumping activity in the waterworks formed a large cone of depression. This pumping drove the groundwater table decreasingly towards the depression. The water flowed through the quarternary aquifers and converged at the pumping wells both from the canal and the area south and west. Approximately 1 km south of the cone of the depression, the water head reached a maximum of 34 m. a.s.l, and further formed a groundwater divide extending towards the south bank of the lake “Jungfernsee”. In the west, the pumping activity did not have much influence as a water divide that started from the southeast end of the lake “Fahrländer See” and ended by converging with the groundwater divide went through the high water head area (Fig. 2.1c). Generally, the water head information was missing in the north, except for the area east of the Lehnitzsee. About 500 m north of “Weisser See”, an area with higher elevation ran east-west between the two lakes and forms a surface water divide. Taking this as a groundwater divide as well, a separate northern groundwater sub-catchment could be delineated that not only delivered water to the surrounding surface water but also contributed to the pumping wells’ catchment if the aquifer provided a hydraulic connection below the ND. In the northeast, the more extensive water body of the lake “Jungfernsee” was included in the model domain as fixed water heads. Together this outlined bounds of the modeling area which included the whole catchment area of the pumping wells, the central area of interest between the pumping wells, and the surface waters. Together, the entire domain covered a total area of around 6.9 km^2, with a maximum extension of 3484 m and 3256 m in the north-south and east-west directions, respectively.

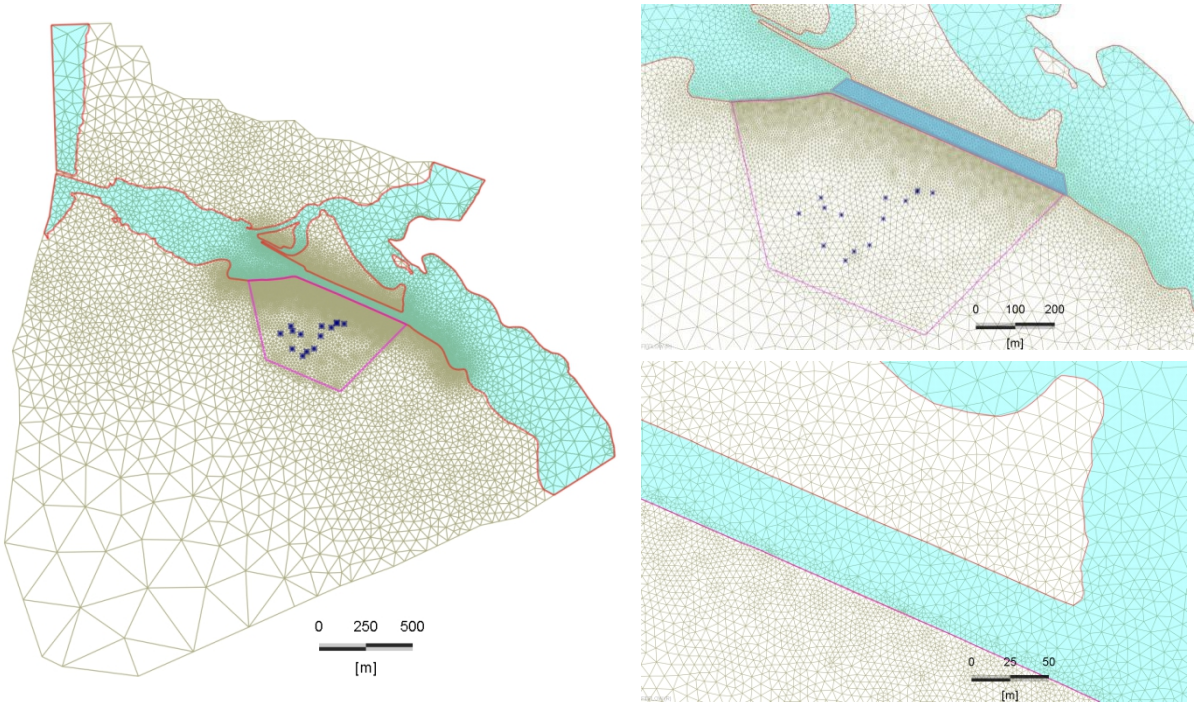

Figure 2.5. Mesh of the finite element model, top view with zoom-in into the area of the waterworks (top right) and the Eastern part of the canal (bottom right). The area of the waterworks and the area of the surface-water groundwater interface are refined, whereas the southwestern hinterland is coarsened. In the top right graph, the area of the canal reconstruction considered in our study is indicated in dark blue.

This model domain was imported in FEFLOW as a polygon. 30384 elements were generated in the top layer accounting for the location of drilling boreholes, pumped wells, observation points of the group (iii), and the banks of the canal and the shores of nearby lakes. Local grid refinement was applied around the area of the ND and pumping well group with the final element size between 5 m and 10 m. This aimed to better depict the relatively strong hydraulic gradient caused by pumping. For the areas of less concern, the element size was increased with distance from the area of interest, which varied from 10 to 300 m (Fig. 2.5). After the initial generation, the meshes were smoothed to meet the Delaunay criterion. The model was then vertically extended to represent the 3-D geological model, and in total, including nine layers of main hydrogeological units (Table 2.2) supplemented by 12 intermediate cushion layers for improving numerical accuracy. The unsaturated zone on the top was set as ‘phreatic mode’ in FEFLOW, implying that its hydraulic conductivity was taken as the saturated K_f-value times the ratio between the saturated thickness and full element height.

Table 2.2 Attributes of 3-D model layers

Geological Layer No.	Slice Attributes	Geological Composition
1st	Sand layer	sand, sapropel
2nd	Main bulk of WI-GT	WI-GT, sand, sapropel
3rd	Sand layer	sand, sapropel
4th	WI-GT lens, silt lens	WI-GT lens, silt lens, sand, sapropel
5th	Sand layer	sand, sapropel
6th	Main bulk of SII-GT	SII-GT, sand, sapropel
7th	Sand layer	sand, merging part of SI-GT and SII-GT
8th	Main bulk of SI-GT	SI-GT, sand
9th	Sand Layer	sand

2.3.1 Groundwater Flow Model

A steady-state model was run and calibrated to provide a consistent representation of the geological structure and their corresponding hydraulic parameters. The auto-calibration of the model was based on the observed water heads at 104 locations distributed within the study site (data groups (i) and (ii)). A Dirichlet boundary of 29.5 m was chosen for the surface water bodies. The pumping wells were set as multi-layer wells with a total pumping rate of 6556 m³/d. The distribution of the total pumping rate to each layer in contact with the well screen was calculated based on the particular K_f-values and the hydraulic head distribution in this layer. In the steady state model, water level and pumping rate represented the meanvalues measured between mid-March and mid-April 2012, a period chosen because of the high density of measured data. Groundwater recharge was set as 0.3 mm/d, which represents 20 % of the mean precipitation of 2011 and 2012. Average daily groundwater recharge volume at the land surface of the model area was about 1780 m³/d and thus only about 21 % of the average volume was pumped daily (sum of production wells of the waterworks and nearby groundwater remediation wells). This reflected a high fraction of bank filtration at this site. All outer boundaries not representing surface waters and the bottom of the model were set as no-flow boundaries according to the configuration of the model domain. Saturated hydraulic conductivities of the steady state model were calibrated using FePEST, integrating the FEFLOW model into the PEST (Doherty 2015) framework. Parameter zones of homogeneous hydraulic conductivity were defined based on the existing geological units. The parameter ranges used in the calibration are given in Table 2.3. The objective function was based on the observed water heads and the anisotropy ratio of hydraulic conductivities, ensuring vertical conductivities (K_v) being linked to the horizontal ones (K_h, where $K_y = K_x$). A maximum limit was set so that K_h/K_v must remain larger than 2 in all geological units, according to Todd and

Mays (2005). Concerning data quality and spatial relevance, different weighting factors were assigned to the hydraulic heads contributing to the objective function. The 12 observation points of the group (ii), which were directly located between the canal and the pumping wells, were given a weighting factor of 10, while for the remaining observation points of the group (i), it was set as 1.

Table 2.3 Model parameters and ranges of the hydraulic conductivities used for the calibration of the steady state model (Domenico and Schwartz, 1998; Hölting and Coldewey, 2013).

Attribute	**Specific Yield (%)**	**Specific Storage (m^{-1})**	**Hydraulic Conductivity （m/s）**		
			Minimum (m/s)	Maximum (m/s)	Initial value (m/s)
Sand	23	1.0E-04	1.0E-05	1.0E-03	1.16E-04
Silt	8	1.0E-04	1.0E-09	1.0E-05	1.16E-06
Sludge	23	1.0E-04	1.0E-09	1.0E-03	1.16E-05
Glacial tills	6	1.0E-04	1.0E-12	2.0E-06	1.16E-06

A steady-state model is only an approximation that can neither reflect the influence of the variation in water heads on the surface water nor adapt to the changes induced by the river reconstruction. Taking the steady-state model results as a starting point, a transient flow model was created to simulate the temporal variation in the groundwater flow system caused by the transient condition in surface water heads, pumping rates and groundwater recharge, and the changing riverbed hydraulic conductivity induced by the river reconstruction (decolmation). To achieve a better vertical resolution, the relatively thick aquifer layer was subdivided into six extra slices in the model. The hydraulic heads of the steady state model were used as the initial condition for the transient simulation. The model boundaries were consistent in type with the steady-state model, but now applying daily average values obtained from the measured time series. The specific yield was set as 6 % for glacial tills, 8 % for silt and 23 % for sand (Domenico and Schwartz, 1998), and specific storage was taken as 1×10^{-4} m^{-1} (Freeze and Cherry, 1979). Limited by the computation time, an automated calibration of the hydraulic conductivities was not feasible. Therefore a manual calibration by trial and error was performed. The transient simulation model was set to start from mid-June 2010 and covered a period of four and a half years until the end of December 2014. For observing water levels in the surface waters, two gauging stations were available near the ND with good data consistency, and these observation points were complementing each other throughout the whole simulation period. Groundwater recharge was taken as 20% of the daily precipitation and applied at the top slice of the model domain, as a rough average though this does not account for the time needed for passing the unsatured zone.

The reconstructed area was subdivided into four parts, where the division between east and west follows a bridge crossing the canal, and the division between north and south corresponds to the middle line of the canal (Fig. 2.1b). As is depicted in Fig. 2.2, the excavation directly deepened the canal by 0.5 m and replenished the deeper area with new material. In the model, all grid elements located in the channel area with a top elevation higher than 24.5 m were assumed to be influenced by the excavation. Since it was impossible in FEFLOW to remove whole elements during a transient simulation, the change in hydraulic resistance was instead implemented indirectly, i.e., all elements affected by the excavation kept their shape but achieved an increased hydraulic conductivity. In the model, the canal area was subdivided into four separate parts (Fig. 2.1b) and the hydraulic conductivity increased successively consistent with the schedule of the reconstruction (Tab.S2). The hydraulic conductivity increased linearly from the original level in to the final. The value was fitted manually to reproduce the increasing water head after the start of the canal reconstruction and the finally adopted values were $K_{xy} = 1.16 \times 10^{-4}$ m/s and $K_z = 2.31 \times 10^{-5}$ m/s.

2.3.2 Heat Transport model

The transient heat transport simulation was carried out from mid-June 2010 to the end of December 2014, corresponding to the transient flow model. The heat transport model adds the energy balance equation to the flow model using its Darcy fluxes as input. Other parameters describing the heat transport were effective porosity, thermal conductivities, heat capacities and dispersivity in the longitudinal and transversal directions. Dirichlet boundary conditions were assigned to the surface water bodies according to measured river temperatures and land surfaces according to measured air temperatures. The remaining boundary conditions were defined as no-flux boundaries. All temperatures were applied as the time series of daily-averaged values. The initial temperature in the model was set to 11.5 °C, which was the temporal average of all observed temperatures.

With respect to heat transport, in FEFLOW, the volumetric heat capacity (c) and heat conductivity (λ) are defined separately for the solid and liquid phase, while the total porosity (ε), the longitudinal and transversal thermal dispersivities (λ^{disp}) are set for the bulk porous medium. Total porosity mainly controls the volumetric ratio between the solid and liquid phases, as both phases contribute to heat transport, which is a difference to non-sorbing solute transport. The total porosity of the glacial tills and sapropel sludge were inferred from saturated gravimetric moisture content and grain density of sediment samples taken in the river section at the south end of the Fahrländer See. The average value of the total porosity was 0.26. The thermal parameters (heat conductivity, volumetric heat capacity, and thermal dispersivity (longitudinal and transversal)) of the existing geological units were

adapted during manual calibration. The parameter range used varied between 1.6 W m^{-1}/K and 6.8 W m^{-1}/K for thermal conductivity, between 1.8 MJ m^{-3}/K and 3.2 MJ m^{-3}/K for the volumetric heat capacity, and between 0.1 m and 1 m for the longitudinal thermal dispersivity following established literature values (VDI 4640/1, 2010; Abu-Hamdeh, 2003; Stonestrom and Blasch, 2003). Gelhar et al., (1992) summarized the studies existing at that time and showed that longitudinal dispersivity is bigger than transversal dispersivity, in the horizontal as well as vertical direction. In this model, the transversal dispersivity was set to 10% of the longitudinal value, which is a common assumption and experimentally supported by the study of Huang et al., (2003). To illustrate the uncertainties in simulated temperatures resulting from the given range in thermal parameters, two extreme scenarios were adopted representing good ability (minimum c and maximum λ) and limited ability (minimum λ and maximum c) of heat transport through the saturated porous media. The accuracy of temperature simulations was quantified by the deviation in the timing of the maximum summer temperature or the minimum winter temperature ($\Delta\Phi$) and by the availability and difference in temperature amplitude (ΔA) between simulated and observed temperatures. For these analyses, the measured groundwater temperatures of the group (iii) were used as they are assumed to be representative of the groundwater temperature and directly linked to the position of the filter screen of each observation well. Since no sampling data were available for W05 and W06 and instead, logger temperatures were used for calibration.

Chapter 3 Results of field observations including water chemistry

Direct plotting and analysis of the water head, temperature, and water chemistry data give a basic insight into the local flow field and thermal field before modeling research. The redox zone distribution can be directly displayed by plotting electron acceptors and DOC levels. Influence from the canal bed reconstruction superposed by the local heterogeneity is examined by comparing the results of before and after the reconstruction period. This chapter first emphasizes the data which can depict the flow field and its changes. The flow field is characterized by the water head, temperature profile, stable isotope, and the main cations and anions analysis. The redox zonation and the DOC decrease are interpreted accounting also for the electron acceptors concentration change. SUVA is introduced to see the difference on the potential of DBP formation. The range of the sampling and measurement results are listed in Table 3.1. Each measurement item was categorized into before the reconstruction and after the start of reconstruction (separately before and after 17th June, 2013). The two subchapters 3.1 and 3.2 are adopted from the published article in Hydrogeology Journal named 'Impact of river reconstruction on groundwater flow during bank filtration assessed by transient three-dimensional modelling of flow and heat transport' by Wang et al. (2020), which can be accessed online as https://doi.org/10.1007/s10040-019-02063-3.

3.1 Water head observations

The observed water head in the near-bank wells together with the water level in the canal is shown in Fig. 3.1a. Featured as a canal section with a relatively stable water level, the seasonal variation of canal stage during the sampling period was relatively small (29.17 m to 29.86 m a.s.l.). Especially after August 2013, the water table in the canal fluctuated only within a range of 20 cm. Influenced by the pumping activity from the nearby waterworks, the pattern of a losing stream was evident by the lower water heads in the observation wells than in the surface waters. Further along the groundwater flow path, the water heads dropped to below 25 m a.s.l when reaching the pumping wells, as it is shown in Fig. 2.1c. From the start of reconstruction, an increase of around 0.5 m in water heads could be observed in $W07_{LOW}$, W08, and $W09_{LOW}$, while there was no increase in the surface water levels. Also, it correlated with neither the observed daily precipitation (Fig. 3.1a) nor the remediation pumping activity, which started from the end of the reconstruction. They reached a relatively stable, though higher, plateau after about three months.

Table 3.1 Comparison of water quality between before reconstruction and after reconstruction in the study area, with specification of range from minimum ~ maximum value from the complete data set. The detailed sampling dates and the total sample numbers are shown in Tab. S1 in the appendix.

Samples	Temperature (°C)		DO (mg/L)		DOC (mg/L)		NO_3^- (mg/L)		NH_4^+ (mg/L)		Mn^{2+} (mg/L)		Fe^{2+} (mg/L)		SO_4^{2-} (mg/L)	
	BE*	AE**	BE	AE	BE	AE	BE	AE	BE	AE	BE	AE	BE	AE	BE	AE
River	0.30~ 26.70	0.57~ 25.50	3.15~ 13.48	3.66~ 14.44	7.20~ 12.00	2.50~ 11.00	LoQ# ~ 8.60	LoQ~ 9.56	0.01~ 0.55	0.08~ 0.36	0.01~ 0.23	0.01~ 0.15	0.01~ 0.19	0.00~ 0.10	125.00~ 179.00	129.00~ 230.42
U100	11.70~ 12.20	11.60~ 13.60	0.10~ 1.40	0.00~ 1.19	3.10~ 4.20	1.40~ 9.30	LoQ~ 1.15	LoQ~ 1.89	0.40~ 0.88	0.68~ 1.51	0.09~ 0.15	0.12~ 0.19	1.10~ 1.67	0.67~ 1.38	71.50~ 95.90	85.50~ 251.43
W03H	10.50~ 14.20	11.20~ 15.40	0.07~ 1.40	0.00~ 3.81	3.80~ 8.00	2.10~ 6.10	LoQ~ 1.15	LoQ~ 1.11	0.17~ 1.35	0.62~ 0.85	0.40~ 0.54	0.47~ 0.60	0.61~ 0.98	0.44~ 0.96	121.00~ 177.00	109.00~ 253.36
W03L	11.60~ 13.20	10.40~ 14.50	0.10~ 2.80	0.00~ 0.62	1.40~ 7.60	0.10~ 5.40	LoQ~ 1.23	LoQ~ 1.05	0.15~ 1.15	0.58~ 2.15	0.10~ 0.53	0.13~ 0.57	0.63~ 1.32	0.65~ 1.27	77.50~ 111.00	78.00~ 205.20
W04H	11.70~ 12.80	11.90~ 13.80	0.02~ 2.20	0.00~ 0.93	2.30~ 6.40	2.10~ 6.20	LoQ~ 1.17	LoQ~ 1.80	0.07~ 0.25	0.13~ 0.36	0.16~ 0.25	0.22~ 0.60	0.98~ 1.31	0.58~ 1.33	121.00~ 169.00	125.98~ 209.51
W04L	11.90~ 12.90	12.20~ 13.70	0.09~ 3.20	0.00~ 1.14	2.90~ 8.30	2.00~ 5.80	LoQ~ 3.41	LoQ~ 1.00	0.48~ 1.45	0.86~ 1.70	0.20~ 0.37	0.22~ 0.37	1.22~ 1.82	0.60~ 1.60	95.90~ 178.00	105.00~ 235.09
W07H	4.30~ 19.90	4.10~ 22.80	0.20~ 4.90	0.00~ 3.93	5.50~ 9.00	2.00~ 7.60	LoQ~ 8.99	LoQ~ 6.11	0.03~ 0.31	0.03~ 0.55	0.01~ 0.22	0.02~ 0.81	0.02~ 0.41	0.00~ 0.06	127.00~ 151.00	125.00~ 217.40
W07L	7.80~ 15.20	8.80~ 15.70	0.12~ 3.50	0.00~ 3.10	5.40~ 6.70	2.20~ 7.40	LoQ~ 4.26	LoQ~ 2.67	0.03~ 0.21	0.12~ 0.53	0.06~ 0.20	0.15~ 0.45	0.01~ 0.57	0.07~ 0.82	134.00~ 155.00	95.95~ 218.23
W08	9.70~ 14.30	5.30~ 19.90	0.10~ 0.80	0.00~ 1.15	5.20~ 6.60	1.80~ 9.30	LoQ~ 1.15	LoQ~ 1.86	0.03~ 0.41	0.12~ 0.70	0.29~ 0.37	0.23~ 0.31	0.92~ 1.21	0.47~ 1.04	130.00~ 147.00	77.72~ 244.40
W09H	10.40~ 13.10	8.70~ 16.40	0.10~ 1.80	0.00~ 2.21	5.40~ 5.90	1.30~ 19.30	LoQ~ 1.14	LoQ~ 1.05	0.23~ 0.59	0.51~ 1.32	2.95~ 3.42	2.90~ 3.73	1.05~ 1.52	0.49~ 1.16	123.00~ 173.00	65.50~ 230.12
W09L	7.80~ 15.20	8.80~ 15.70	0.12~ 3.50	0.00~ 3.10	5.40~ 6.70	2.20~ 7.40	LoQ~ 4.26	LoQ~ 2.67	0.03~ 0.21	0.12~ 0.53	0.06~ 0.20	0.15~ 0.45	0.01~ 0.57	0.07~ 0.82	134.00~ 155.00	95.95~ 218.23

* BE denotes to before reconstruction

** AE denotes to after reconstruction

LoQ denotes to limit of quantification

Different from W08 and $W09_{LOW}$, the increase of $W07_{LOW}$ started earlier than the starting of the reconstruction and then a noticeable drop occurred a few months after the completion of the reconstruction. This increase and drop can be separately attributed to the earlier work of the bank protection removal and a possible local reclogging process along its infiltration path. For the wells with longer distance or deeper screen elevation, $W03_{HIGH}$, $W03_{LOW}$, and U100 are shown in Fig. 3.1b. Featured as the deep near-bank well in the north, the water head in U100 was around 0.5 m higher than the deep well of $W03_{LOW}$ in the south. This indicates that the groundwater flow direction in the deeper aquifer can be from U100 or even further north towards the south. The water head in $W03_{HIGH}$ was about 1 meter lower than $W03_{LOW}$. The increase of the water head driven by the reconstruction can also be observed in W03 and U100 (Fig. 3.1b), and the amplitude was similar to the near-bank wells.

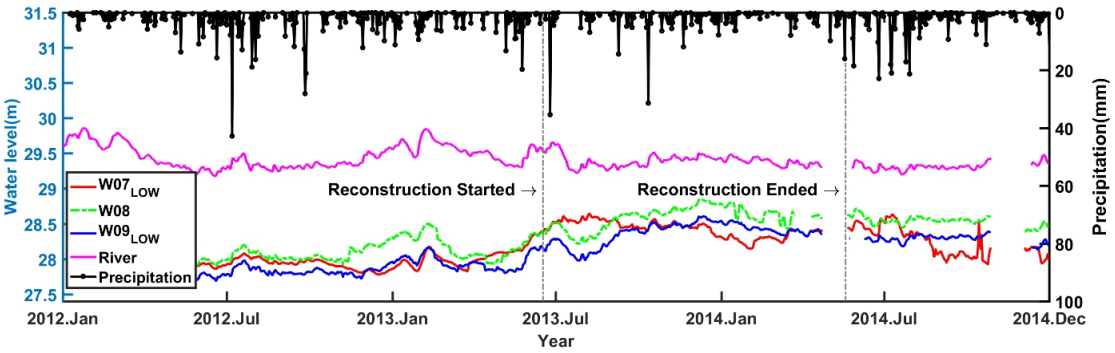

(a)

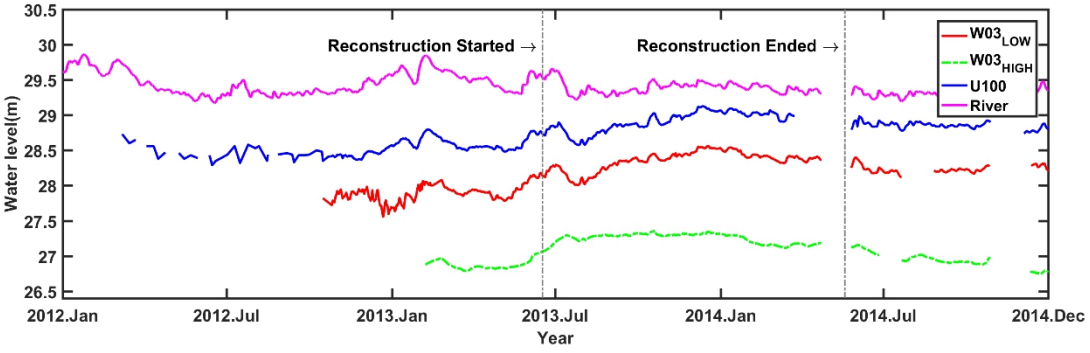

(b)

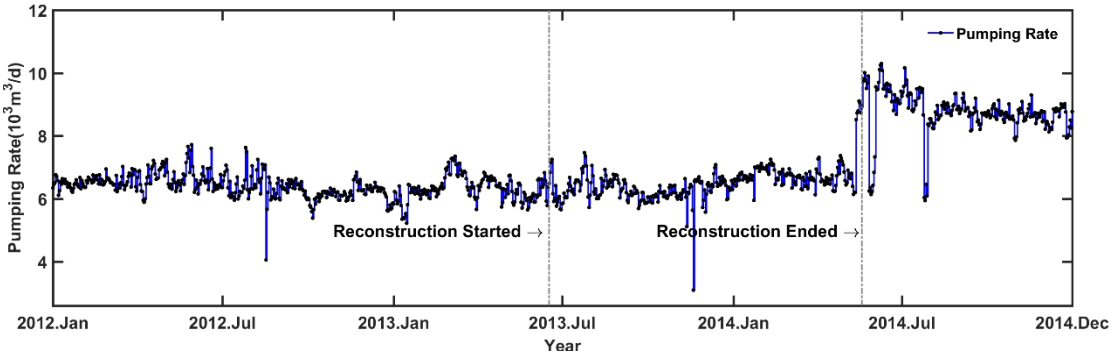

(c)

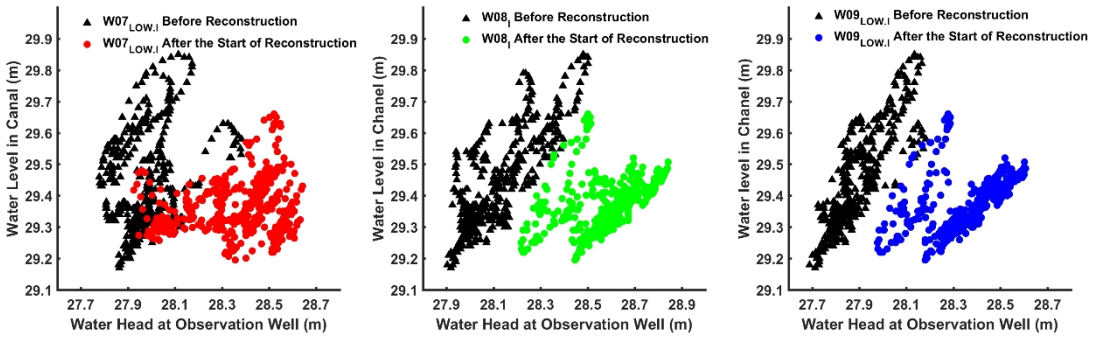

(d)

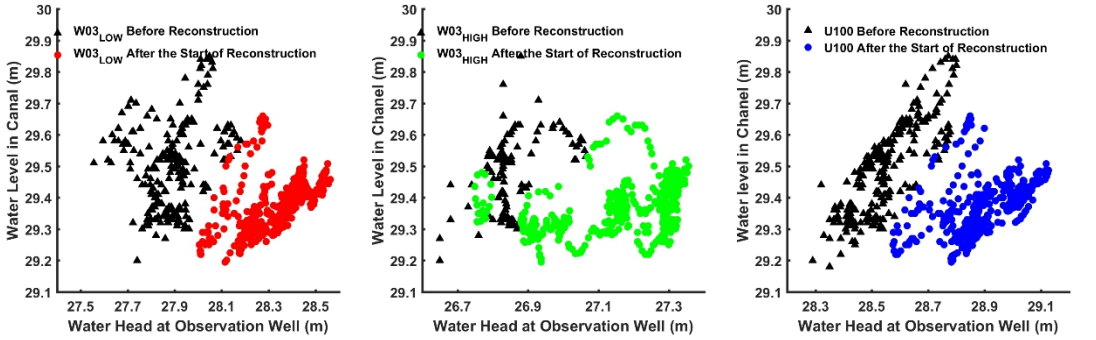

(e)

Fig. 3.1. a) The observed water head in ND canal and observation points $W07_{LOW}$, W08 and $W09_{LOW}$. b) The observed water head observation points $W03_{HIGH}$, $W03_{LOW}$ and U100. C) The total pumping rate from the water work. d) Scatter plot of water heads in observation wells $W07_{LOW}$, W08 and $W09_{LOW}$ versus water head in the canal. e) Scatter plot of water heads in observation wells $W03_{HIGH}$, $W03_{LOW}$ and U100 versus water head in the canal.

The change of the water heads from before- to after reconstruction can be better illustrated by a scatter plot of water heads between the observation wells and ND (Fig. 3.1d-e). These scatter plots of water heads can be separated into two or three groups shifted to larger values along the x-axis indicating larger groundwater heads. The three groups represent the periods i) before reconstruction, ii) during reconstruction work, and iii) after reaching a new plateau at the end of the reconstruction period. Most of the observation points behave similarly. This behavior may be attributed to either a coincidental earlier rise before reconstruction or a drop some months after completion of the reconstruction. Due to the the large dredging depth of the reconstruction work, both the internal and external colmation layers were completely removed. The low permeable glacial tills below the river bottom was also largely eliminated which might have created highly conductive windows and even continuous conductive areas. These changes can increase the hydraulic connection between the canal and aquifer. Given the pumping amount was operated with a groundwater abstraction similarly as before, this led

to a smaller hydraulic gradient needed to maintain the water flux towards the pumping wells and thus made the water heads between the canal and waterworks increase.

3.2 Temperature observations

As an annually periodic signal, the temperature time series collected by the logger roughly had the form of a sine function in the canal (Fig. 3.2). During the three-year sampling period, the temperature peaked at around 25 °C in summer and it's minima was approximately 0 °C in winter. This original signal was smoothed, damped, and delayed on its way from the infiltration at the canal bottom and banks to the observation wells. The distance from the well $W07_{LOW,}$ W08, $W09_{LOW}$ to the canal is similar, as well as the elevation of the data loggers installed inside the wells. The temperature patterns in those wells featured with significant differences in both amplitude and peaking time (Fig. 3.2a). The temperature in $W07_{LOW}$ varied from about 20 °C to 5 °C and showed the largest amplitude among the three. The temperature in $W09_{LOW}$ varied between 9 °C and 11 °C before reconstruction and 8 °C and 13 °C after reconstruction which was the smallest amplitude of the three wells. For the time shift, the peak time for $W07_{LOW}$ was delayed by weeks, but for W08 and $W09_{LOW}$, the pattern was shifted by months to a year. This indicates that there is a distinct thermal distribution along these three flow paths, where the propagation speed reaching W07 was much faster than the other two. At the more distant wells (Fig.3.2 b), the annual cycle was further damped in $W03_{LOW}$, and almost disappeared in $W04_{LOW}$ and the deep well of U100. In U100, the strongly averaged temperature pattern was around 1 °C lower than in $W04_{Low}$, which might have been caused by the difference in water composition. Part of the water flow in U100 might have originated from the pristine remnant groundwater in the north.

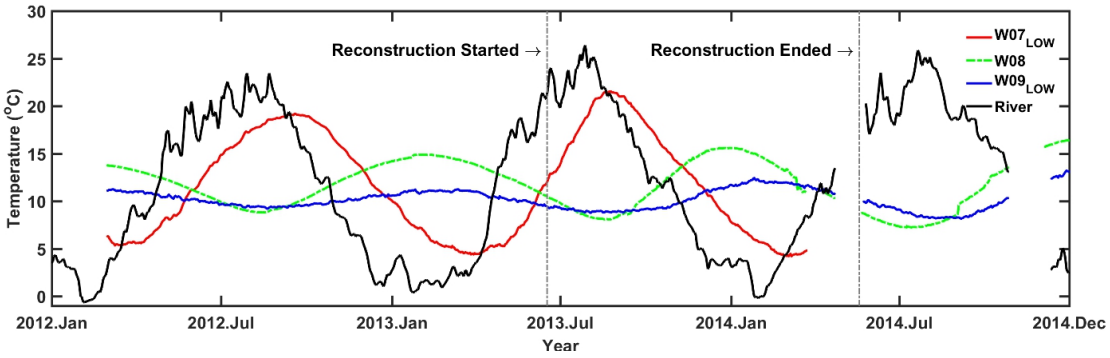

(a)

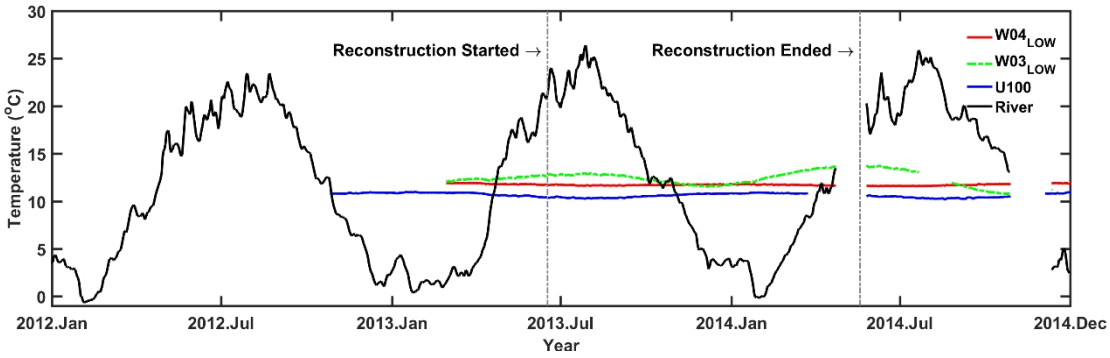

(b)

Fig. 3.2 The observed time series of temperatures in the canal and at observation points of a) $W07_{LOW}$, W08 and $W09_{LOW}$, b) $W03_{LOW}$, $W04_{LOW}$ and U100. All of the time series were measured with automated data loggers installed in the observation wells.

Vertical groundwater temperature profiles recorded after reconstruction are displayed in Fig. 3.3, where the topmost points reflect the temperature 5 cm below the soil surface, according to weather station data of Leibniz Institute of Agricultural Engineering and Bioeconomy (ATB). For W08 and $W09_{LOW}$, the temperature curves converge from the seasonally highly variable topsoil signal to a stagnation point with a narrow range (10.5~13.4 °C for W08, 11.7~13.1 °C for $W09_{LOW}$) that is near the groundwater table. However, they diverge again with increasing depth. This could reflect that there was a horizontal groundwater flow from the canal towards the pumping wells because the temperature signal from the land surface was damped prior to reaching the groundwater table. A similar principle was also applied in other studies for estimating surface water infiltrating into the aquifer (e.g., Duque et al. 2010; Ferguson & Woodbury 2005). For the temperature profiles close to the bottom, the amplitude and timing were similar between W08 and $W09_{LOW}$ and intensified downwards. Here, the temperature variations brought by the water flow combined with heat conduction were anticyclical to the surface temperatures and thus worked against the heat transferred via the vadose zone. In comparison of W08 and $W09_{LOW}$, there was a reduced amplitude and later arrival of the temperate variations at the data logger with continuous recording in $W09_{LOW}$.

However, this was due to the higher position of the data logger, which was much closer to the stagnation point.

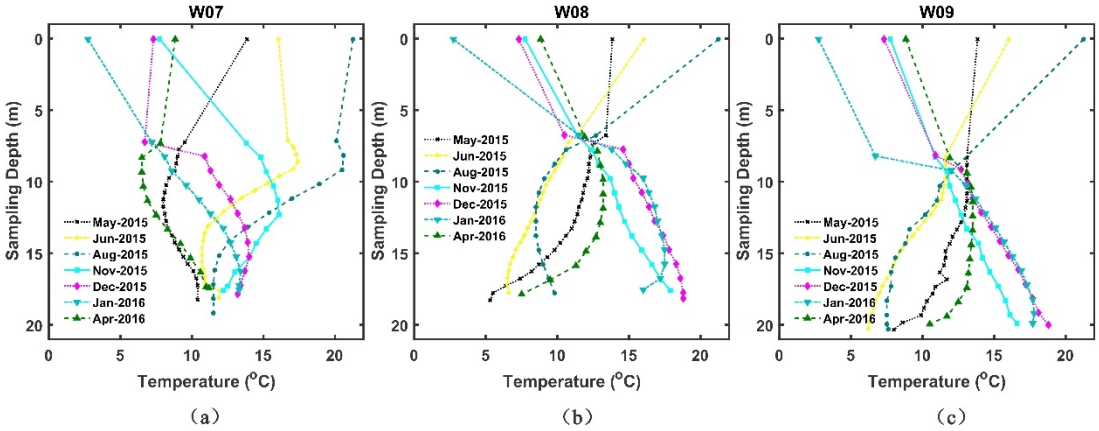

Fig. 3.3 Temperature profiles in three observation wells after the reconstruction. The various colorful dots denote to temperature data sampled in different depths during the sampling time-period. (a) is the temperature profile in $W07_{LOW}$, (b) is in W08, and (c) is in $W09_{LOW}$, respectively.

For $W07_{LOW}$, the temperature profile has an inverse shape compared to W08 and $W09_{LOW}$. The variation range reaches the largest within the first ten meters, then decreased with increasing depth. It shows a zone with modified profiles at just about the groundwater table and then converges to a steady temperature area at the bottom without significant shifts in timing throughout the profile. With similar external influences (precipitation, land cover, air temperature, etc.), this indicated that there was an influence by groundwater flow, but one which primarily occured at the top few meters below the groundwater table and little to none in the deeper parts of the profile. Altogether, this type of temperature profiling gave additional indications of the vertical distribution and strength of the groundwater flow which could be used as information for the groundwater flow model as well as a reference for the heat transport modelling.

3.3 Stable water isotopes

Different from heat, which can also propagate in water through conduction beside the advection, stable isotopes are the most conservative tracers since they transport as part of the water. Stable isotopes can better reflect the flow field condition. In this study, since the sampling of stable isotope data was ended shortly after the accomplishment of the canal reconstruction, the analysis of plotting results can only reflect the flow regime up to this time point. The moving average (window length covers four samples) of the $\delta^{18}O$ in four observation wells ($W03_{LOW}$, $W04_{LOW}$,$W07_{HIGH}$, U100) and the canal were plotted in Fig. 3.4a.

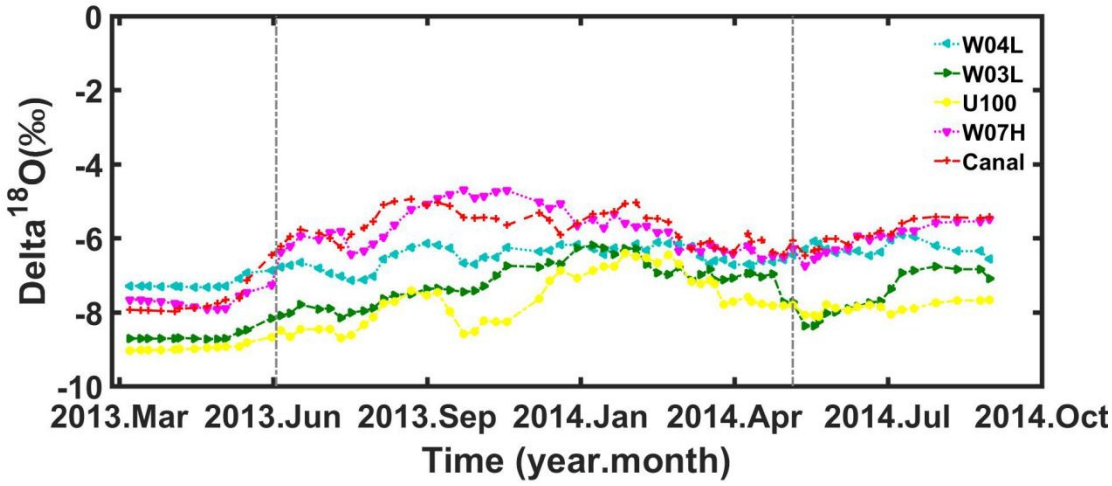

(a)

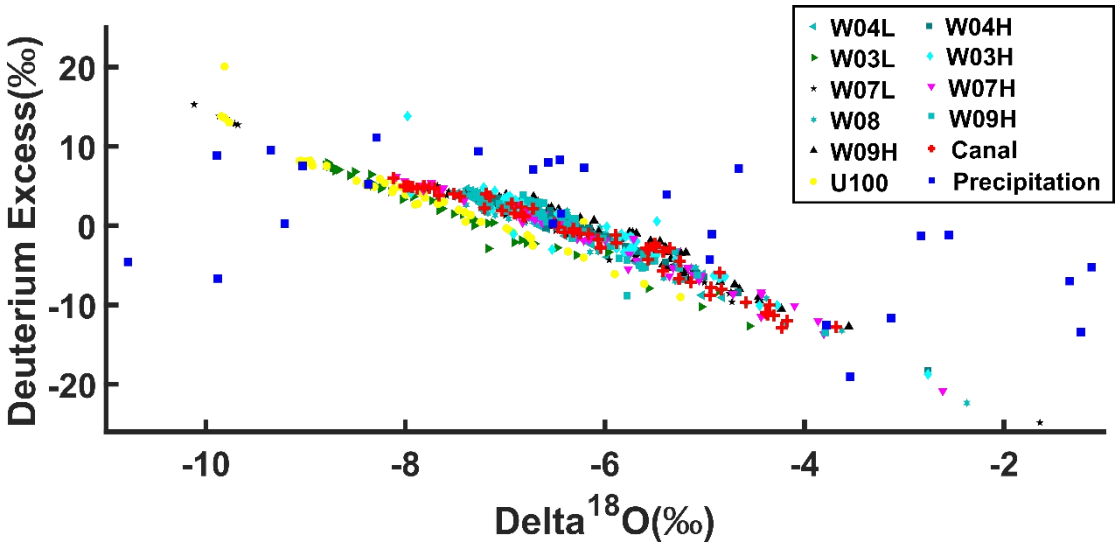

(b)

Fig. 3.4 a) Linear plot of delta ^{18}O for observation wells of $W03_{LOW}$ $W04_{LOW}$ $W07_{HIGH}$ U100 and the canal by a moving average with the window size of four (around one month). b) Scatter plot of deuterium excess versus delta ^{18}O for groundwater wells and local reference measurements in the canal.

Before reconstruction, the sampling results of all wells in the three months were stable, and the lowest $\delta^{18}O$ level was observed in deep wells of U100 and $W03_{LOW}$. The other deep well $W04_{LOW}$ showed the highest $\delta^{18}O$ level, while the near bank well of $W07_{HIGH}$ and canal were located in between. From the beginning of the reconstruction, the dynamic change of $\delta^{18}O$ occured in all observation wells. By January of 2014, the $\delta^{18}O$ measurement in the canal and $W07_{HIGH}$ climbed to the top, whereas $W04_{LOW}$ kept oscillating at a similar level as before the reconstruction. U100 and $W03_{LOW}$ remained the lowest. A rising trend occurred in both wells reaching the level of $W04_{LOW}$ by the beginning of 2014. From January 2014 to April 2014, the $\delta^{18}O$ in all wells showed the dynamic change in the overlapping area, except for U100,

which dropped in March 2014. After the completion of the reconstruction, $W04_{LOW}$ kept a similar $\delta^{18}O$ level as $W07_{HIGH}$ and SW, while U100 was maintained at the lowest level. $W03_{LOW}$ was located in between, except for a period between May 2014 to July 2014, when it fells as low as U100. It hinted that the water flow through $W07_{HIGH}$ could be traced back to the canal, while the deep wells $W03_{LOW}$ and U100 may be contributed by the same origin. After reconstruction, the water source of $W03_{LOW}$ was possibly shifted towards surface water, as its $\delta^{18}O$ level got closer to the canal and $W07_{HIGH}$. Limited by the sampling time both before and after the reconstruction, the origin of water flow through $W04_{LOW}$ is difficult to determine here, however, it is closer to the canal and $W07_{HIGH}$ than the other two deep wells. With the help of the water chemistry data analysis (mainly Piper plots), the water flow through W04 will be further investigated in chapter 3.4

By plotting all the observation wells together with the precipitation as $\delta^{18}O$ versus Deuterium excess (Fig. 3.4b), it is shown that the $\delta^{18}O$ is widely distributed but mainly between 4‰ and -9‰. Within this range, the sampling results of observation wells can be categorized into two groups. Results from all of the near-bank wells and the shallow distant wells together with the canal can form a large scatter indicatingthe dominant water source as the infiltrated Surface water (SW). Similar to the previous result from Fig. 3.4a, deep wells of both $W03_{LOW}$ and U100 showed overlap and deviated from other observation points. As it was discussed in Section 3.1, the hydraulic gradient between them suggested a continuous groundwater flow path from U100 to $W03_{LOW}$. For U100, in consideration of its distinct $\delta^{18}O$ level, it may be composed of the remnant landside groundwater from further north. Therefore, the composition of the water flow through the deep aquifer could be a mix of both the landside groundwater and newly infiltrated SW. The other deep well, $W04_{LOW}$, was mainly located within the scatter of the shallow water wells except for some points of low $\delta^{18}O$, which could be a mix of both, however with larger contribution from the SW. Based on this result, the local flow field in the RBF site can be categorized into two flows: 1) SW infiltration which was dominant in the shallow aquifer, and 2) deep aquifer flow from the north with a possible contribution from the infiltrated SW. By the difference in riverbed saturation condition, deep groundwater flow, etc., Hiscock and Grischek (2002) defined six different flow conditions for RBF sites. Different from the majority cases in which the deep groundwater flow is neglected, the RBF situation in this study can be categorized as the 3rd field type showing a groundwater flow below the canal and a saturated riverbed. A detailed categorization of RBF flow conditions can be found in Hiscock and Grischek (2002).

3.4 Water chemistry type

The sampling of water chemistry data after the reconstruction was done continuously and frequently only in the year 2016 and 2017. The data from this period was used to evaluate the

water chemistry conditions and their change caused by the reconstruction. Piper plots were used as a first evaluation method. As shown in Fig. 3.5, the point distribution of all wells and surface water was located nearby the boundary between calcium sulfate water and calcium bicarbonate water. Before the reconstruction, as the representative of mixture between remnant landside groundwater and infiltrated SW, U100 featured a lower proportion of Cl^- and SO_4^{2-} than water sampled from the canal in the anions distribution (Fig. 3.5). It could be grouped as the type of calcium bicarbonate water. The water sampled in the canal was distributed across both water types with samples of calcium sulfate water being the majority. All the near-bank wells (W07, W08, W09) and the shallow distant wells ($W04_{HIGH}$, $W03_{HIGH}$) could be categorized as calcium sulfate water, which was closer to the SW than to the U100. It was consistent with the result from the stable isotope analysis that the flow in the shallow aquifer was dominant by the SW infiltration. For deeper wells, the sample distribution of $W03_{LOW}$ overlapped largely with the position of U100, and the water type was therefore grouped as calcium bicarbonate water before the reconstruction. Similar to the plotting result of the SW, the plotting result of W04 distributed right at the border between the two water types before the construction, higher in the concentration of Cl^- and SO_4^{2-} than in $W03_{LOW}$ and U100.

After the reconstruction, there was a general rise in the share of Cl^- and SO_4^{2-}. In the canal water, the sample result was still at the border between the calcium sulfate water and the calcium bicarbonate water; however, closer to the calcium sulfate water. For U100, the water type continued like the condition before the reconstruction. Some samples lay in the domain of calcium sulfate water type. For the near-bank wells (W07, W08, W09) and the shallow distant wells ($W04_{HIGH}$, $W03_{HIGH}$), the water remained calcium sulfate water, which was closer to the water of the canal. For wells in the deep aquifer ($W03_{LOW}$, $W04_{LOW}$), a strong rise of around 20% in the share of Cl^- and SO_4^{2-} could be observed, which drove the shift from calcium bicarbonate water to calcium sulfate water. The distribution position of water type became closer to the SW than to U100. The change in the plotting pattern indicated a variation in the flow field. In the shallow aquifer, since the water source was still SW infiltration, the plotting pattern was consistent with the condition before the reconstruction. However, the increasing infiltration rate caused by the rising canal bottom permeability could not be depicted by this piper plot result since the water chemistry in those wells were dominated by the SW continuously. In the deeper aquifer, the change can be shown by the rise in the share of Cl^- and SO_4^{2-}. This indicated an increasing contribution ratio of the infiltrated canal water in the deep flow path caused by the reconstruction, which was mainly caused by the increasing net canal bed permeability.

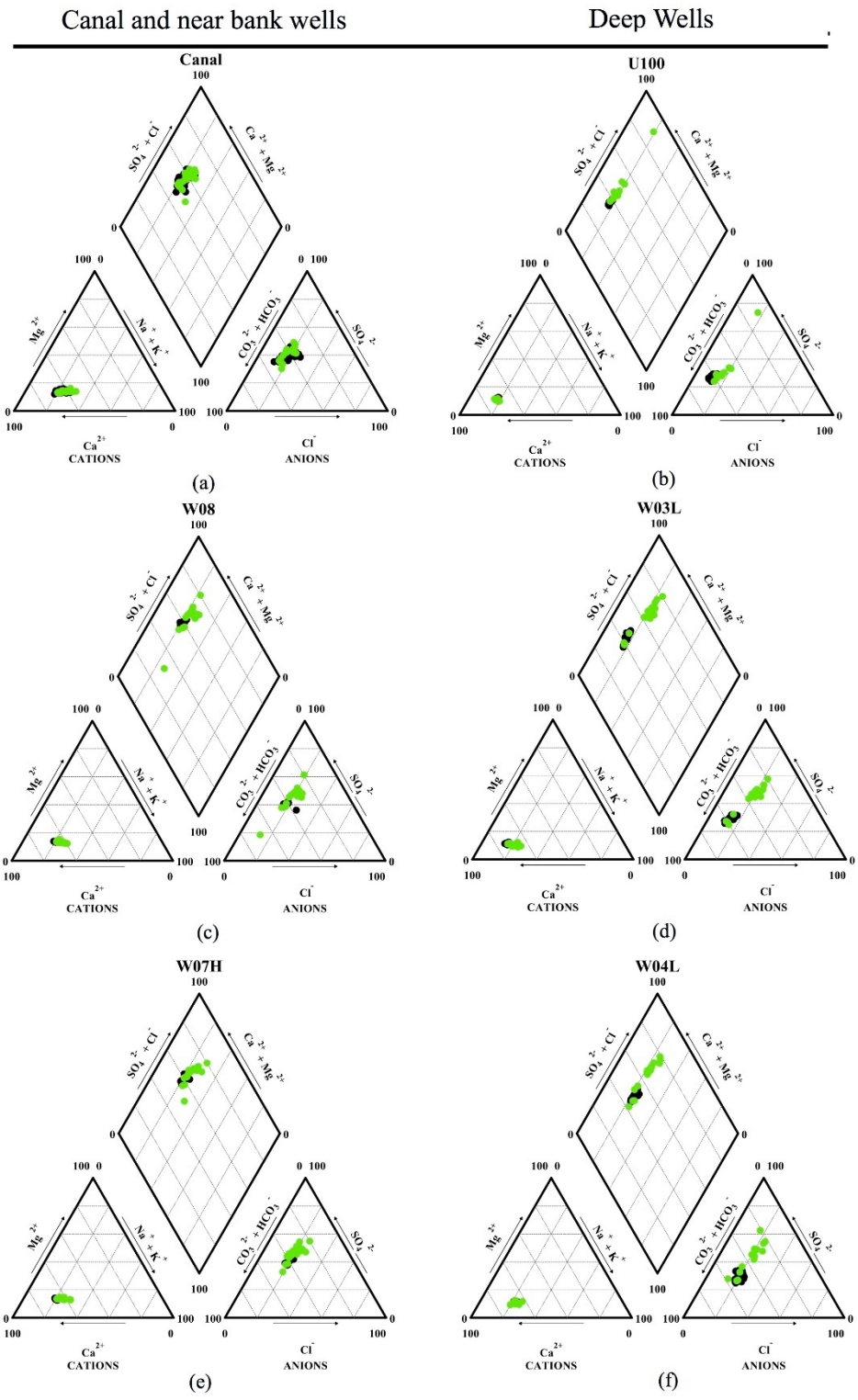

Fig. 3.5 Piper plot showing groundwater geochemistry from different observation wells, where black points stand for data sampled before canal reconstruction, while green points stand for data sampled after reconstruction.

3.5 Redox zonation, ammonium, DOC removal

The redox zone distribution in the RBF site was influenced by both the canal bed reconstruction and the local hydrogeological heterogeneity. The presentation is in the order of the electron acceptors together with ammonium and then the organic matter (DOC and SUVA). The comparison of electron acceptors was classified into two groups: before and after the start of the reconstruction. Due to the potential seasonal dynamic of DO and nitrate, the result for comparison will be shown as time series (Fig. 3.7-3.10). For NH_4^+ and the electron acceptors of Fe^{2+}, $Mn^{2+,}$ and SO_4^{2-}, few studies so far have shown the seasonal dynamic and the sparse sampling frequency in our research also limited examining the seasonal dynamics before reconstruction. Therefore, violin plots were adopted for displaying the sampling result before and after reconstruction (e.g., Fig. 3.8). Standard boxplots are shown within the violin plots. The hinges cover the first and third quartiles (the 25th and 75th percentiles) and the whiskers extend an extra 1.5 times the interquartile range from the upper and lower hinges. The values located outside were considered as outliers. A two-sides Wilcoxon-rank-sum test (Wilcoxon, 1945) was used to test whether the change is statistically significant. The null hypothesis (H_0) being tested is: 'There is no substantial change between the sampled result before the reconstruction and after the start of the reconstruction'. The results of statistical hypothesis testing were listed in Tab. 3.3, where the statistically significant results ($P < 0.01$) were highlighted in grey. The median value for some of the electron acceptors Mn^{2+}, SO_4^{2-}, Fe^{2+}, together with ammonium and DOC were listed in Tab. 3.2. The whole test was carried out in the R language.

Table 3.2 Median value for part of the cation and anions, 'Before' stands for before the reconstruction and 'After' stands for after the start of the reconstruction. The red, yellow and green colors stand for increasing, constant and decreasing concentration, respectively. The number of samples for calculating these concentrations are shown in Tab. S1

	NH_4^+ (mg/L)		Mn^{2+} (mg/L)		SO_4^{2-} (mg/L)		Fe^{2+} (mg/L)		DOC (mg/L)	
	Before	After	Before	After	Before	After	Before	After	Before	After
Canal	0.16	0.18	0.07	0.05	146	194	0.05	0.02	8.90	7.60
U100	0.49	1.33	0.12	0.14	85	104	1.29	0.88	3.75	3.75
W03H	0.88	0.78	0.52	0.54	144	171	0.74	0.64	5.55	5.20
W03L	0.88	1.78	0.13	0.15	93	186	1.18	0.94	3.20	3.95
W04H	0.15	0.28	0.21	0.25	146	182	1.14	1.06	5.00	5.00
W04L	1.02	1.18	0.28	0.26	130	185	1.55	0.96	5.20	4.70
W07H	0.05	0.21	0.05	0.46	133	196	0.02	0.00	6.50	5.06
W07L	0.09	0.31	0.18	0.29	136	164	0.18	0.53	6.25	5.60
W08	0.11	0.44	0.31	0.27	137	199	1.04	0.59	5.70	5.55
W09H	0.44	0.71	3.22	3.16	147	173	1.26	0.77	5.70	5.60
W09L	0.56	0.35	1.12	1.55	127	197	1.43	1.27	5.75	5.28

Table 3.3 Statistical test results for the significance of the difference in mean concentration before the reconstruction and after the start of the reconstruction. Significant results ($P < 0.01$) are highlighted in grey. The number of samples for calculating the ions and DOC are shown in Tab. S1.

	NH_4^+	Mn^{2+}	SO_4^{2-}	Fe^{2+}	DOC	ETC
Canal	0.598821	0.342205	0.000002	0.000265	0.000002	0.011608
U100	0.000064	0.039527	0.000418	0.002691	0.782050	0.413471
W03H	0.098034	0.002311	0.117090	0.018674	0.085586	0.012933
W03L	0.000585	0.000033	0.000115	0.000175	0.103953	0.004359
W04H	0.000046	0.000012	0.026494	0.033277	0.952690	0.000218
W04L	0.047102	0.092498	0.001897	0.000008	0.151534	0.000103
W07H	0.013214	0.000169	0.000614	0.018161	0.026825	0.748616
W07L	0.000171	0.000373	0.001882	0.011649	0.061441	0.886701
W08	0.000124	0.002036	0.004481	0.000161	0.166815	0.006977
W09H	0.000106	0.637612	0.184668	0.000039	0.941502	0.132318
W09L	0.052315	0.000099	0.001150	0.173405	0.461500	0.005327

As it is shown in Tab.3.2, in general, a global decrease of the median concentration is seen in DOC and Fe^{2+}, while most of the increasing trend is demonstrated by NH_4^+, Mn^{2+} and SO_4^{2-}. For NH_4^+ and Mn^{2+}, the median concentration was very low, which was mainly within the 0.5 mg/L, both before and after the reconstruction, while for Fe^{2+}, the median concentration was higher but still be around 1 mg/L. Therefore, the change in those cation and anions were small in absolute value. As one of the main anions, the median concentration of SO_4^{2-} had a maximum near 200 mg/L and the absolute change is larger than NH_4^+, Mn^{2+} and Fe^{2+}. DOC median level which varied between 5 to 10 mg/L. Taking $P<0.01$ as the threshold for determining the significant change, the results are shown in Tab.3.3. More than half of the sampling items in different wells showed significant change ($P<0.01$, Tab. 3.3) after the reconstruction, which was mainly cations and anions. DOC acted as an exceptional case, where the change was only significant in SW. The detailed study of those water quality items will be later in this chapter.

3.5.1 pH

The pH was taken in three selected sampling wells. Together with the canal this was plotted in Fig. 3.6. pH value in the canal shows the most considerable variation, which varies mainly between 7 to 8.5. The highest pH was measured in July and August of 2009, which were separately 8.88 and 8.68, while the lowest value of 6.75 was measured in December 2011. The near-bank well $W07_{HIGH}$ and the distant well $W04_{LOW}$ showed a similar pH level, which was around 7.5, and the variation range was smaller compared with the SW. A larger dynamic was observed in the last year the data was available and the minimum pH was still above 6.5. Among observation wells, the highest pH level was observed in $W09_{LOW}$, which was on

average 7.8. There was neither evident seasonal trend along the whole sampling period nor apparent change after the reconstruction observed. This suggests a relatively stable and neutral pH level along the entire study period.

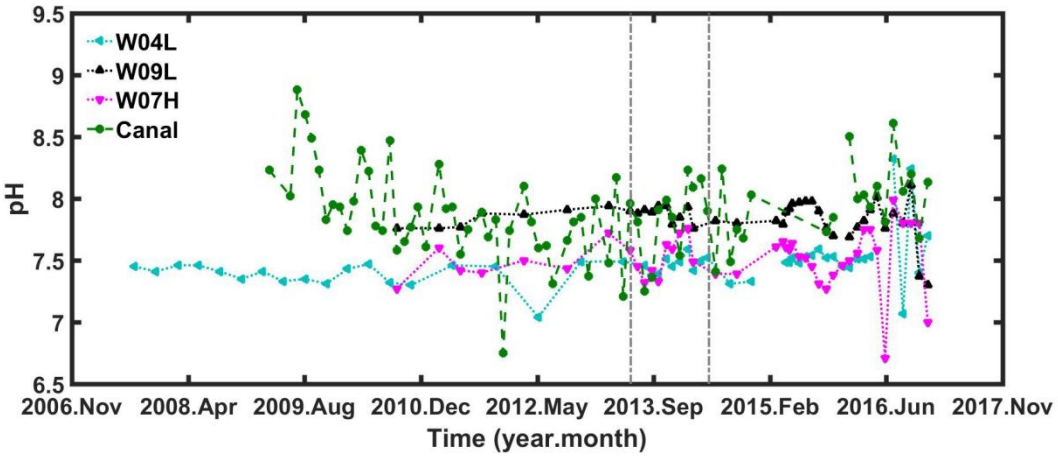

Fig. 3.6 Linear plot of pH for observation wells of $W04_{LOW}$, $W07_{HIGH}$, $W09_{LOW}$, and the canal.

3.5.2 DO

For the DO source in the groundwater of an RBF site, Kohfahl et al. (2009) also proposed three additional possible oxygen sources besides the infiltrating surface water: 1) infiltrating precipitation, 2) the entrapment of air due to the dynamic variation of the groundwater table, and 3) diffusive oxygen flux. For the infiltrated water along the flow path, DO was consumed first before other alternative electron acceptors (Gross-Wittke et al., 2010), while the aerobic condition can last from centimeter-level to kilometer-level (Kedziorek et al., 2008).

The difference in the flow path could play a decisive role in determining DO consumption. According to the analysis of the samples, the seasonal variation range of the temperature and DO concentration in SW were generally higher than in GW (Fig. 3.7). For SW, seasonal variations range of DO and temperature were 3.15-14.44 mg/L and 0.3-26.7 °C, respectively; for GW, the DO was in general below 2mg/L, most closely to 0 mg/L, except for $W07_{HIGH}$. While for seasonal temperature dynamic the varation range was between 4.1-22.3 °C ($W07_{HIGH}$) and 11.0-13.6 °C (U100). There was a negative correlation relationship between DO and temperature in both the SW sample and $W07_{HIGH}$ (Fig. 3.7a, b). Whereas it was not observed in other wells (Fig. 3.7c-3.7f). Except for $W07_{HIGH}$, the DO kept an extremely low concentration in the GW and even decreased to zero in most of the time (Fig.3.7c-3.7f). Two time-periods of general DO rise can be observed. The first one is from April 2013 to May 2013, before the reconstruction. The second general oxygen rise period is from August 2013 to November 2013, during the reconstruction period. It showed lower DO concentration than

the previous one, however with great variation. By reviewing the raw data, the higher values of the abovmentioned two periods originated from the *in situ* measurements. They could be attributed to the pumping process during the field sampling, which might reaerate the sampling tank and further lead to the rise of DO. Single high DO values in W09 were also present, but are likely to be attributed to sampling errors, e.g., air bubbles trapped during sampling before going to analysis in the lab and thus have to be considered as outliers.

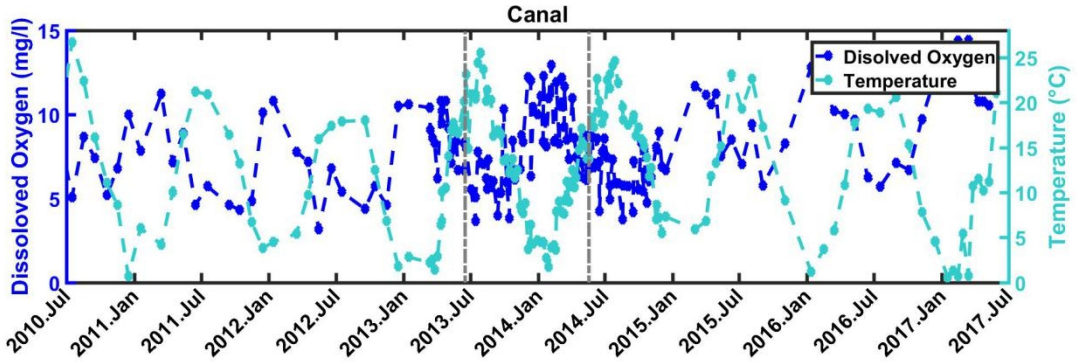

(a)

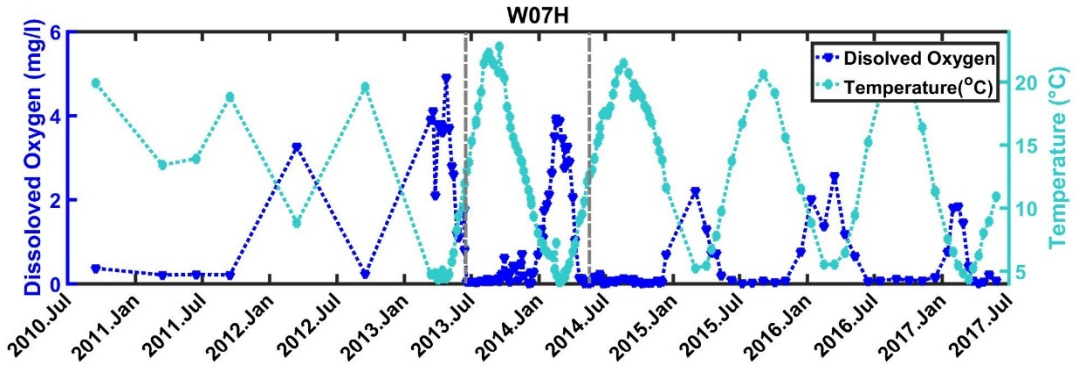

(b)

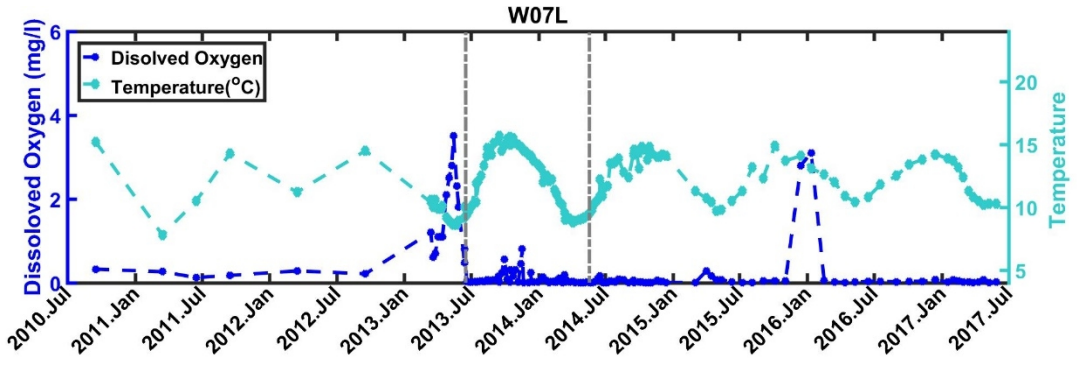

(c)

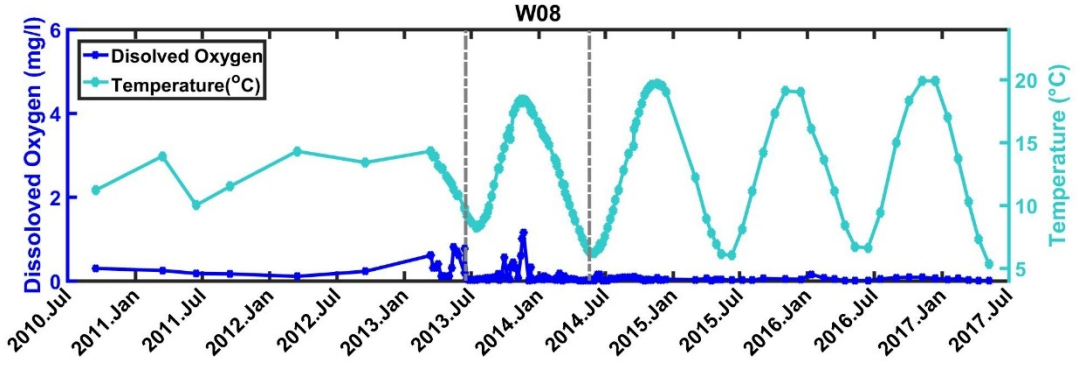

(d)

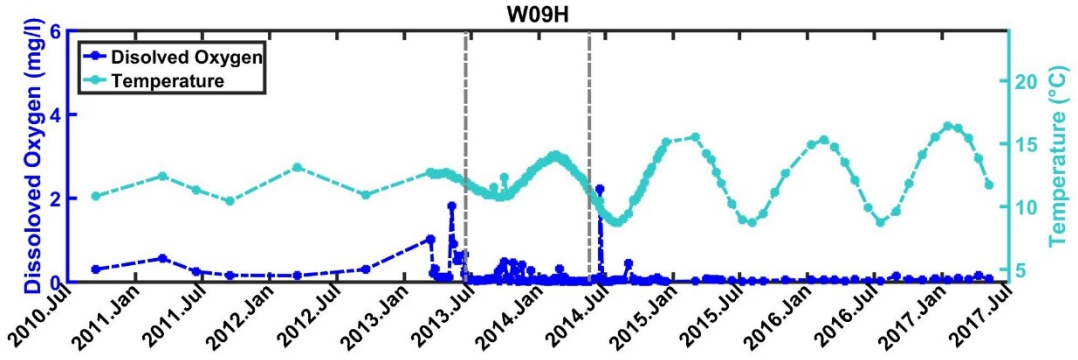

(e)

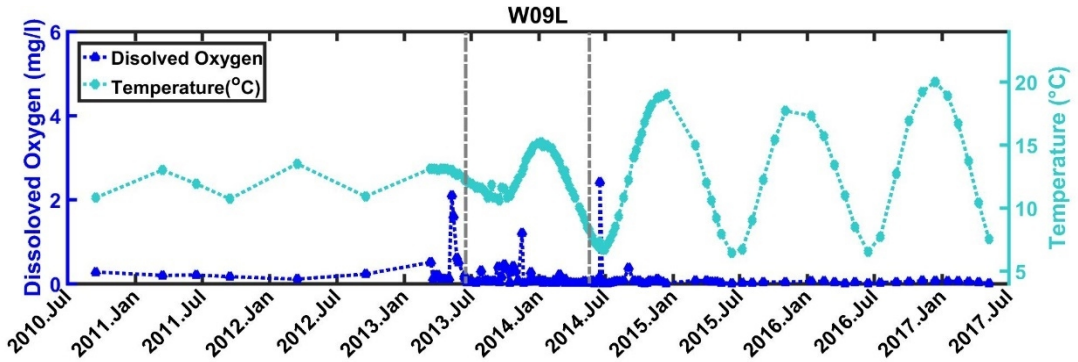

(f)

Fig. 3.7 The variation of dissolved oxygen (DO, mg/L) and temperature (°C) in the canal (a) and observation wells $W07_{HIGH}$, $W07_{LOW}$ (b, c), W08 (d), $W09_{HIGH}$, $W09_{LOW}$ (e, f). Blue dots denote to DO; cyan dots denote to seasonal variations of temperature. The two grey dashed lines in June 2013 and May 2014 represent the reconstruction period in the ND.

Variations of the oxic zonation caused by the reconstruction were only evaluated in $W07_{HIGH}$ since the DO level was close to zero in all other observation wells. Consistent with the seasonal dynamics, the observed DO level in $W07_{HIGH}$ declined in winter after reconstruction. The DO level reached the maximum at the first tenable seasonal peak in the winter of 2014 and then dropped drastically in the winter of 2015 (Fig. 3.7b). Later in 2017, with the highest measured DO level in the surface water, the observed value in $W07_{HIGH}$ was the lowest. This

indicated a larger consumption rate of DO as the electron acceptor and a larger scale of biochemical reaction in the wintertime along the flow path to $W07_{HIGH}$.

Comparing two near-bank wells, W07 and W09, which shared similar distance to the canal and similar screen elevation (Tab.2.1), two individual horizontal and vertical DO patterns could be observed (Fig. 3.7b-3.7f). In general, $W07_{HIGH}$ (BR: 0.20-4.90 mg/L, AR: 0.00-3.93 mg/L) showed a larger DO variation than $W09_{HIGH}$ (BR: 0.10-1.80 mg/L, AR 0.00-2.21 mg/L) (Fig. 3.7b and 3.7e). This clear difference between $W07_{HIGH}$ and $W09_{HIGH}$ can be generated by the heterogeneity of geological composition between these two wells, which could be hinted at by temperature profiles (Fig. 3.3). In general, it suggested a much shorter traveling time in $W07_{HIGH}$. Vertically, the stratification of DO pattern between $W07_{HIGH}$ and $W07_{LOW}$ was observed, especially after excavation, which is similar to other investigations (e.g., (Massmann et al. 2008)). In contrast, both $W09_{HIGH}$ and $W09_{LOW}$ shared analogous DO concentration. This suggested that the sluggish groundwater flow to $W09_{HIGH}$ and $W09_{LOW}$ might supply enough retention time for the aerobic reaction on both wells. In contrast, for $W07_{HIGH}$ and $W07_{LOW}$, a tipping point might exist between the difference in traveling times which would shift the redox reaction further into the suboxic phase.

Different from the near-bank wells, the distant wells and the deep wells showed much smaller temperature variation amplitude and was even unobservable for W04 and U100 (Fig.3.8a, d, e). The DO level in all the wells was mostly close to 0 mg/L. A general oxygen rise was observed over the same period as the near-bank wells. This can be explained as the above-mentioned in situ sampling error. The low DO level in those wells also hinted that there was no reaeration process, similar to the aforementioned infiltrating precipitation or entrapment of air after the infiltrating water passing the near-bank wells. This indicated a relatively close groundwater system in this RBF field.

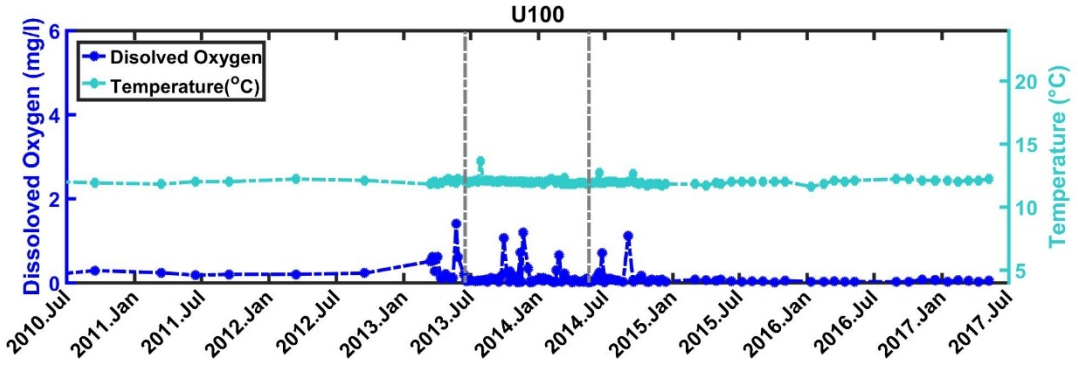

(a)

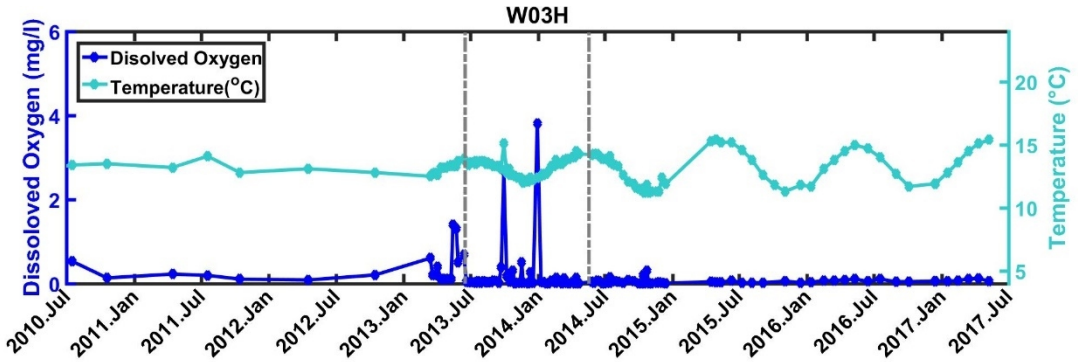

(b)

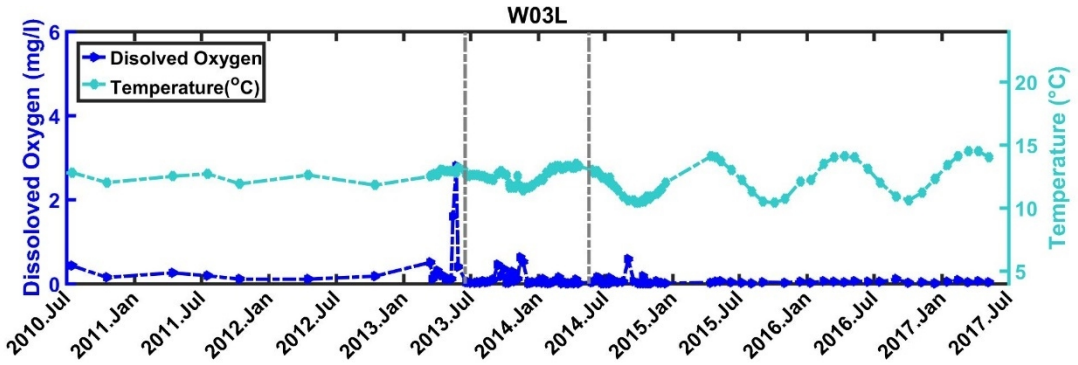

(c)

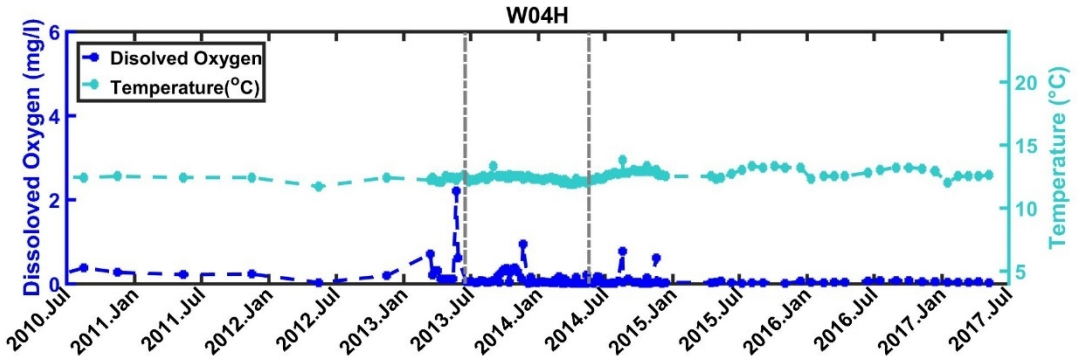

(d)

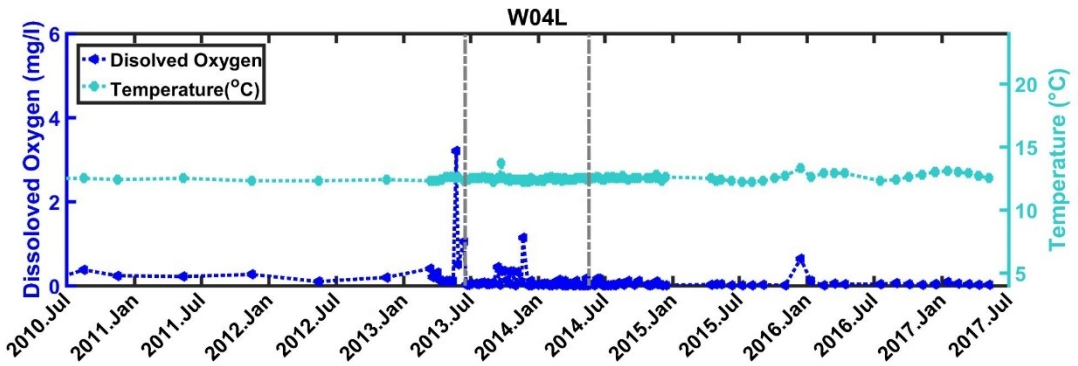

(e)

Fig. 3.8 The variation of dissolved oxygen (DO, mg/L) and temperature (°C) in U100 (a) and observation wells $W03_{HIGH}$, $W03_{LOW}$ (b, c), $W04_{HIGH}$, $W04_{LOW}$ (d, e). Blue dots denote to DO; cyan dots denote to seasonal variations of temperature. The two grey dashed lines in June 2013 and May 2014 represent the period of reconstruction in the ND.

3.5.3 Nitrate

An important function of RBF is to decrease the nitrate concentration by the redox reaction as nitrate is the next electron acceptor when oxygen is used up (Bourg and Bertin, 1993). Denitrification is considered as the most vital reaction consuming nitrate (Aravena and Robertson, 1998), while investigations also showed that the dissimilatory nitrate reduction to ammonium (DNRA) process could also be accounted for declining nitrate concentrations under anaerobic condition (Grau-Martínez et al., 2017). Between them, Korom (1992) mentioned that denitrification is favored in groundwater systems over DNRA. Besides the organic matter, an investigation by Brunet and Garcia-Gil (1996) showed that inorganic compounds, such as H_2S, could also be used as an electron donor for facultative anaerobic autotrophic denitrification. It was observed in the later study at an RBF site in Saxony, Germany (Grischek et al., 1998; Mallen et al., 1998), where Mn^{2+}, Fe^{2+} and HS^- acted as the electron donors to decrease the nitrate concentration. The process of nitrification and aerobic organic matter degradation could increase the nitrate concentration (Jacobs et al., 1988).

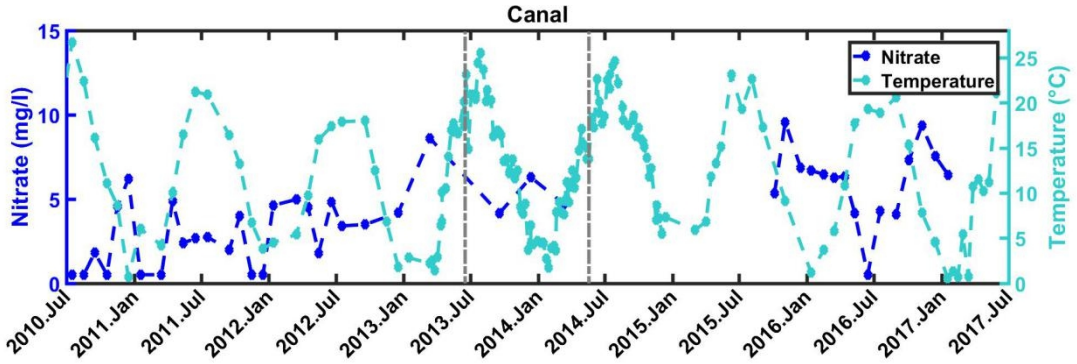

(a)

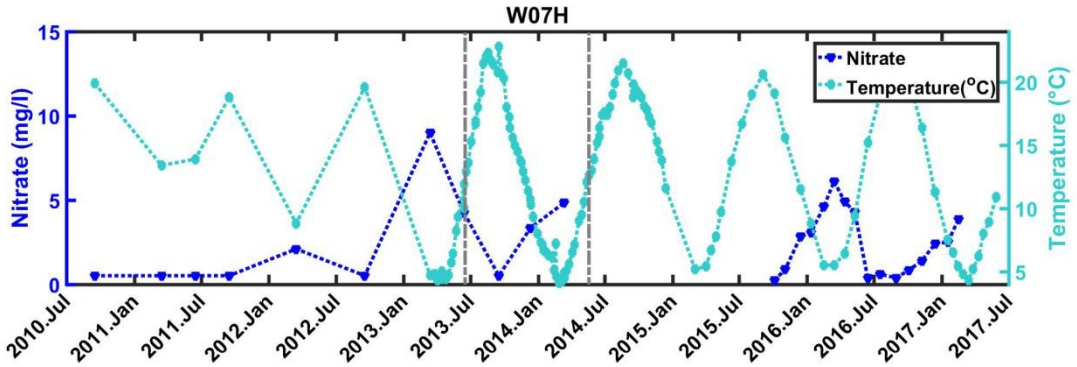

(b)

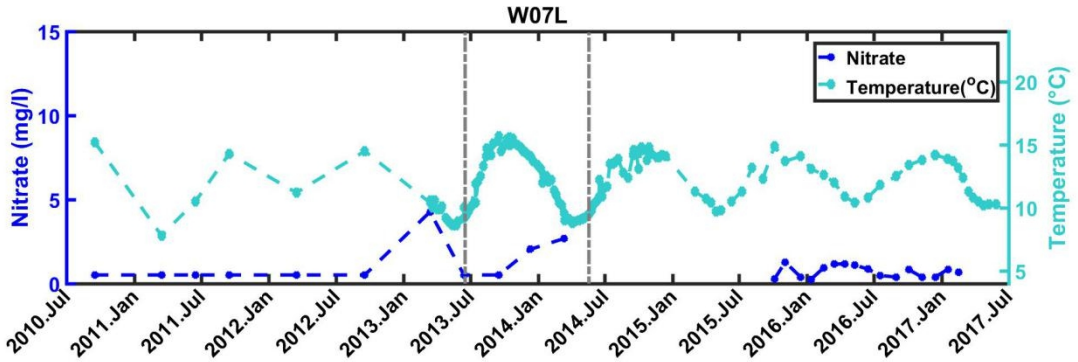

(c)

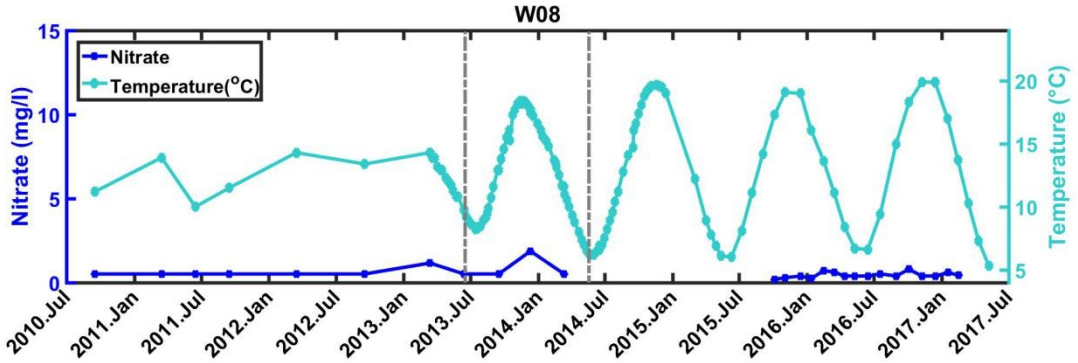

(d)

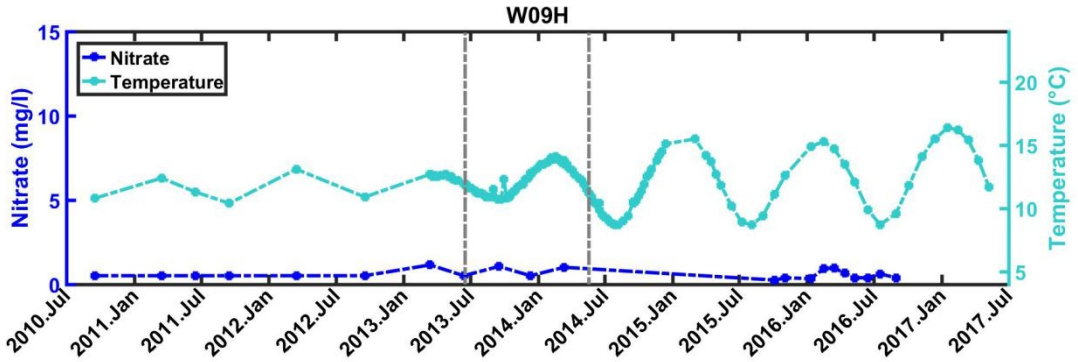

(e)

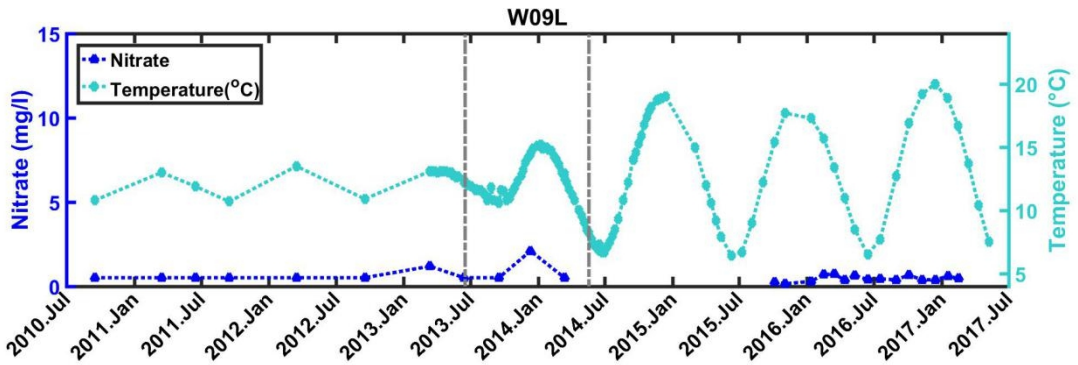

(f)

Fig. 3.9 The variation of nitrate (NO_3^-, mg/L) in the river (a) and observation wells $W07_{HIGH}$, $W07_{LOW}$ (b, c), W08 (d), $W09_{HIGH}$, $W09_{LOW}$ (e, f). Blue dots denote to NO_3^-; cyan dots denote to seasonal variations of temperature. The two grey dashed lines in June 2013 and May 2014 represent the period of reconstruction.

As it is shown in Fig. 3.9a, there was a dynamic change of nitrate concentration in the river water identified from October 2015 to February 2016 when sampling frequency was high. This showed a negative relationship with temperature. A similar pattern was observed in other studies (Doussan et al., 1997; Grischek et al., 1998; Massmann et al., 2008a, 2006, 2004) and was explained by the joined influence from the consumption of nitrate by algae in the waterbody, in the biological active siltation zone, and the decreased nitrate runoff caused by agriculture activity during the summertime. (Grischek et al., 1998; Massmann et al., 2008a). Compared with surface water (Fig. 3.9a), the NO_3^- concentrations were low in most of the near-bank wells except $W07_{HIGH}$ sometimes even below the limit of quantification (1 mg/l) until 2014 (Fig. 3.9c-3.9f). Seasonal variation of the NO_3^- concentration could only be observed in W07 after the reconstruction as for DO. This could have happened beforehand, though without being captured by the coarse sampling frequency. It was in accordance with the negative correlation existing in the canal which indicates a seasonal dynamic of the redox zonation and short residence time (Fig. 3.9b). This analogous dynamic pattern has been observed in other studies (Kedziorek et al., 2008; Massmann et al., 2008a, 2006, 2004; Pan et al., 2018). The spatial distribution differences of NO_3^- concentration in W07 and W09 was similar to the case of DO. Vertical spatial distribution of NO_3^- concentration was different in the wells which shared a similar distance to the ND (W07, W08 and W09). For example, for W07, NO_3^- concentration in the depth of 10-12 m was higher than in the depth of 15.5-17.5 m ($W07_{HIGH} > W07_{LOW}$). While for W09, NO_3^- in the depth of 16-18 m was similar to the depth of 10.5-12.5m ($W09_{LOW} \approx W09_{HIGH}$). A similar situation also happened in the study of the river Lot (Kedziorek et al., 2008) where the well with a shorter distance to the river showed much lower DO and nitrate concentration along with higher dissolved manganese concentration than more distant wells.

For distant and deep wells the nitrate level was mostly close or even below the limit of quantification (Fig. 3.10). Similar results were also shown in other investigations (e.g., (Hoppe-Jones et al., 2010; Kwon, 2015b; Massmann et al., 2004; Su et al., 2018; Wu et al., 2007)). This hinted that a good nitrate degradation ratio existed at this RBF site and the supply of the organic carbon outweighed the aerobic and anoxic electron acceptors. This would lead to more reducing conditions further along the flow path. Limited by the low measurement frequency, no conclusion could be drawn on the influence of the reconstruction. However, the nitrate removal efficiency in this RBF site was still kept at a constant high level after reconstruction. This could be shown by a low nitrate level in most of the near-bank wells and distant wells.

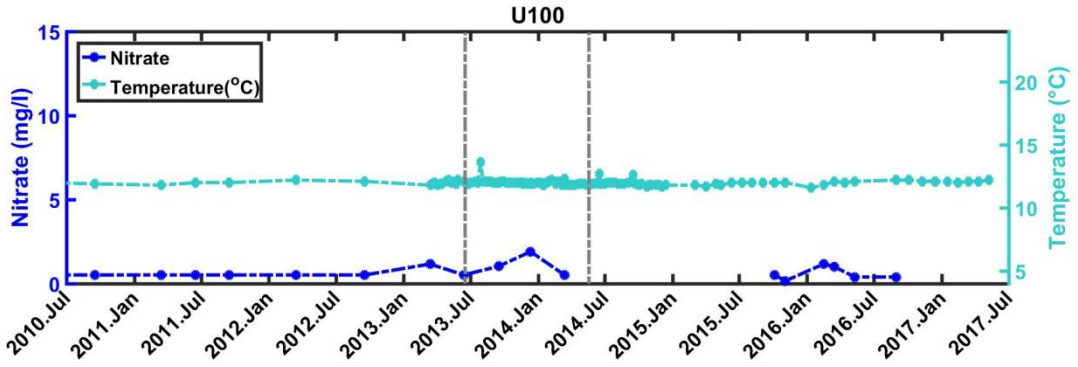
U100
Nitrate
Temperature(°C)
Nitrate (mg/l)
Temperature (°C)
0
5
10
15
20
2010.Jul
2011.Jan
2011.Jul
2012.Jan
2012.Jul
2013.Jan
2013.Jul
2014.Jan
2014.Jul
2015.Jan
2015.Jul
2016.Jan
2016.Jul
2017.Jan
2017.Jul

(a)

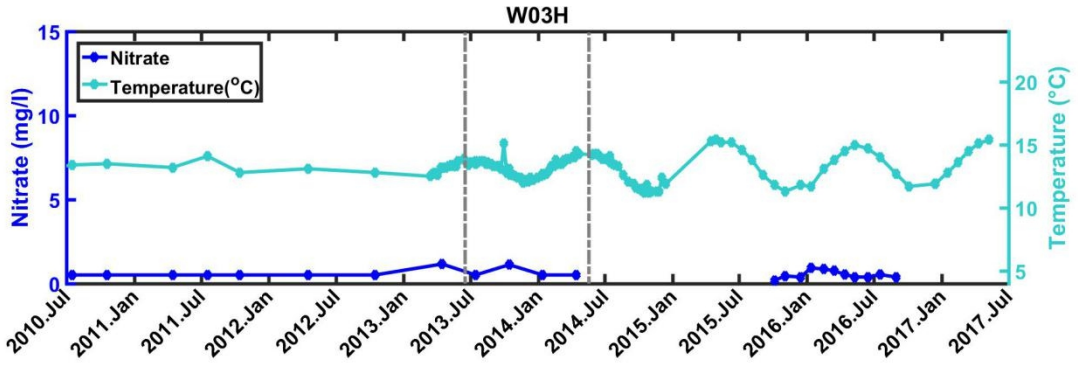
W03H
Nitrate
Temperature(°C)
Nitrate (mg/l)
Temperature (°C)
0
5
10
15
20
2010.Jul
2011.Jan
2011.Jul
2012.Jan
2012.Jul
2013.Jan
2013.Jul
2014.Jan
2014.Jul
2015.Jan
2015.Jul
2016.Jan
2016.Jul
2017.Jan
2017.Jul

(b)

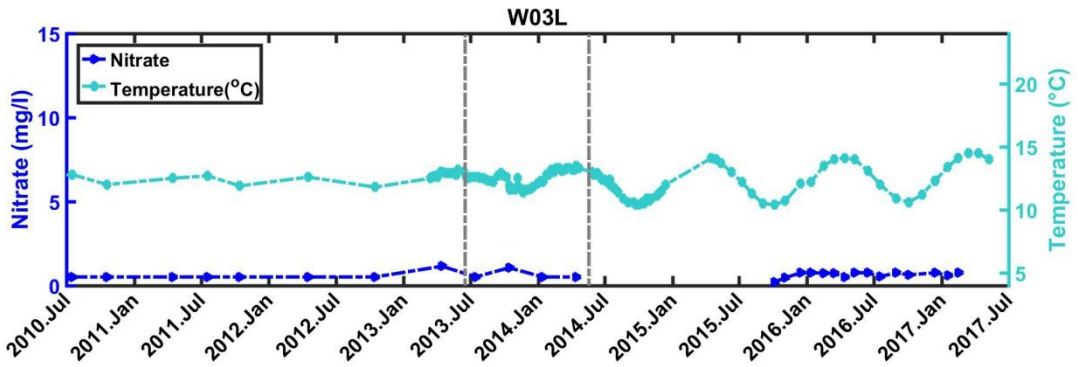
W03L
Nitrate
Temperature(°C)
Nitrate (mg/l)
Temperature (°C)
0
5
10
15
20
2010.Jul
2011.Jan
2011.Jul
2012.Jan
2012.Jul
2013.Jan
2013.Jul
2014.Jan
2014.Jul
2015.Jan
2015.Jul
2016.Jan
2016.Jul
2017.Jan
2017.Jul

(c)

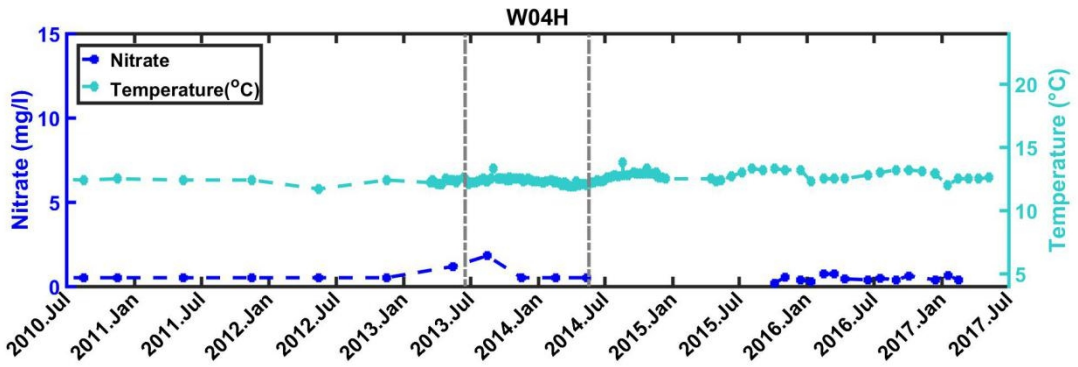
W04H
Nitrate
Temperature(°C)
Nitrate (mg/l)
Temperature (°C)
0
5
10
15
20
2010.Jul
2011.Jan
2011.Jul
2012.Jan
2012.Jul
2013.Jan
2013.Jul
2014.Jan
2014.Jul
2015.Jan
2015.Jul
2016.Jan
2016.Jul
2017.Jan
2017.Jul

(d)

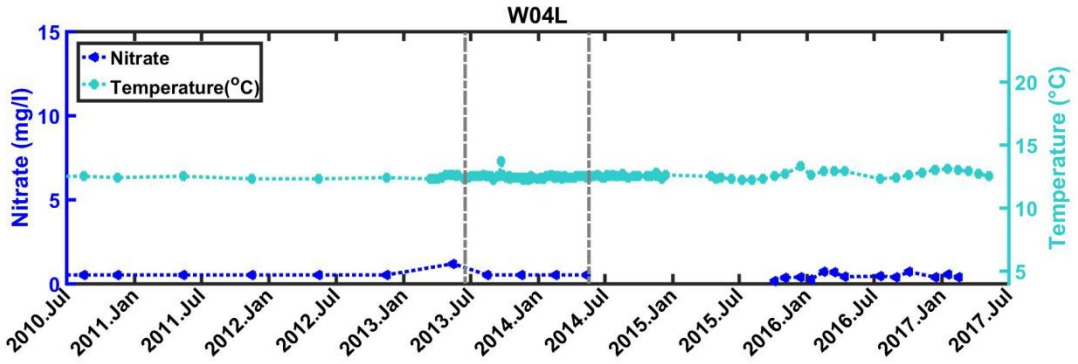

(e)

Fig. 3.10 The variation of nitrate (NO_3^-, mg/L) and temperature (°C) in the U100 (a) and observation wells $W03_{HIGH}$, $W03_{LOW}$ (b, c), $W04_{HIGH}$, $W04_{LOW}$ (d, e). Blue dots denote to NO_3^-; cyan dots denote to seasonal variations of temperature. The two grey dashed lines in June 2013 and May 2014 represent the period of reconstruction in the ND.

3.5.4 Ammonium

Increasing ammonium is one of the unwanted side effects in RBF caused by the changing redox condition (Hiscock and Grischek, 2002). Although the ammonium level is not included in the 'International Standards for Drinking-water' (World Health Organization (WHO), 2003), it still can influence the odor and the taste and further endanger the health inhigh doses. In Europe, the drinking water limit of ammonium is 0.5 mg/L (The Council of the European Union, 1998) both for the surface water and groundwater (The Council of the European Union, 2000). During the bank filtration process, the bioactivity of microbes is vital for the change of ammonium concentration (Groeschke et al., 2017), while the adsorption causes retardation for the ammonium transport in the aquifer. In the surface water at different bank filtration sites, the ammonium concentration varies from less than 1 mg/L (Ghodeif et al., 2018; Grischek et al., 1998; Gross-Wittke et al., 2010; Massmann et al., 2004) to several milligrams per liter (Doussan et al., 1998; Li et al., 2019; Wang et al., 2007) and even tens of milligrams per liter (e.g., Groeschke et al., 2017). The source could be either artificial, which is the treated or untreated wastewater and domestic sewage, or natural runoff which can include seasonal dynamics. During the bank filtration process, the change of the ammonium concentration is very much site-specific. Along with the flow, the increase of the ammonium concentration was concluded as mineralization (Doussan et al., 1998) or attributed to ammonification (Pan et al., 2018; Strock, 2008). This increase could happen either on the river bottom sediment or with a smaller extent along with the groundwater flow (De Vet et al., 2010), together with the accumulation in the aquifer (Kwon, 2015b). At an RBF site in Saxony, Germany, another source of ammonium was suggested as the sulfide-induced dissimilatory nitrate reduction (Grischek et al., 1998; Mallen et al., 1998), although other

DNRA processes have so far not yet been reported in bank filtration at this site. The decrease of ammonium concentration was mainly attributed to the nitrification (Doussan et al., 1998; Grischek et al., 1998; Pan et al., 2018; Wu et al., 2007). In the field studies, ammonium was also found in the newly infiltrated water (Grischek et al., 1998) to a distance of meters (Pan et al., 2018), tens of meters (Wu et al., 2007), and even hundreds of meters (Groeschke et al., 2017). Anaerobic ammonium oxidation to nitrogen (anammox) takes ammonium and nitrite as the redox partners (Van De Graaf et al., 1997), however, no research so far could distinguish it from nitrification during the bank filtration process which both act as a sink to the ammonium concentration. An oscillation of ammonimum concentration has also been observed within a site in different studies, (e.g. (Doussan et al., 1998; Groeschke et al., 2017; Pan et al., 2018)), while the level of change also varied a lot.

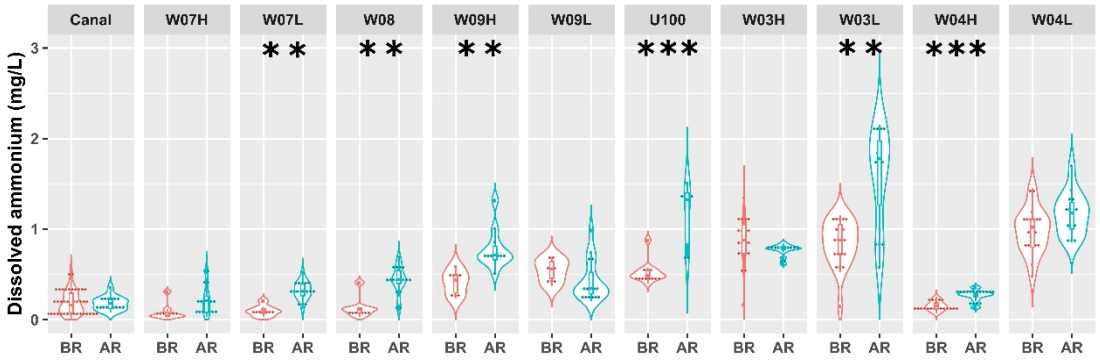

Fig. 3.11 Violin plot of the concentration distribution of ammonium (NH_4^+, mg/L) in the canal and observation wells before and after the reconstruction. '*' was used to denote the significance level (*represents P<0.01; **represents P<0.001; ***represents P<0.0001). Boxplots are included within the violin plot. The "BR" denotes to before reconstruction (from 2007 July to June 2013); "AR" denotes to after reconstruction (from June 2013 to February 2017).

In our study, as it was shown in Fig. 3.11 and Tab. 3.1, ammonium concentration in the canal was below 0.5 mg/L, and the change observed after the reconstruction was not significant (P>0.01). During the entire study period the ammonium concentration in groundwater was generally higher in wells of larger depth or further distance ($W04_{LOW}$, $W03_{LOW}$, U100) than the near-bank wells. The reason could be the mineralization along the flow path (De Vet et al., 2010), as it was described by the generalized reaction from Strock (2008). After reconstruction, higher median concentrations together with a broader variation range were observed (Fig. 3.11). Among the near-bank wells, $W09_{HIGH}$ showed the highest ammonium concentration level both before and after reconstruction. In comparison to $W09_{HIGH}$, the low ammonium level in $W07_{HIGH}$ can be due to the higher flow velocity ($WNA07_{HIGH}$) alleviated the mineralization of organic matter and further slowed down the increase of ammonium

concentration. This agrees with Doussan et al. (1997). Furthermore, as it was shown in chapter 3.5.1 and 3.5.2, both DO and nitrate were still present in $WNA07_{HIGH}$. This created the oxic environment along the flow path and decreased the ammonium concentration by nitrification.

Among deep wells, the ammonium concentration was kept at a similar level in $W04_{LOW}$ ($P>0.05$) after the reconstruction, while a significant change ($P<0.01$) could be observed in $W03_{LOW}$ and U100. The largest increase happened at $W03_{LOW}$. The median value jumped from less than 1 mg/L to around 2 mg/L. By plotting the ammonium concentration of the deep wells with time (Fig. 3.12) a general increase could be traced back to the last few samples during reconstruction. And further after the data gap, the ammonium level of $W03_{LOW}$ was maximum at the first sampling point (Oct 2015) and followed by a continuous decrease. No clear trend could be observed in the other two deep wells. Considering the relatively stable ammonium level during the six years' observation time since 2007, the substantial increase at $W03_{LOW}$ could have been triggered by the reconstruction. This could be either attributed to the increasing flow velocity along the flow path or the change of the hyporheic zone. However, the growing flow velocity is unlikely to be the cause since decreasing traveling time would limit the ammonification reaction (Doussan et al., 1998). Instead of the substantial increasing ammonium level, lower concentration should be expected. A similar conceptual model could be applied to the reconstructed riverbed, however, beyond the groundwater flow, the thermal field and the aquifer matrix in the hyporheic zone were also changed.

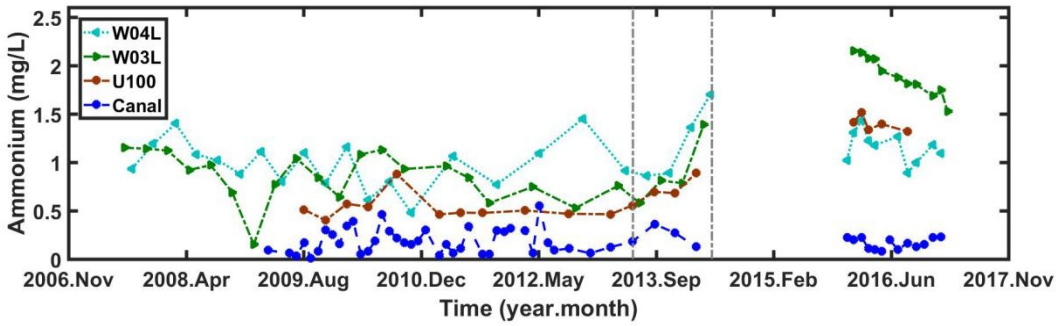

Fig. 3.12 Ammonium (NH_4^+, mg/L) concentration in the canal and deep observation wells before and after the reconstruction.

The hyporheic zone is decisive on ammonium concentration. As it was shown in the study of Doussan et al. (1998), the ammonium level rose from less than 5 mg/L to more than 200 mg/L at a depth of the 50 cm below the riverbed and was followed by a drastic decrease to less than 10 mg/L within few meters of distance by sorption (Doussan et al., 1998). A similar pattern also happened at an RBF site in Beijing, China, where the variation was within 2 mg/L (Pan

et al., 2018) and the decrease was caused by nitrification. Therefore, the hyporheic zone could act as both the source and sink for ammonium while the sorption could strongly postpone its propagation. The sorption capacity depends on the aquifer composition, where the decisive component is the negative charged clay and organic matter. As it was shown in multiple studies (McBratney et al., 2002; Seyed Jalali et al., 2019), the increasing mass fraction of clay and organic matter can raise the Cation Exchange Capacity (CEC). In this study, due to the reconstruction the original sedimentary layer and the clogged hyporheic zone were renewed by artificial material, where the sorption ability might have decreased until the external clogging layer was formed again and the pore space was refilled by the new sediment and the biofilm. During this period, the cation exchange capacity experienced a sudden drop followed by a slow recovery. Therefore, the much lower CEC level in the hyporheic zone was incapable of keeping the newly formed ammonium and further lead to its breakthrough along with the infiltration flow. As is shown in chapter 3.5.1 and 3.5.2, both the DO and nitrate were consumed in the deeper near-bank wells and therefore the sink of ammonium by nitrification and anammox could not happen.

If the ammonium rise was caused by the reconstruction, a key question to be answered is the lagged arrival time of the ammonium peak during its transport in groundwater. The main controlling factors on the retardation effect were both the cation exchange and biological reactions (Böhlke et al., 2006; Buss et al., 2004; Ceazan et al., 1989). In the field scale, the retardation of ammonium in the shallow aquifer was observed by in several studies (Böhlke et al., 2006; Ceazan et al., 1989; DeSimone and Howes, 1998) where the retardation factor varied from 2 to 6. However, Buss et al. (2004) demonstrated a broader variation range of ammonium retardation factor in their study which could reach as large as three orders of magnitude. In our site, the glacial tills with high silt composition was widely distributed. This can create areas of high CEC level and strongly delay the ammonium propagation. Therefore, a large retardation factor could be expected. Starting from the riverbed, the occurrence of the ammonium peak was supposed to occur during the reconstruction period. Estimated by Munz et al. (2019), the traveling time from the canal to $W03_{LOW}$ was 104 days and to $W04_{LOW}$ was 438 days. Therefore, if the ammonium peak (t_p) was observed at $W03_{LOW}$, the range of retardation factor could be simply achieved by the formula below:

$$r_{max} = (t_p - t_s)/104 \quad (7)$$

$$r_{min} = (t_p - t_e)/104 \quad (8)$$

where r_{max}, r_{min} are the maximum and minimum retardation factor. This reflects the two extreme cases: the peak of ammonium was released the first day and alternatively the last day

of the reconstruction period. The t_s, t_e stand for the starting and the completion time of the reconstruction.

However, due to the missing peak within the data gap between July 2014 to October 2015 in $W03_{LOW}$, it is impossible to make abovementioned calculation. Nonetheless, a parsimonious estimation could still be achieved based on the first traceable high value after the gap in $W03_{LOW}$. By using the first available data sample after the data gap and inserting it into formulas (7) and (8), the reconstruction period to the peaking time after the data gap was between 473 to 840 days ago. The retardation factor could be between 4.5 and 8.1. Further estimation on the peak arrival time for $W04_{LOW}$ would be between November 2018 and February 2024. However, since the actual peak in $W03_{LOW}$ should be within the sampling gap, the actual retardation factor should be smaller, which indicates an earlier arrival time of ammonium peak for $W04_{LOW}$. Nonetheless, due to the long traveling distance, the peak can be strongly alleviated by the dispersion and diluted by the coming groundwater of lower ammonium concentration. Therefore, it might not be able to be directly observed.

In general, after reconstruction, the ammonium level increased in all wells, except at $W03_{HIGH}$. Shown by the high ammonium concentration at $W03_{LOW}$, a possible breakthrough might have happened due to the sudden drop of CEC in the renewed riverbed. A rough estimation of the retardation factor for ammonium based on the available data can be estimated within the range of 4.5 and 8.1. The ammonium peak would arrive at $W04_{LOW}$ no later than February 2024. However, due to the strong connection between the retardation factor and the aquifer matrix, the arrival time of the peak might deviate from the estimated date. Nonetheless, because of the long setback distance, the ammonium peak can be further alleviated and diluted and even vanish at the distant well.

3.5.5 Manganese and iron

Manganese and iron are electron acceptors after the depletion of oxygen and nitrate in a closed groundwater system (Champ et al., 1979; Chapelle, 2001). They are reduced and dissolved into pore water from the solid phase. Both their dissolution and sequestration have a causal relationship of redox change along with groundwater flow (Farnsworth and Hering, 2011). The dissolution of manganese and iron mainly happens at three conditions (Kedziorek et al., 2008): 1) heavier organic load in the infiltrating water; 2) dammed river with increasing DO consumption in sediment or during the flow path, and 3) a less permeable layer covers the top of the aquifer. It could also be concluded as a condition when the electron donors are overwhelmed. Based on previous studies, Oren et al. (2007) summarized that Mn dissolution started when the DO concentration became smaller than 50 $\mu mol.L^{-1}$. Kedziorek and Bourg (2009) demonstrated that the reduction and dissolution of manganese and iron would happen

when the index of ETC (Electron trapping capacity) was smaller than 0.2mmol L^{-1}. Variation of manganese and iron concentration was found in different investigations. For meters to ten meters of traveling distance, Bourg and Bertin (1993) found that the manganese concentration increased during the infiltration and then decreased afterward, likely due to the solubilization during infiltration and subsequent sorption of oxidized Mn along the further flow path. For longer traveling distances (hundreds of meters), a study in Delhi, India, at an highly polluted water course (Groeschke et al., 2017) showed an initial increasing trend and then decreased concentration along the flow path for both iron and manganese. However, a study in Reijerwaard, Netherlands (De Vet et al., 2010) showed an increasing iron but decreasing manganese concentration along the groundwater flow path. Both studies have in common that iron concentration was higher than manganese concentration by even one order of magnitude larger in some wells. Investigations among three RBF sites of similar scales in the US also showed the increase of manganese concentration of different extent (Hoppe-Jones et al., 2010). Within one site, the Mn concentration can also show great heterogeneity. Such as the case of the Soil Aquifer Treatment in Shalfdan, Israel, and the reason was assumed to be the heterogeneity in aquifers, including the variation of rock type, velocity, redox process and bearing of Mn in the rock (Oren et al., 2007).

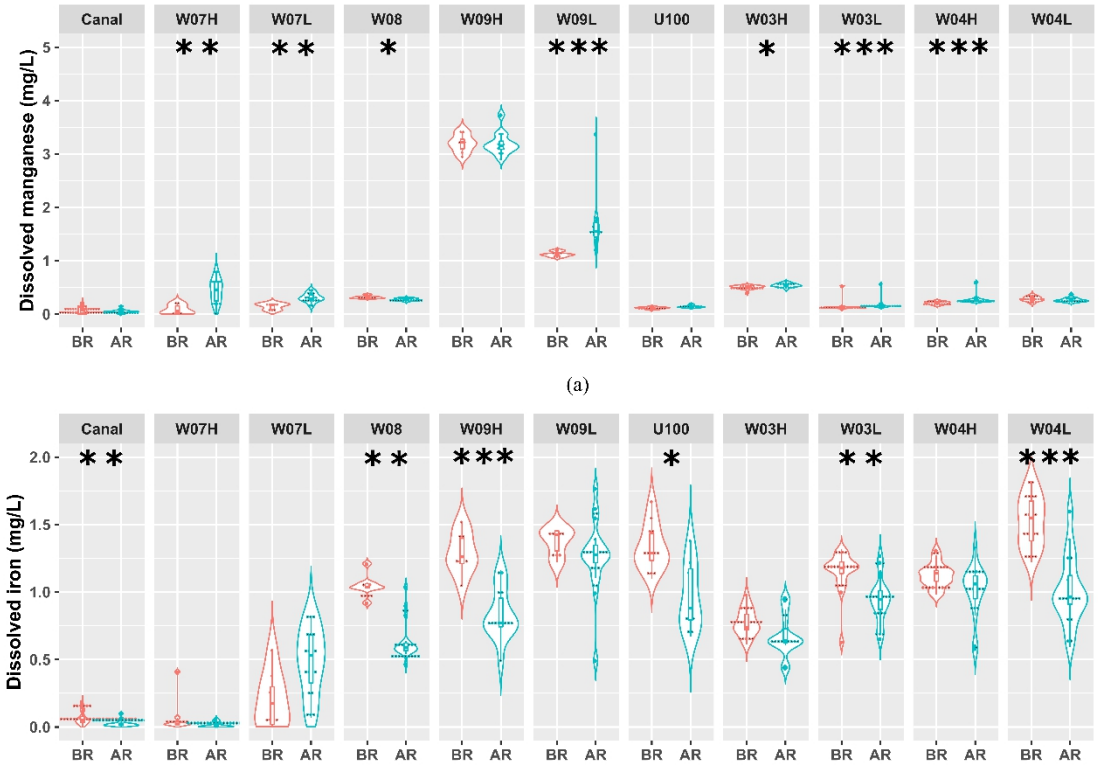

Fig. 3.13 Violin plots of the variation of manganese (Mn^{2+}, mg/L) (a) and iron (Fe^{2+}, mg/L) (b) in the river and observation wells. The '*' was used to denote the significance level (*represents P<0.01; **represents P<0.001; ***represents P<0.0001). Boxplots are included within the violin plot. The

"BR" denotes to before reconstruction (from 2007 July to June 2013); "AR" denotes to after reconstruction (from June 2013 to February 2017).

When having a low concentration in the canal water, higher manganese and iron concentrations must be biogenic or geogenic origin on the flow path, starting while the SW is infiltrating into the riverbed. Generally, the manganese concentration was very low in all the observation wells, except W09. After the reconstruction, a significant change ($P<0.01$) could be found in most wells except $W09_{HIGH,}$ $W04_{LOW}$ and U100 and the canal. In near-bank wells, the increase of the median Mn^{2+} concentration was found in $W07_{HIGH}$ (from 0.05 mg/L to 0.46 mg/L), $W07_{LOW}$ (from 0.18 mg/L to 0.29 mg/L), and $W09_{LOW}$ (from 1.12 mg/L to 1.55 mg/L) (Fig. 3.13a, Tab. 3.2). Further along the flow path, the Mn^{2+} concentration was significantly different after the reconstruction ($P<0.01$) in the distant wells, except $W04_{LOW}$. However, due to the relatively low concentration (mostly below 0.1 mg/L, except $W07_{HIGH}$, $W07_{LOW}$ and $W09_{LOW}$), the absolute change was also small. The general low concentration in distant wells might partly reflect the dilution effect by the mixing of infiltrating water through different flow paths. Due to the low contributing rate from the relatively stagnant flow passing by W09, the much larger flowrate of low-Mn^{2+}-concentration water infiltrating from other flow paths can keep the mixed water from substantial Mn^{2+} increase. Fe^{2+} concentration was generally higher than Mn^{2+} (Fig. 3.13b) in most of the wells. A clear spatial trend was observed among the near-bank wells, which followed an order of $W07_{HIGH}<W07_{LOW}<W08<W09_{HIGH}<W09_{LOW}$ (Fig. 3.13b) both before and after the reconstruction. This was in accordance with the increasing order of the residence time, based on the calculation from Munz et al. (2019), except for the two wells of W09. The lowest concentration was at well $W07_{HIGH}$, which was close to zero as in the canal, while the largest was at $W09_{LOW}$ (1.43 mg/L before- and 1.27 mg/L after reconstruction). For distant wells, the strength of the reducing environment increased along with distance and depth from infiltration, peaked at $W04_{LOW}$, where the median Fe^{2+} concentration was 1.55 mg/L before- and 1.31 mg/L after reconstruction. Containing the remnant landside groundwater, U100 kept a similar median level and variation range of Fe^{2+} as $W04_{LOW}$ (Fig. 3.13b).

Different from DO and nitrate, which were almost fully consumed in most of the observation wells, both the dynamic of the Fe^{2+} and Mn^{2+} can reflect the change of the redox condition in those wells. For iron, after reconstruction, a significant change ($P <0.01$) could be observed in most of the wells, except for $W07_{HIGH}$, $W07_{LOW}$, $W03_{HIGH}$ and $W04_{HIGH}$. However, if the threshold of the P-value was chosen as 0.05, the distant wells of $W03_{HIGH}$ and $W04_{HIGH}$ would also be considered as experiencing a significant change after the reconstruction. As it is shown in Tab. 3.2, except $W07_{LOW}$, all the wells showed the decrease of the median Fe^{2+} concentration level. This hinted that along those flow paths less iron was dissolved from the

solid phase into the groundwater and correspondingly less dissolved organic matter was oxidized. However, considering the significant Mn^{2+} increase in some of the wells ($W03_{LOW}$, $W03_{HIGH}$, $W04_{HIGH}$ and $W09_{LOW}$), contradictory conclusion might be drawn. Although the increase of median level was mostly smaller than 0.05 mg/L in most of the wells, it still created an ambiguity for explaining the local redox change. Nonetheless, since the change both for Fe(II) and Mn(II) was within 0.5 mg/L, and considering the reaction ratio with the organic matter, the possible change for DOC would be very small (within 0.25 mg/L), which might not be of great influence in this RBF field.

According to the order of electron acceptors, the dissolution of manganese should be ahead of iron in the redox reaction, while in this study, the Fe^{2+} concentration was generally much higher than Mn^{2+} (Fig. 3.13). Similar cases were also observed in other studies (De Vet et al., 2010; M. Groeschke et al., 2017). To clarify the reason, ETC value (Kedziorek and Bourg, 2009) was adopted for examining the redox condition. Except for $W07_{HIGH}$, all the other wells exhibited ETC values below the threshold for manganese and iron dissolution (0.1 millimol/L) (Fig. 3.14). This suggested that both Fe(II) and Mn(II) could be released along the flow path before reaching those observation wells, while the general low Mn^{2+} concentration could be ascribed to a general scarcity of manganese in the aquifer. Manganese-rich material may exist between the canal and W09. Superposed by the stagnant groundwater flow along the flow path, more Mn^{2+} might be released before reaching $W09_{HIGH}$ and $W09_{LOW}$. With a higher weight of 'remnant landside groundwater', water samples in U100 also showed a general low background Mn^{2+} concentration in the aquifer. A great variation range of ETC level in $W07_{HIGH}$ could be observed, while the release of Fe^{2+} and Mn^{2+} was always low regardless of the seasonal dynamic. This indicates the limitation of ETC on forecasting the case with great seasonal dynamic on redox condition especially for high DO residues in the winter time like $W07_{HIGH}$.

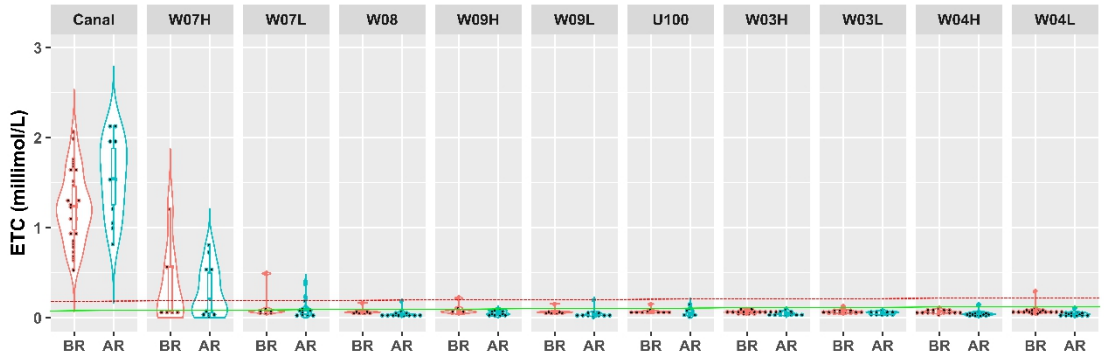

Fig. 3.14 Violin plot of the electron trapping capacity (ETC) values (millimol/l) in wells during the monitoring period (from 9/15/2010 to 12/14/2016). The red line denotes the threshold for reductive dissolution of manganese and iron oxyhydroxides occurrence when ETC value lower than 0.2 mmol/L,

and the green line denotes the threshold for iron dissolution when ETC value lower than 0.1 mmol/L. The abovementioned standard is according to Kedziorek and Bourg (2009) The "BR" denotes to before reconstruction (from 2007 July to June 2013); "AR" denotes to after reconstruction (from June 2013 to February 2).

3.5.6 Sulfate

Sulfate is the electron acceptor after manganese and iron oxides or hydroxides are reduced (Su et al., 2018). By the joint effort of the difference in the quantity of organic carbon and previous electron acceptors, further influenced by temperature variation and geological composition, sulfate might show either conservative (Bourg and Bertin, 1993; Oren et al., 2007) or variation (Grischek et al., 1998; M. Groeschke et al., 2017; Massmann et al., 2003b; Su et al., 2018) in the near bank site. Sulfate could be increased by oxidation of pyrite (e.g., Massmann et al., 2003) or consumed as the electron acceptor.

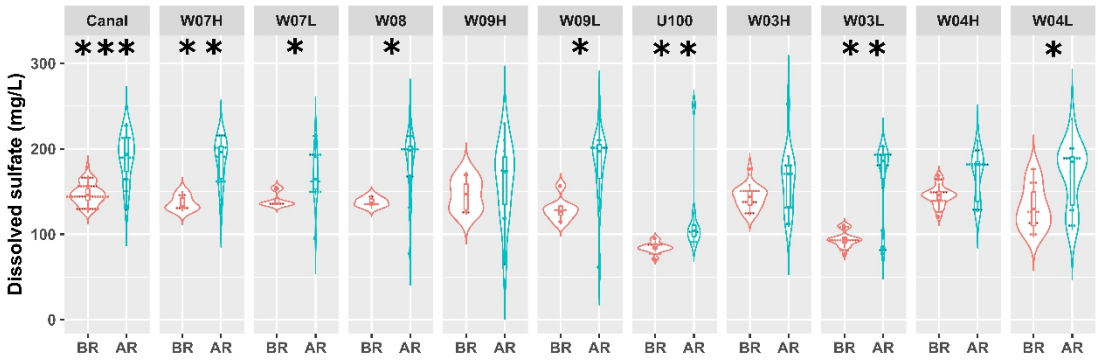

Fig. 3.15 Violin plot of the variation of sulfate (SO_4^{2-}, mg/L) in the canal and observation wells. The '*' was used to denote the significance level (*represents P<0.01; **represents P<0.001; ***represents P<0.0001). Boxplots are included within the violin plot. The "BR" denotes to before reconstruction (from 2007 July to June 2013); "AR" denotes to after reconstruction (from June 2013 to February 2017).

Before the reconstruction (Fig. 3.15) the SO_4^{2-} concentration of the near-bank wells had a similar level as the SW. Even when wells had reached an anaerobic stage, such as $W09_{HIGH}$, $W09_{LOW}$ and W08, there was no noticeable decrease of SO_4^{2-} compared with the SW. As it was shown in the study of Massmann et al. (2003b), even with relative stable SO_4^{2-} concentration, the change of the SO_4^{2-} isotopic signature could still hint at the occurrence of the SO_4^{2-} reduction, however, the data were not available here. Therefore, no definite conclusion could be drawn. For the deep and distant wells, a lower sulfate level could be observed in U100 and $W03_{LOW}$ (Fig. 3.15). In another distant well $W04_{LOW}$, the median level was like the near-bank wells, however, with broader variation range to lower concentration. As it was mentioned before, this could be a mixture of both deep aquifer flow and infiltrated

SW from the near-bank wells and the sulfate level might vary in between. After the reconstruction, the most substantial SO_4^{2-} change ($P<0.0001$) was in the SW, where the median level increased drastically (146 mg/L to 194 mg/L). This was not due to the reconstruction. The change in the SW was rather a coincidence however the direct cause was not clear. A global response on the increase of median SO_4^{2-} concentration and broader variation range could be observed, significant in most wells ($P<0.01$) except for U100, $W03_{HIGH}$ and $W04_{HIGH}$. Among them, U100 kept the lowest concentration after the reconstruction (Fig. 3.15). Except for its highest value, which likely is due to measurement error, U100 also showed the smallest variation range. The largest increase of median value happened at the distant well of $W03_{LOW}$ ($P<0.001$), where it doubled. The median value increased from a level similar to U100 to the level of near-bank wells. For $W04_{LOW}$, significant change ($P<0.001$) was also observed, where the median level reached as high as $W03_{LOW}$ after reconstruction. This result was in accordance with the conclusion from the piper plot, which could be explained as the higher infiltration rate of the canal water shifting the deep aquifer flow from the remnant landside groundwater dominant (similar as U100) to the newly infiltrated canal water dominant. It also suggested the possibility of using sulfate as a tracer for further study in this site.

3.5.7 DOC

The median DOC concentration in all observation wells was generally lower than SW during the whole monitoring period (Fig. 3.16). After the reconstruction, there was a significant ($P<0.0001$) change of the DOC concentration in the canal, where the median concentration level decreased from 8.9 mg/L to 7.6 mg/L (Fig. 3.16). Representative of containing the remnant landside groundwater, U100 showed the lowest DOC level as well as the minimum variation range both before and after the reconstruction. This indicated a relatively stable and low DOC background at the starting point of the deep flow path. In the near-bank wells the variation range of DOC grew after the reconstruction. The high level (5.90-9.00 mg/L) was mainly measured in November and December of 2013. when the construction was ongoing. The low concentration level (1.72-3.62 mg/L) was mostly measured among the period between April 2016 and November 2016. In distant wells, the further enlargement of the DOC variation range as the near-bank wells was not observed (Fig. 3.16). The deep well of $W03_{LOW}$ showed a similar low median DOC level as U100. However, it increased slightly after the reconstruction. This could be attributed to the rising share of high DOC level SW in the deep flow path caused by the reconstruction. $W04_{LOW}$ was the closest observation point to the water supply network and showed a higher median value than $W03_{LOW}$, but a much narrower DOC variation range. This demonstrated that with current setback distance, the RBF

site could not only reduce the high and variable DOC level of the SW into a stable and relative low-level range, but also buffer the influence of the reconstruction. However, compared to the near-bank wells, there was no observed further decrease in the DOC median level in the more distant wells (Fig. 3.16). This illustrates that the majority of the DOC consumption happened before reaching the near-bank wells.

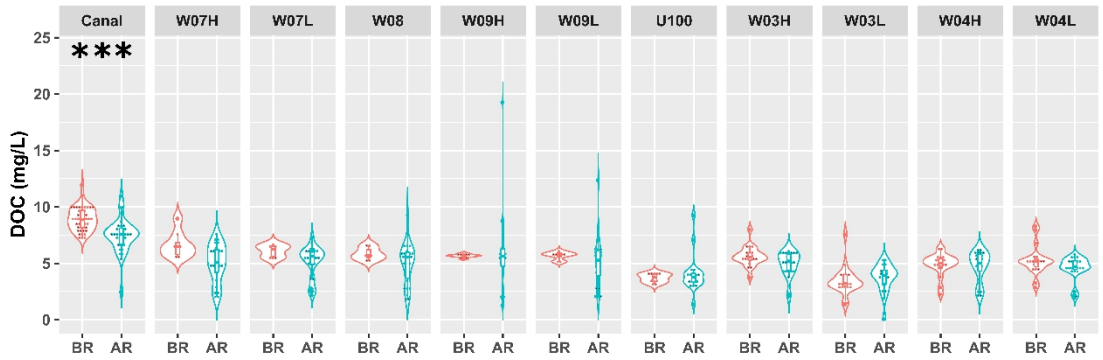

Fig. 3.16 Violin plots of the variation of dissolved organic carbon (DOC, mg/L) in the river and observation wells. '*' was used to denote the significance level (***represents P<0.0001). Boxplots are included within the violin plot. The "BR" denotes to before reconstruction (from 2007 July to June 2013); "AR" denotes to after reconstruction (from June 2013 to February 2).

The measurement of DOC was a direct indicator of the RBF treatment effect. However, since POC also contributed as an electron donor in the redox reactions, it was necessary to check the total consumption rate of the organic matter during the bank filtration. A previous investigation by Kedziorek et al. (2008) recovered the quantity of the reacted organic carbon by DO and nitrate consumption and further distinguished the fraction between the DOC and POC in the cold and warm time. In our study, we used a continuous measurement between November 2015 and December 2016. Shown in Tab. 1.1, the consumed CH_2O was estimated based on the relationship of the difference of DO and the nitrate concentration between the canal and the near-bank well. Two assumptions were made to simplify the comparison: 1) the traveling time of the infiltrated water reaching the near-bank wells was ignored since the sampling time step gap was more than one month, which could be longer than the traveling time, and 2) all the organic carbon was consumed by the redox reaction mediated by microorganisms (as mentioned by Grischek et al. (1998)). The total involved CH_2O (t- CH_2O) was used, which was defined as the sum-up of consumed CH_2O and the measured CH_2O (converted from DOC) in the observation wells. Shown in Fig.3.17, the median t-CH_2O level in the observation wells was above the maximum CH_2O level in the canal, except for the W08. Furthermore, half of the interquartile range for all observation wells was located outside of the maximum CH_2O in the canal. This indicated the involvement of POM as the additional

carbon source for the redox reaction which was consistent with the previous studies, e.g., (Grünheid et al., 2005; Hoppe-Jones et al., 2010; Romero-Esquivel et al., 2017).

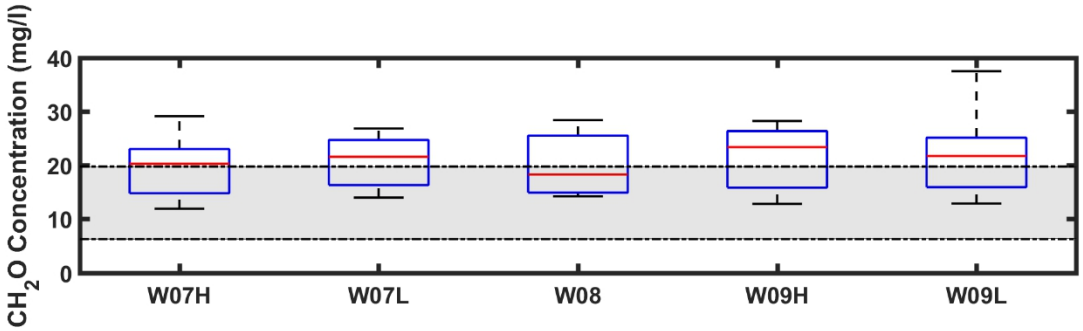

Figure. 3.17 The total involved CH_2O (t-CH_2O) for the near-bank wells after the reconstruction. The grey zone stands for measured CH_2O concentration range in the canal, which was converted from DOC. The box-plot of the observation wells stands for the sum of CH_2O consumed (inferred from the decrease of DO and nitrate concentration and the increase of Mn^{2+} and Fe^{2+} concentration) and the measured CH_2O (converted from measured DOC).

3.5.8 SUVA

Specific ultraviolet absorbance (SUVA) has been widely adopted as a surrogate for forecasting the formation potential of disinfection by-products (DBPs) (Hua et al., 2015; Singer, 1999). Typically, the SUVA value above 4 L/(mg·m) would be considered as a sign of high weight on the aromatic hydrophobic matters. This leads to a higher potential of DBPs formation. SUVA values smaller than 2 L/(mg·m) indicate a higher fraction of aliphatic organic substances, which has a low risk of DBPs formation. A middle value is considered as a medium level, which is a mixture of both. Although in the waterworks at our study site, there is no further disinfection process involved in, it could still be a hint for other RBF sites that may face the risk of DBPs. The data in our study was available only before and shortly after the reconstruction. Shown in Fig. 3.18, the SUVA value in the canal was around 2 L/(mg·m), both before and after the reconstruction. No clear relationship could be concluded between the SUVA and the DOC. In the near-bank wells W07, W08 and W09, the SUVA value was kept around 2 L/(mg·m) along the whole sampling period, which was similar to the SUVA level in the canal. Even when the sampled DOC value reached above 8 mg/L, the SUVA level was still consistent, which indicated that there was no apparent preference in the DOC degradation along the flow path to the near-bank wells regardless of the DOC treatment efficiency. Among the distant and deep wells, U100 showed a relatively lower SUVA level and the smallest variation range. No noticeable change could be observed after the reconstruction. This suggested a relatively stable condition of the remnant groundwater during the whole sampling period. In the distant wells W03 and W04, SUVA values higher

than 4 L/(mg·m) were observed in Feb 2008 and Feb 2009 when the corresponding DOC level was also the lowest among the observation results. This suggested a further depletion of aliphatic matter after passing the oxic zone, which drove the DOC down but increased the weight of aromatic matter. A similar case was observed at an RBF site in Aurora, Colorado, USA (Regnery et al., 2015), where the SUVA value increased along with the drop of DOC in four years of observation. After reconstruction, all the measurements in distant wells were approximately 2 L/(mg·m). This indicated relatively low risk on the DBPs formation.

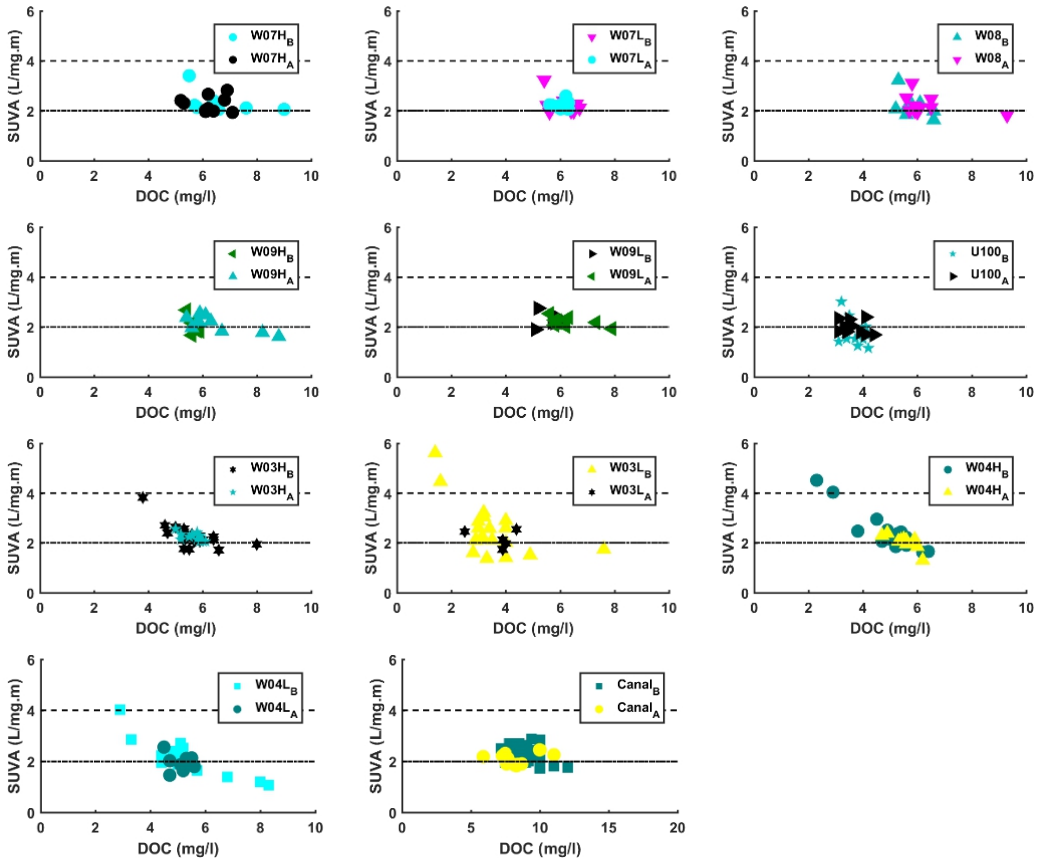

Figure 3.18 SUVA value in the canal and observation wells both before and after the reconstruction. The subscript of 'B' stands for the observation before the starting of the reconstruction while 'A' stands for the observation after it.

Chapter 4 Result of Groundwater Flow and Heat Modelling

The analysis of the water quality data described influence brought by the reconstruction both in the short term and one year after the complement of the project. However, as a technique for water treatment, not only the quality but also the quantity should be considered. The increasing hydraulic connection between the canal and the aquifer could bring a larger infiltration rate into the aquifer. The modelling research could give a reasonable estimation of this change. This chapter is adopted from the published article in Hydrogeology Journal named 'Impact of river reconstruction on groundwater flow during bank filtration assessed by transient three-dimensional modelling of flow and heat transport' by Wang et al. (2020), which can be accessed online as https://doi.org/10.1007/s10040-019-02063-3.

4.1 Groundwater Flow Model

4.1.1 Results of the steady-state flow modelling

The scatter plot of water heads between observation and simulation after model calibration is shown in Figure 4.1. The evaluation of the goodness of fit for the steady-state model showed good agreement between observed and simulated values (groups (i) and (ii)), with a Mean Absolute Error (MAE) of 0.71 m and a Root Mean Square Error (RMSE) of 1.04 m (Fig. 4.1a). Observed water heads lower than 25 m a.s.l. are mainly from the observation points of the pumping wells (green points in Fig. 2.3). A systematic deviation was observed in this region, which was to be expected when applying a steady-state model while pumping was varying on a day-by-day basis. Points with high water heads were mainly located in the southeast and southwest of the model, where a more considerable degree of uncertainty exists in the geological conditions, and thus also in the simulated heads, due to sparser drilling information. Generally, the geological condition at the study site is known to be discontinuous and heterogeneous, because of the unconsolidated composition of the Quaternary deposits that have likely been modified by erosion or formed naturally by depositional fluvial system dynamics.

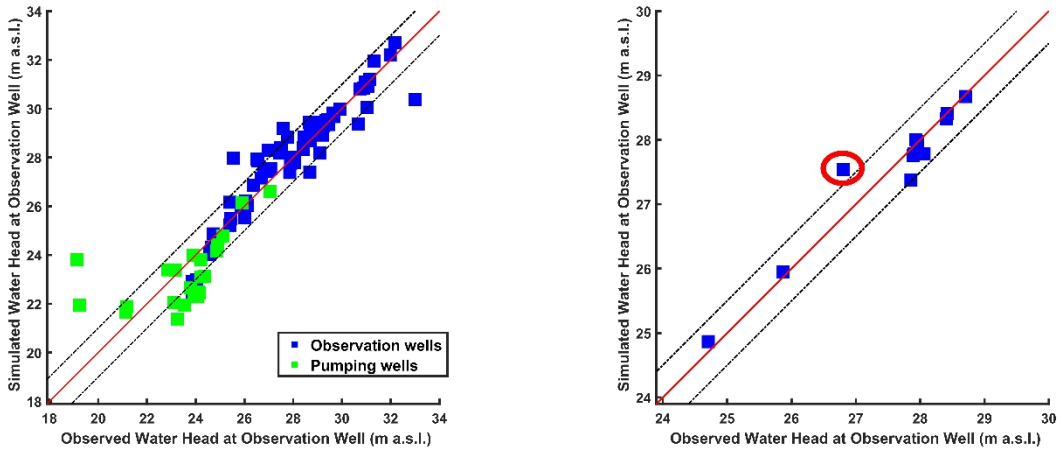

Fig. 4.1 Scatter plot of observed versus calculated water heads of the calibrated steady state model of all available observation wells and b only the observation wells between the canal and pumping wells. The black dashed lines represent the interval of a ±1-m and b ±0.5-m deviation from the perfect match (red diagonal line). The red circle (b) highlights the position of well $W03_{HIGH}$, which shows the largest deviation

For the observation points between the ND and pumping well gallery, the deviation between observed and simulated water heads (group (ii) only) was even smaller, with an MAE of 0.18 m and RMSE of 0.28 m (Fig.4.1 b). Almost all the points are located within the interval of ± 0.5 m, except for $W03_{HIGH}$ (absolute error of 0.7 m, highlighted by the red circle in Fig. 4.1b). Generally, the model did show a good overall fit and can be assumed to represent the complex hydraulic conditions at the study site moderately well. The hydraulic conductivity for sand was largest at the bottom aquifer, with a value of 3.5×10^{-4} m/s for the horizontal and the K_h/K_v of 8.3, respectively. The hydraulic conductivity of the remaining aquifers ranged from 2.9×10^{-5} to 1.0×10^{-4} m/s in the horizontal direction and from 5.1×10^{-6} to 4.2×10^{-5} m/s in the vertical direction. The K_h of the aquitards (glacial tills and silt) was much lower, varying between 2.0×10^{-7} m/s and 2.0×10^{-6} m/s. Details of the calibrated hydraulic conductivities can be found in Tab. 4.1. The large anisotropy ratio of SI-GT was set to fit the hydraulic heads in the southern part of the model domain, which was otherwise underestimated. The same result could have been achieved by a lower horizontal hydraulic conductivity, but that would also influence the hydraulic conductivities in the near-shore area. Therefore, the large anisotropy ratios of SI-GT mimic the impermeable second aquifer bottom without affecting the calibration results of the first aquifer. The parameter sets achieved were further used for the transient model, as described further below.

Table 4.1. List of calibrated hydraulic conductivities for the steady-state and transient models (WI refers to Weichselian, S to Saalian and GT to glacial till).

Name	Steady-state model		Transient model	
	K_x, K_y (m/s)	K_z (m/s)	K_x, K_y (m/s)	K_z (m/s)
Sand layers on the top	8.0E-05	1.1E-05	8.0E-05	1.1E-05
Sand zone of WI-GT layers	1.0E-04	1.0E-05	1.0E-04	1.0E-05
Sand layers between WI-GT and SII-GT	5.6E-05	2.0E-05	8.1E-05	3.5E-05
Sand zone of SII-GT layers	8.4E-05	1.5E-05	8.4E-05	1.5E-05
Sand layers between SII-GT and SI-GT	2.9E-05	5.1E-06	1.9E-04	3.5E-05
Sand zone of SI-GT layers	3.5E-04	4.2E-05	1.2E-04	5.8E-05
Sapropel of Lake "Weisser See"	8.9E-06	3.1E-06	8.9E-06	3.1E-06
Sapropel of Lake "Jungfernsee"	1.3E-05	1.5E-06	1.3E-05	1.5E-06
WI-GT lens	4.4E-07	1.5E-07	2.0E-06	2.0E-07
WI-GT	1.1E-06	1.3E-07	1.1E-06	1.3E-07
Silty sand lens	1.1E-06	1.2E-07	1.1E-06	1.2E-07
SII-GT	2.0E-06	7.9E-07	2.0E-06	7.9E-07
SI-GT	2.0E-07	8.8E-10	1.2E-06	1.2E-07

4.1.2 Results of the transient flow modelling

Hydraulic conductivities resulting from manual re-calibration in the transient model are listed in Table 4.1. Compared with the steady-state model, the changes resulted were mainly for the aquifers as well as the SI-GT and WI-GT lenses, as they were highlighted in grey. Both horizontal and vertical hydraulic conductivities were increased in the SI-GT and WI-GT lenses but decreased in the bottom aquifer. The modifications further oriented the model towards the observation points with frequent measurements that were in the core area of interest. A transient model based on such a substantial time series of observations, implying a strong top-up of experimental information on the groundwater flow system, can be expected to be a better representation of reality than the inherently more simplified steady-state model. However, it is also a much higher computational burden.

The model results are grouped into ‘before’ and ‘after’ the start of the reconstruction period and evaluated by both Pearson’s correlation coefficient (*r*) and RMSE (Table 4.2). The resulting time series are shown in Fig. 4.2, 4.3 and 4.4. The RMSE before reconstruction ranged between 0.09 m and 0.33 m, with an average value of 0.24 m, while after the reconstruction, the scenario of with reconstruction showed a lower average RMSE (0.32m) than the scenario of without the reconstruction (RMSE=0.56m). By including the reconstruction into the model, the increasing groundwater head was captured at all observation points. The theory behind could be explained as below. During the riverbed

reconstruction, low-permeability riverbed sediments (including parts of the glacial tills) were dredged out, while the bank reconstruction led to the removal of lateral hydraulic resistances. This increased the hydraulic connection between the canal and the aquifer. To maintain the consistent pumping rates after the reconstruction, a lower hydraulic gradient between the canal and pumping wells was sufficient due to the increased hydraulic connection. Therefore, the water heads in the pumping wells increased as well as in the area between the canal and the waterworks. Nevertheless, the RMSE on average increased for the period of reconstruction. This reflects that the system change is less well represented than the stable period previously, which could be attributed to fact that the real local changes in the riverbed were not known and that this period was a forward prediction and not subject to re-calibration.

Table 4.2. The transient flow model results for the scenario with reconstruction and without the reconstruction, evaluated by Pearson's correlation coefficient and RMSE.

	Pearson's correlation coefficient			RMSE (meter)		
		After Starting Reconstruction		Before Reconstruction	After start of reconstruction	
Observation well	Before Reconstruction	Including Reconstruction	Without Reconstruction		Including Reconstruction	Without Reconstruction
W06	0.9	0.87	0.9	0.09	0.14	0.19
W05	0.92	0.13	0.09	0.14	0.30	0.36
$W04_{LOW}$	0.59	0.93	0.93	0.31	0.43	0.77
$W03_{LOW}$	0.18	0.71	0.48	0.33	0.43	1.01
$W07_{LOW}$	0.15	0.26	0.53	0.23	0.34	0.47
W08	0.83	0.62	0.28	0.19	0.16	0.87
$W09_{LOW}$	0.85	0.72	0.34	0.10	0.15	0.60
U100	0.77	0.76	0.31	0.13	0.09	0.49
$W04_{HIGH}$	0.71	0.9	0.9	0.15	0.18	0.54
$W03_{HIGH}$	0.58	0.69	0.8	0.83	0.96	0.34
$W07_{HIGH}$	0.28	0.35	0.62	0.25	0.35	0.45
$W09_{HIGH}$	0.84	0.7	0.35	0.09	0.18	0.60

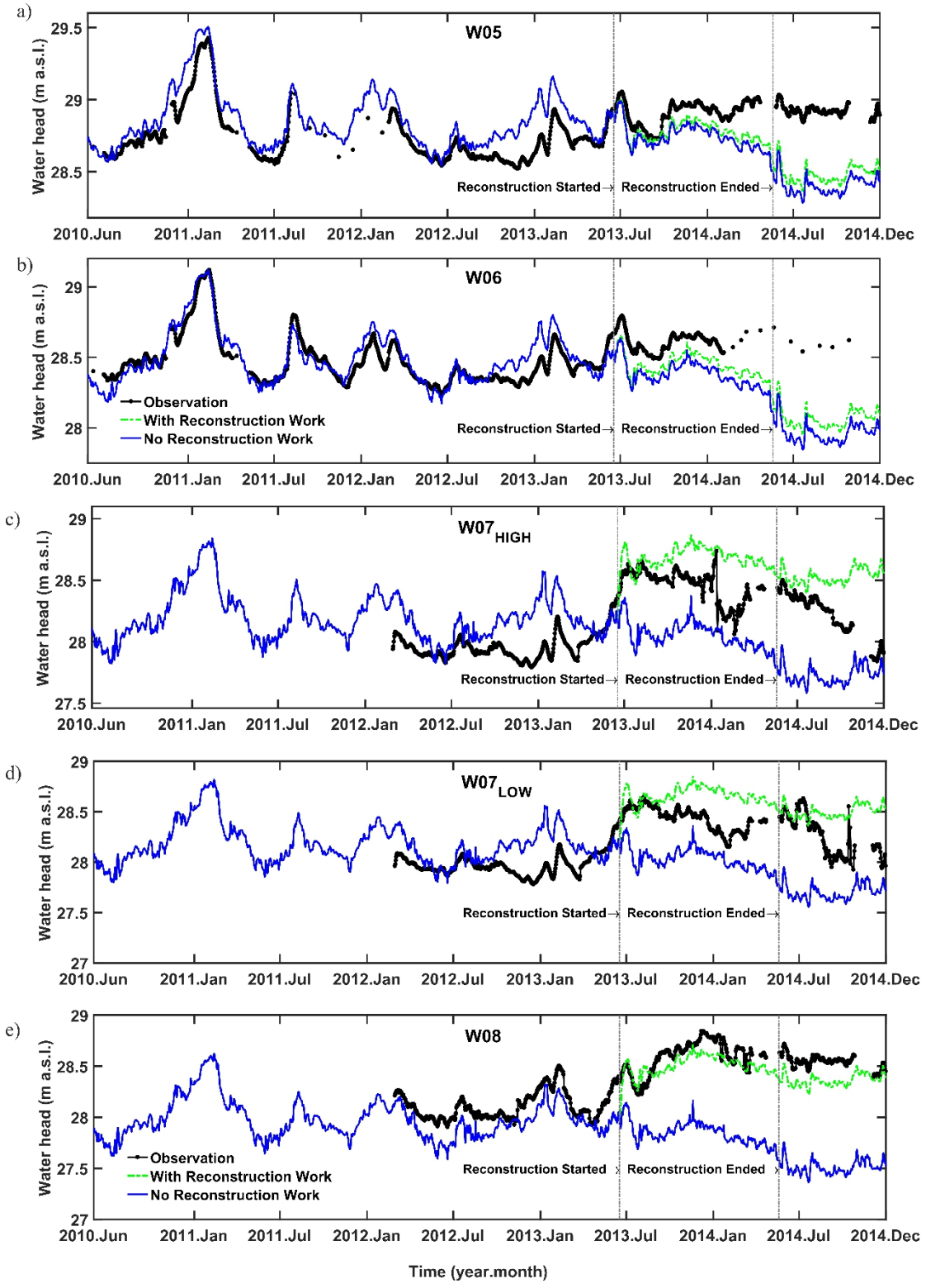
a)
W05
Water head (m a.s.l.)
29.5
29
28.5
Reconstruction Started
Reconstruction Ended
2010.Jun
2011.Jan
2011.Jul
2012.Jan
2012.Jul
2013.Jan
2013.Jul
2014.Jan
2014.Jul
2014.Dec
b)
W06
Water head (m a.s.l.)
29
28.5
28
Observation
With Reconstruction Work
No Reconstruction Work
Reconstruction Started
Reconstruction Ended
2010.Jun
2011.Jan
2011.Jul
2012.Jan
2012.Jul
2013.Jan
2013.Jul
2014.Jan
2014.Jul
2014.Dec
c)
W07HIGH
Water head (m a.s.l.)
29
28.5
28
27.5
Reconstruction Started
Reconstruction Ended
2010.Jun
2011.Jan
2011.Jul
2012.Jan
2012.Jul
2013.Jan
2013.Jul
2014.Jan
2014.Jul
2014.Dec
d)
W07LOW
Water head (m a.s.l.)
29
28.5
28
27.5
27
Reconstruction Started
Reconstruction Ended
2010.Jun
2011.Jan
2011.Jul
2012.Jan
2012.Jul
2013.Jan
2013.Jul
2014.Jan
2014.Jul
2014.Dec
e)
W08
Water head (m a.s.l.)
29
28.5
28
27.5
27
Observation
With Reconstruction Work
No Reconstruction Work
Reconstruction Started
Reconstruction Ended
2010.Jun
2011.Jan
2011.Jul
2012.Jan
2012.Jul
2013.Jan
2013.Jul
2014.Jan
2014.Jul
2014.Dec
Time (year.month)

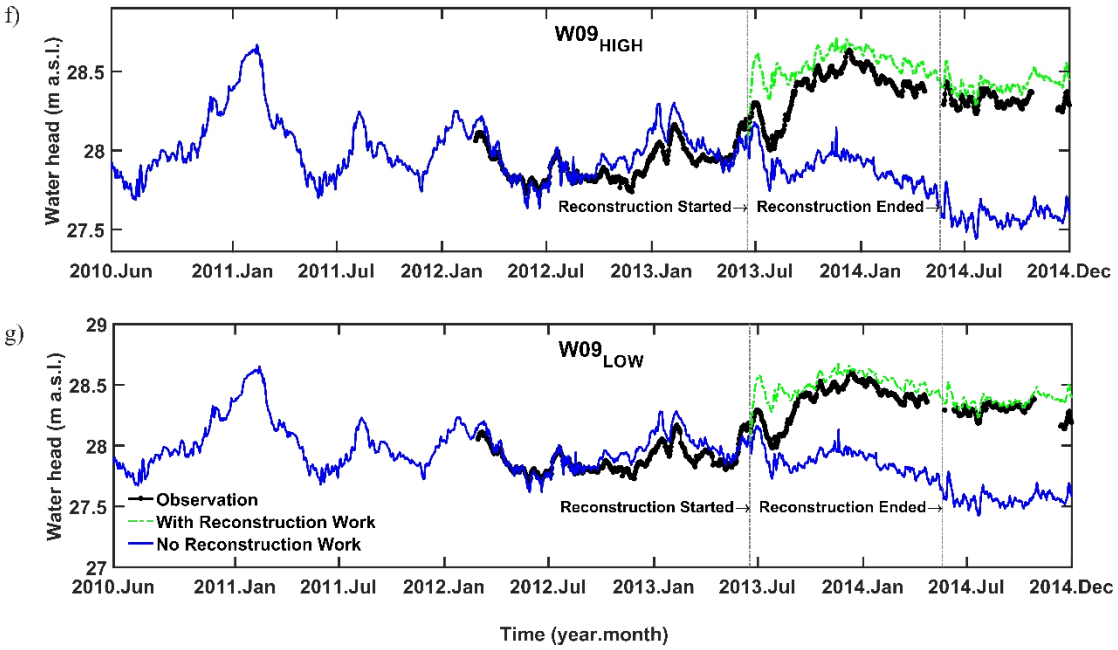

Fig. 4.2 Water head time series at near-bank wells (W05, W06, $W07_{HIGH}$, $W07_{LOW}$, W08, $W09_{HIGH}$ and $W09_{LOW}$) comparing observed values (black line) and simulated values for both the model scenarios without (blue line) and including the reconstruction work (green line).

As it is shown above in Fig. 4.2a, b, the simulation result of both W05 and W06 matched the observation result well before the reconstruction. The RMSE for both is below 0.15 m, while the Pearson's correlation coefficient was around 0.9. There was a period of mismatch one year before the reconstruction, starting from an observed decreasing trend in October 2012 and ending up by another increasing trend in March 2013. In the beginning time from October 2012 to November 2012, the simulated results increased in contrast with the decreasing observation, which drove a mismatch during this period. After reconstruction, a great discrepancy of W05 and W06 started a few months later, where a relatively continuous decreasing trend was shown in the simulation result, while the observation water head was stable in a plateau. By the end of the reconstruction, a drastic drop influenced by the new remediation wells nearby was simulated, however, in reality the drop is much less. This could be mainly attributed to the inaccurate local geological model.

Before reconstruction, $W07_{HIGH}$ and $W07_{LOW}$ (Fig. 4.2c d) were characterized by a moderate correlation level (<0.4), while other near-bank wells of W08, $W09_{HIGH}$ and $W09_{LOW}$ (Fig. 4.2e f g) showed much larger correlation level (>0.8). The mismatch period as W05 and W06, was also observed to a much larger extent at $W07_{HIGH}$ and $W07_{LOW}$, and to a smaller extent at $W09_{HIGH}$ and $W09_{LOW}$; that is almost at all near bank wells except W08. This could indicate that part of the main driving force influencing the water heads in that winter period might be missing. The winter 2012/2013 was characterized by a long period in time with

minimum daily temperatures below 0 °C, and average daily temperatures of only 2.4 °C. Potentially, freezing processes at the study site which were not represented in the numerical model might have caused this deviation between nominally observed and simulated water levels. For all simulations the hydraulic conductivity (also fluid viscosity and density) was constant in time and did not depend on temperature. This simplification may contribute to the general deviation of the simulation results compared to the observations. However, the temperature dependent variations in fluid viscosity and density for the given temperature range were rather small and thus the uncertainties caused by temperature dependent variations in hydraulic conductivity were much smaller than the general uncertainty in heterogeneous hydraulic conductivity itself.

Fig.4.3 Photo of the Nedlitzer Durchstich showing the ongoing construction work at 12.12.2013. Note that at the southern canal bank the old, clogged armourstones were already removed, a geotextile was placed at the channel bottom and that the new armourstones were still missing. The new armourstones were placed and canal bank reconstruction was finished between 12.12.2013 and 01.03.2014 (photo by Matthias Munz).

During and after reconstruction, $W07_{HIGH}$ and $W07_{LOW}$ were characterized by a moderate correlation level. For $W07_{HIGH}$ the short-term dynamics in the observed water level included a substantial drop of about 0.7 m on 12 January 2014, an increasing trend of around 0.2 m before a slow recovery of about 0.5 m until the end of February. After that, step changes were not captured by the model simulations (Fig. 4.2a). During this period the southern canal bank adjacent to W07 was renewed (see Fig. 4.3), i.e. a new geotextile was placed and covered with armour stones, potentially affecting the observed water levels at the nearby observation well W07 (distance between W07 and channel is only 13.2 m paired with a good hydraulic connection at this spot). From July 2014 onwards, the observed water level at $W07_{HIGH}$

continuously decreased until the end of the observation period (Fig. 4.2c). In December 2014 the water level at $W07_{HIGH}$ was close to the simulated water level of the model scenario without canal reconstruction, whereas the water level of the model scenario including canal reconstruction was about 0.6 m higher. This indicates that the better hydraulic connection between the canal and groundwater caused by the artificial decolmation of the canal bed at this canal section lasted for about 6 months only. The hydraulic connection there continuously decreased to its initial level before river reconstruction, probably by recolmation. Comparable effects were observed for $W07_{LOW}$ (Fig. 4.2d). These results agree with Schafer (2006) who confirmed that substantial riverbed colmation was observed at a bank filtration site of the Ohio River several months after commissioning. However, at this study site it was observed just for a local spot.

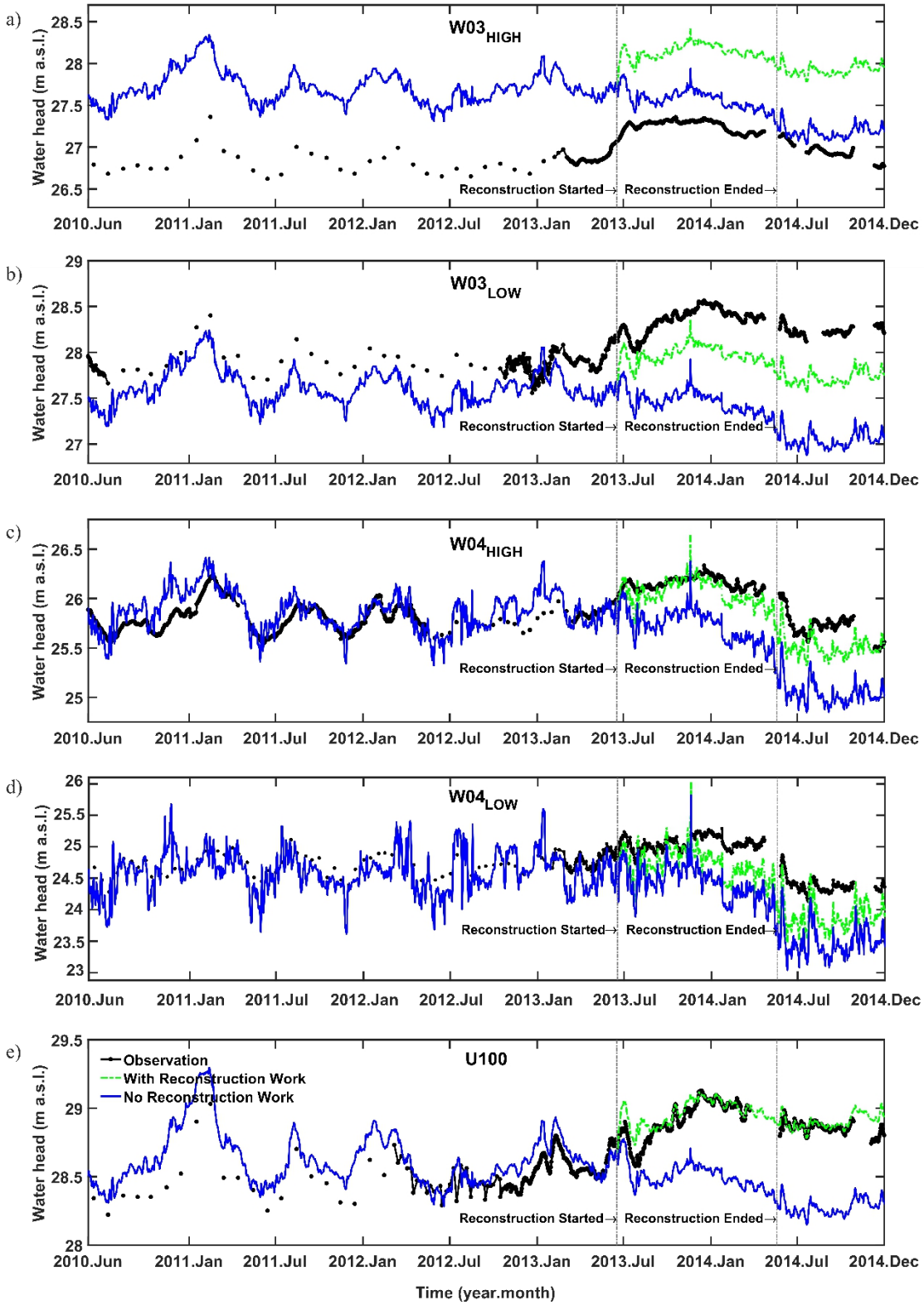

Fig. 4.4 Water head time series at $W03_{HIGH}$, $W03_{LOW}$, $W04_{HIGH}$, $W04_{LOW}$ and U100, comparing observed values (black line) and simulated values for both the model scenarios without (blue line) and including the reconstruction work (green line).

For the distant wells and deep wells, the simulation results were shown in Fig. 4.4. Among them, $W03_{LOW}$ was characterized by a moderate correlation level (<0.4). This mismatch is overemphasized by the continuous measurement starting in mid-October of 2012 with a short, spurious inverse trend, while the observed dynamic changes taking place beforehand were actually in accordance with the simulated result, but are likely not being taken into account in the correlation coefficient due to the sparsity of the data points. For $W03_{HIGH}$, it has shown the largest error of all the wells in group (ii) in the steady state, and it continues this tendency in the transient state (Fig. 4.4b). After reconstruction, although the rising trend could be reflected in the scenario of including the reconstruction, the absolute error was smaller in the scenario without reconstruction. The deviation in $W03_{HIGH}$ could be caused by the existence of low-conductivity material along the groundwater flow path from the canal not being captured in the geological model. For the most distant wells of $W04_{LOW}$ and $W04_{High}$, larger RMSE level was observed after the reconstruction while the Pearson's correlation coefficient increased at the same time. U100 showed the lowest RMSE level among all wells, both before and after the reconstruction.

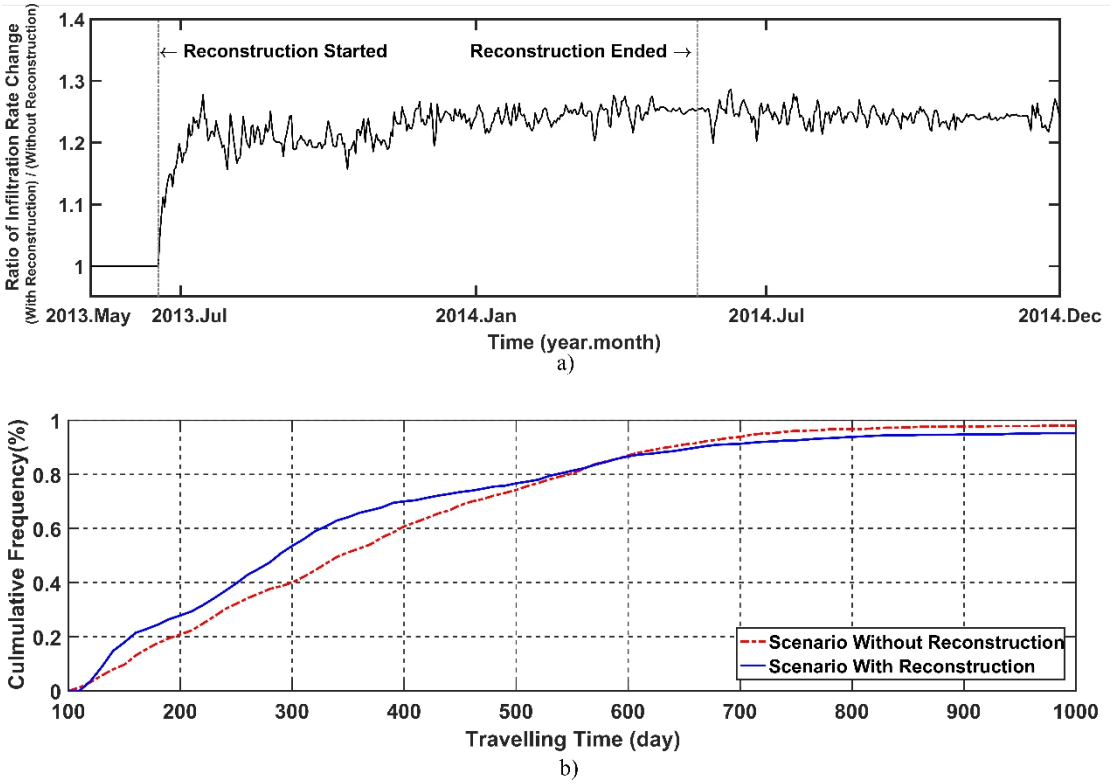

Fig 4.5 a) The ratio of surface water recharge to groundwater (infiltration rate) at the canal with and without reconstruction. b) Comparison of the cumulative distribution of flow path travel times (forward particle tracking from the bottom of the canal toward the pumping wells) on 30 June 2014, between the model scenarios 'with' and 'without' reconstruction. Points with traveling time longer than 1000 days are not shown in the graph.

The increasing riverbed hydraulic conductivity corresponds to the rising infiltration rate. The ratio of surface-water recharge to groundwater (infiltration rate) at the ND in both the scenarios with and without reconstruction is shown in Fig. 4.5a. It is evaluated as a net volume exchange from surface water to the groundwater by bank filtration during each day. The infiltration rate increases promptly together with reconstruction, which started by removing clogged riverbed and bank fortifications, and established a higher water level soon thereafter. On average, the bank filtration volume rate from the river increased by 23 %, i.e., 521 m^3/d, compared to the scenario without reconstruction (Fig. 4.5a). This increase is equivalent to around 9 % of the total pumping rate and will have led to some spatial rearrangement of well catchments and an increase in the already high share of bank filtration water abstracted by the waterworks.

Influenced by the increasing infiltration rate, the traveling time distribution must also change. The results of forward particle tracking prove that the travel time distribution is shifted towards shorter travel times (shorter than 550 days); i.e., subsurface residence time of water in the aquifer is reduced (Fig. 4.5b). Thus, flow paths with travel times between 100 and 550 days occurred more often in the model scenario including reconstruction compared to the scenario without reconstruction. For example, 55 % of flow paths had travel times shorter than 300 days whereas without reconstruction this would have been only 40 % of the flow paths. Also, an according decrease of long residence time (longer than 550 days) resulted, which has to be expected because pumping as the general driver was continuing on the same level as before.

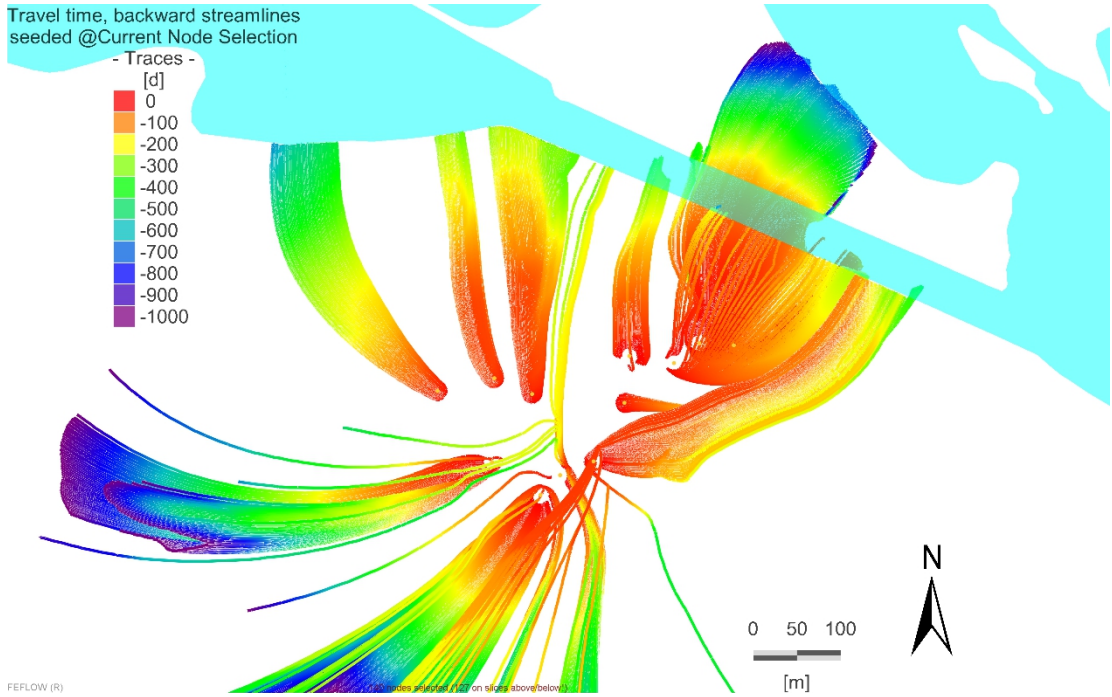

a)

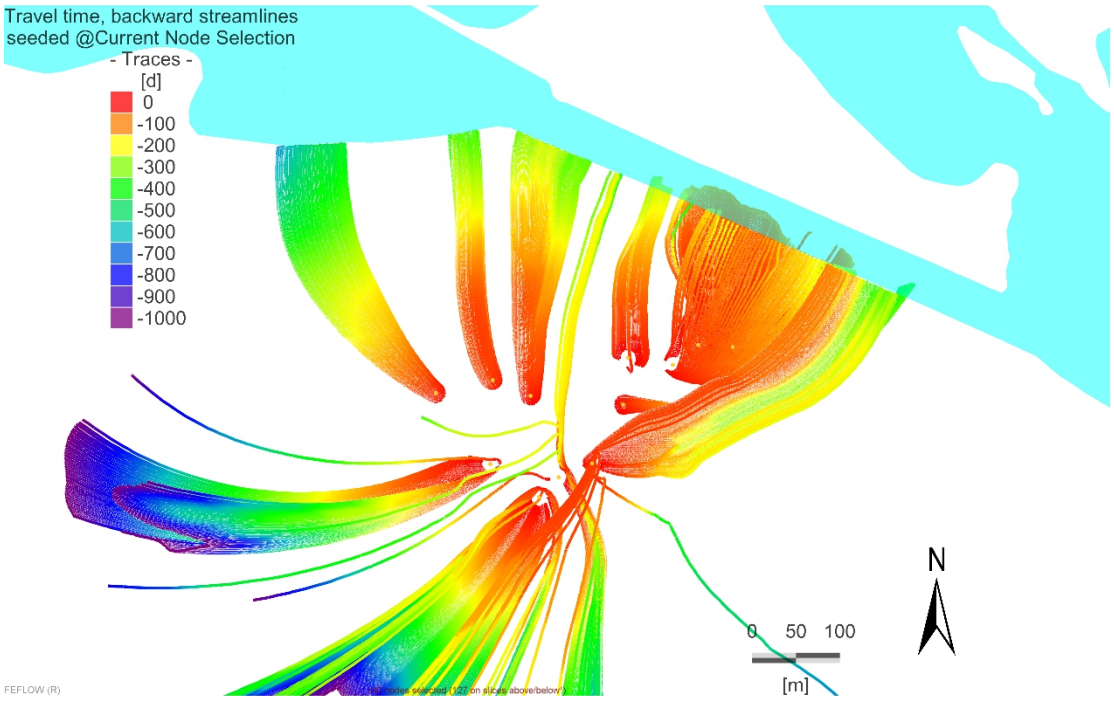

b)

Fig. 4.6 Simulated steady state backward streamlines starting from the individual pumping wells based on the boundary conditions of 30 June 2014, indicating representative snap shots of individual catchments. The graph a) represents the scenario without reconstruction and b) the scenario with reconstruction. These plan views show a 2-D perspective of the 3-D streamlines that generally pass through several geological units and may thus seem to cross each other in this plan view. Streamlines are color-coded based on their backward travel times.

Steady state backward particle tracking from the pumping wells indicates the general shape of the capture zones and corresponding subsurface travel times/residence times. Based on the boundary conditions of June 30th, 2014, flowlines were extracted for the model scenario without and with reconstruction (Fig. 4.6). For the scenario without reconstruction (Fig. 4.6a), the capture zone of the north-eastern pumping wells extends toward the adjacent canal with dominant subsurface travel times ranging between 50 and 150 days. Some flowlines could be tracked back to start at the northern lake "Krampnitzsee" with subsurface travel times up to several years. North-western pumping wells mainly received their water from the lake 'Weisser See'. Along these flow paths, the travel times ranged between 150 and 600 days. Only the southern pumping wells turned out to cover the southwestern area, larger part of the catchment. The reconstruction work caused some major changes in subsurface flow regime. The northern capture zone shrinks towards the canal, i.e., no flow lines were traced back anymore to the northern lake "Krampnitzsee" (Fig. 4.6b). The main reason for this substantial change could be attributed to removal of impermeable glacial tills below the canal bottom which had so far impeded the vertical infiltration from the ND. This made the nearby lake of same water level to deliver the water instead. After the reconstruction, part of the glacial tills were removed or replaced by more conductive material and the direct infiltration from the canal became the origin of flow paths. In contrast, no main differences in subsurface capture zone and corresponding travel times were observed in the southern catchment. Overall, the increased hydraulic connection between canal and aquifer caused a reduction in subsurface capture zone in the area north of the canal and shortened subsurface travel times from canal to pumping wells.

4.2 Result of Heat Transport Model

The thermal parameters of the transient heat transport model were assigned similarly to each sedimentary material (e.g., glacial tills, sand, sapropel) and changed individually in each geological unit by trial and error. Due to this moderate level of calibration the heat transport simulations still have the character of forward modelling. The calibrated thermal conductivities were 1.7 W m^{-1}/K for silt/glacial tills and 2.7 W m^{-1}/K for sand. The volumetric heat capacity slightly varied depending on geological composition between 2.5 MJ m^{-3}/K (silt/glacial tills) and 2.7 MJ m^{-3}/K (sand). The agreement between the simulated temperature and the observed ones varies in different wells (Fig. 4.7 and Fig. 4.8). Mean differences in time shift of the maximum and minimum temperatures ($\Delta\Phi$) and temperature amplitudes (ΔA) between simulated and observed temperatures for the time period after river reconstruction for all observation wells with substantial temperature variations are presented in Tab. 4.3.

Table 4.3 Differences in time shift ($\Delta\Phi$) and temperature amplitude (ΔA) between simulated and observed temperatures for the time period after river reconstruction for all observation wells (the minimum value is used for peak analysis).

Observation well	**Reference peaking time**	**$\Delta\Phi$ (days)**		**ΔA (K)**	
		Including Reconstruction	Without Reconstruction	Including Reconstruction	Without Reconstruction
$W07_{HIGH}$	20/08/2014	11	27	0.21	-1.68
$W07_{LOW}$	04/04/2014	13	34	-1.88	-0.48
W08	27/05/2014	-16	54	0.14	3.95
$W09_{HIGH}$	29/07/2014	-110	-50	-3.32	0.46
$W09_{LOW}$	24/06/2014	-63	29	-0.87	3.65
W05	17/06/2014	8	3	1.79	1.47
W06	17/08/2014	-7	-14	1.25	0.88

As shown in Tab.4.3, except the well set of W09, the differences in time shift ($\Delta\Phi$) in the scenario of including reconstruction in most of the near-bank wells is within two weeks, while the $\Delta\Phi$ for the scenario of without reconstruction could be up to 54 days (W08). Considering the time scale of the temperature circle, this suggested an acceptable match the temperature pattern. For both $W09_{HIGH}$ and $W09_{LOW}$, the time shift ($\Delta\Phi$) in the scenario of including reconstruction is quite large, which might suggest a possible misinterpretation in the local thermal flow field. In the scenario of including reconstruction, deviation of the temperature amplitude is within one Kelvin (K) in the wells of $W07_{HIGH}$, W08 and $W09_{LOW}$, larger than one Kelvin (K) in W05, W06 and $W07_{LOW}$ and $W09_{HIGH}$.

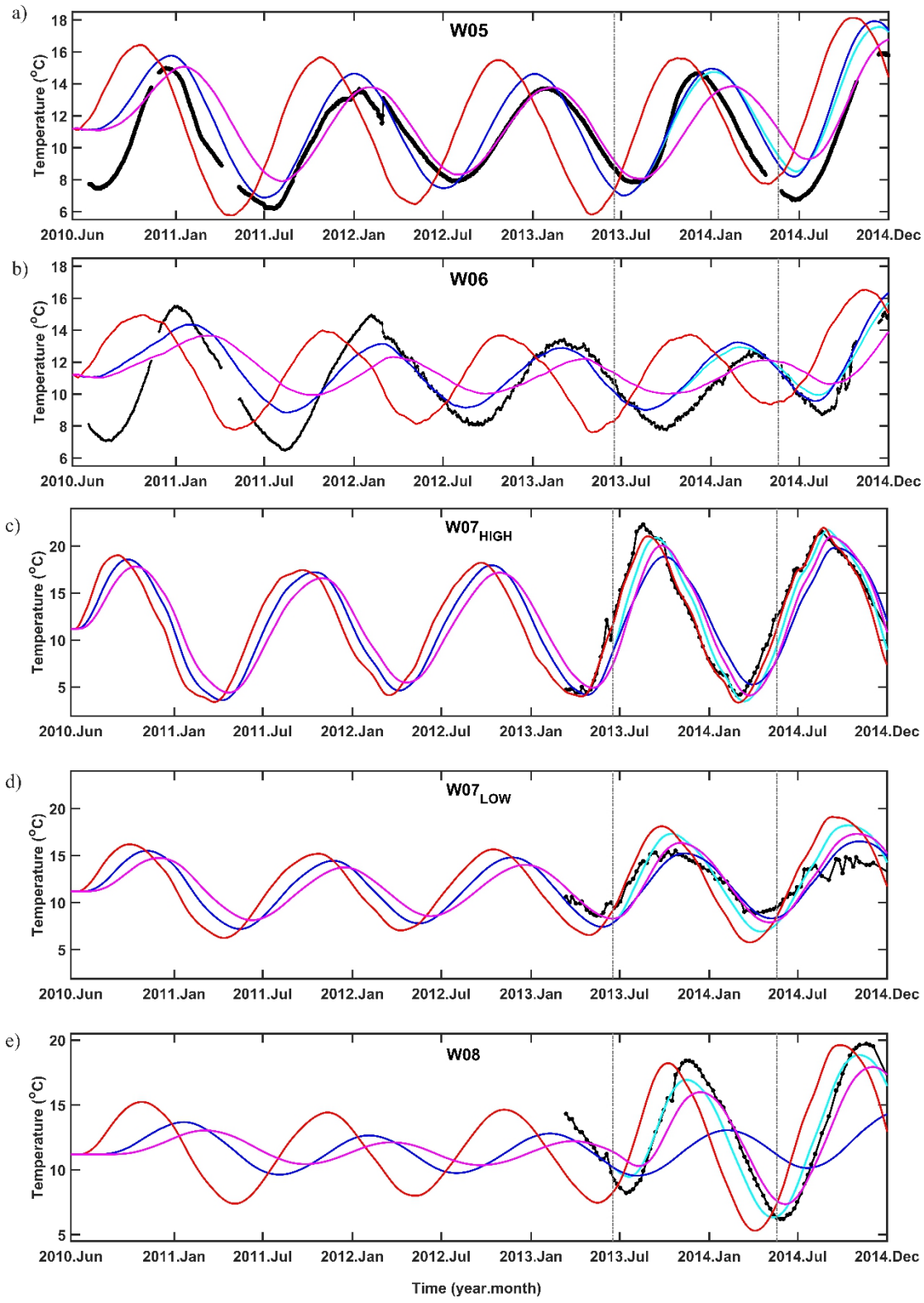
a)
W05
b)
W06
c)
W07HIGH
d)
W07LOW
e)
W08
Temperature (°C)
2010.Jun
2011.Jan
2011.Jul
2012.Jan
2012.Jul
2013.Jan
2013.Jul
2014.Jan
2014.Jul
2014.Dec
Time (year.month)

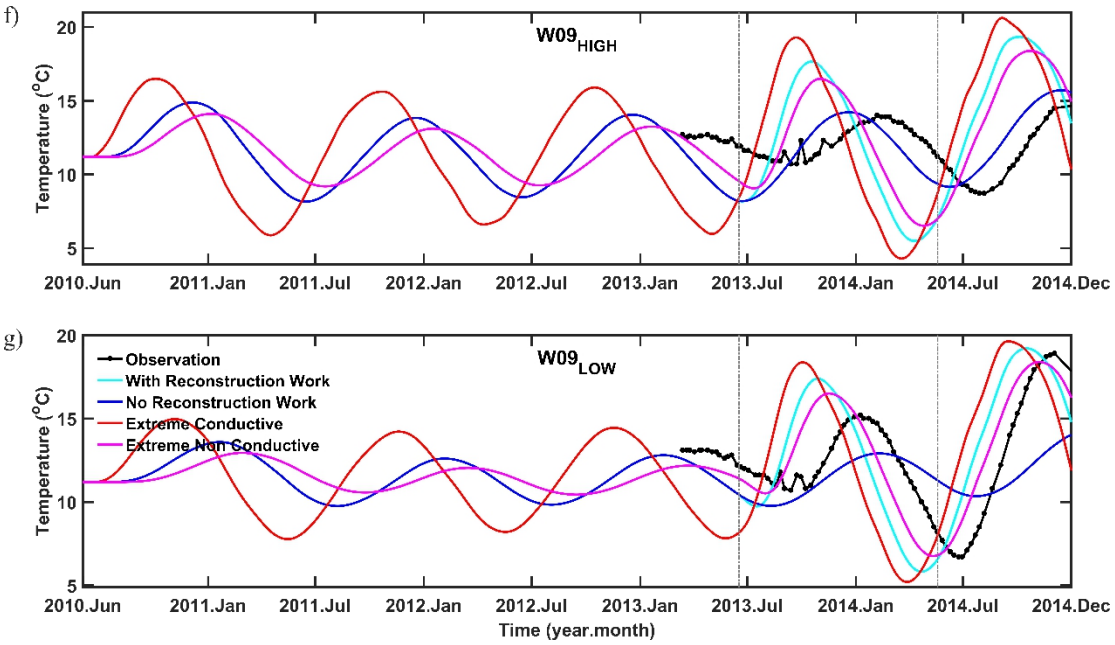

Fig. 4.7 Temperature time series at the near-bank wells (W05 and W06 $W07_{HIGH}$, $W07_{LOW}$, W08, $W09_{HIGH}$ and $W09_{LOW}$), comparing observed values (black line) and simulated values for both the model scenarios without (dark blue line) and including the reconstruction work (cyan line). Time series for the scenario with reconstruction are plotted for highly conductive thermal properties (red line) and low-conductive thermal properties (purple line) to show the possible range based on parameter uncertainty.

The model scenario including the reconstruction characteristically shows that after the start of canal reconstruction the temperature amplitude of the annual cycle increased and the arrival time of the peak became earlier (Fig. 4.7c-g, cyan lines) compared to the simulation scenario without reconstruction (Fig. 4.7c-g, dark blue lines). This general change in the temperature signal directly corresponds to an increased groundwater flow rate (i.e., increased advective heat transport), which is generated by the better hydraulic connection between the river and aquifer after the canal reconstruction. Furthermore, for W07 (Fig. 4.7c d) the match of observations on different levels supports a reasonable vertical representation of the groundwater flow distribution. In contrast, the temperature dynamics in W05 and W06 (Fig. 4.7a b) did not differ substantially between both model scenarios. This indicates that the groundwater flow field in the eastern catchment is not substantially affected by the canal reconstruction.

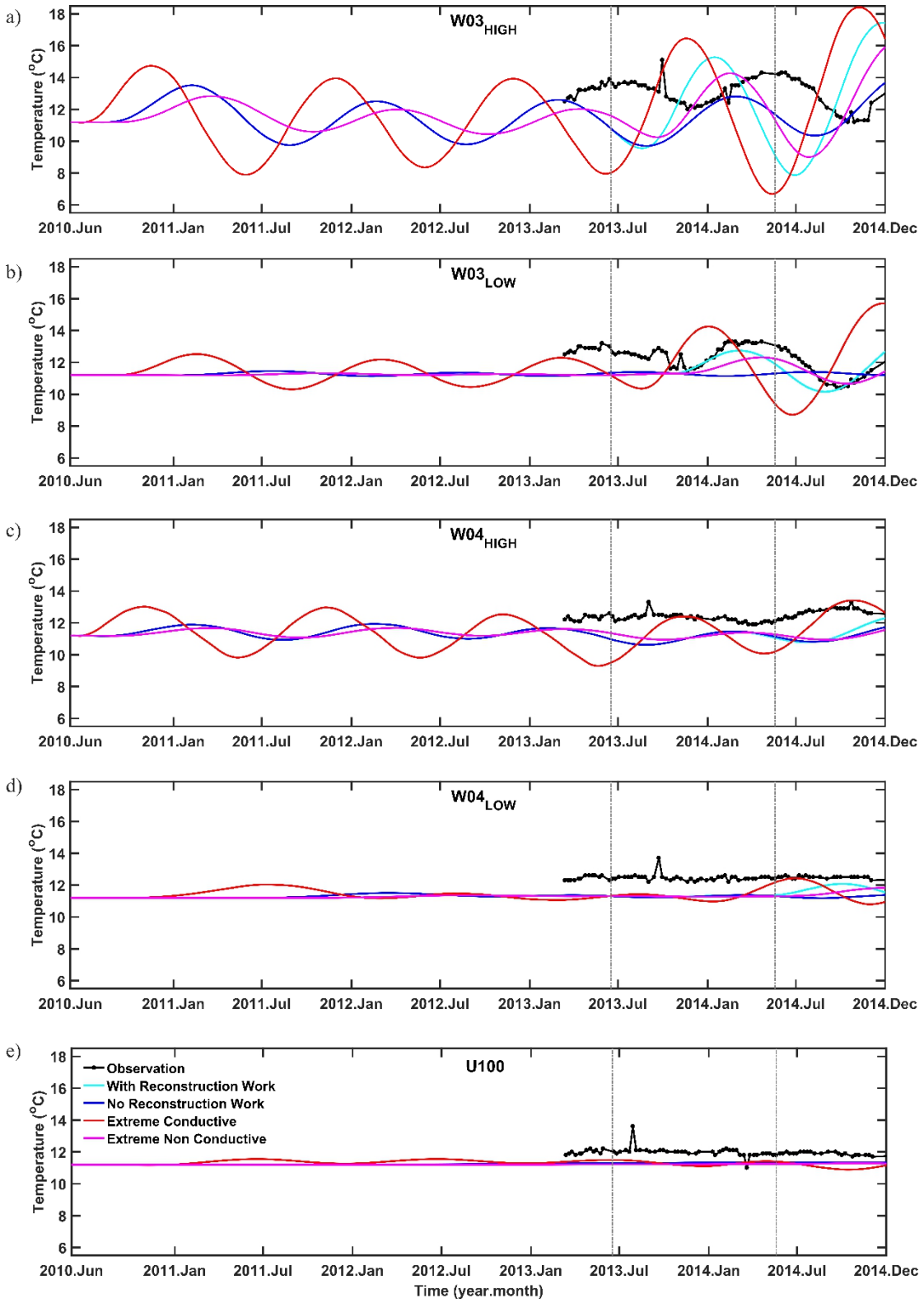

Fig. 4.8 Temperature time series $W03_{HIGH}$, $W03_{LOW}$, $W04_{HIGH}$, $W04_{LOW}$ and U100, comparing observed values (black line) and simulated values for both the model scenarios without (dark blue line) and including the reconstruction work (cyan line). Time series for the scenario with reconstruction are plotted for highly conductive thermal properties (red line) and low-conductive thermal properties (purple line) to show the possible range based on parameter uncertainty.

The observation wells $W04_{HIGH}$, $W04_{LOW}$ and U100 were characterized by almost constant temperatures throughout the year, which is well represented by both simulation scenarios (Fig. 4.8 c-e). The constant signal was not expected to be influenced by the canal reconstruction as the average yearly temperature (equal to long-term average in air/river temperature) is independent of the groundwater flow velocity. Mean simulated temperatures were 1.17 K, 1.12 K and 0.70 K lower than observed temperatures in $W04_{HIGH}$, $W04_{LOW}$ and U100 respectively. The greatest deviation between observed and simulated temperatures of the model scenario including canal reconstruction occurred in $W09_{HIGH}$ (Fig. 4.7f). The overestimated amplitude and underestimated arrival time of the temperature signal were caused by overestimated groundwater flow rates (advective heat transport). The model is not reproducing the slow flow regime in $W09_{HIGH}$, indicating that the hydraulic connection between the canal and the shallow aquifer is weaker than incorporated in the current geological model. Thus, the heat transport simulations here could indicate and rectify a local refinement of the geological model to be appropriate.

The temperature distribution is shown for a depth of around 10 m (±2 m) in Fig. 4.9 a-d. The zone adjacent to the river was characterized by strong seasonal temperature oscillations whereas the wells which are not located in the infiltration zone (U100, northern bank) or are far from the river (W04, distance to the channel ~126 m) were characterized by yearly constant temperatures. Driven by the strong hydraulic gradient from the canal towards the pumping wells, the seasonal temperature signal was transported into the saturated sediment via advection. Both maximum summer temperature and minimum winter temperatures infiltrated into the canal bed, and further penetrated into the aquifer, but were retarded to a certain degree depending on heat capacity and thermal conductivity of the sediment (i.e., the thermal front moves slower than the water particle or conservative solutes itself; the retardation factor of heat is about 2.15). Minimum temperatures in the canal occurred at the end of January (~1 °C). For the scenario without reconstruction, after 6 months (summer, 30th June) the cold front rose to 6 °C after traveling about 50 m from the canal, whereas the temperatures in the river already increased to about 20 °C (Fig. 4.9a). Variations in the transport distance (penetration depth) along the shoreline of the channel correspond to local differences in hydraulic conductivity, i.e., at W07 the cold front already passed at the presented summer snapshot (Fig. 4.9a). Analogously, the winter temperature pattern (Fig. 4.9c) could be interpreted in the same way. The rest of the aquifer tended to constant temperatures of ~11.4 °C (Fig. 4.9a, c). The seasonal temperature amplitude was completely reduced after a transport distance larger than ~100 m in the southern aquifer. In the northern aquifer, the penetration depth of the seasonal temperature signal (thermal front) was limited by heat conduction to roughly 1-2 m (Fig. 4.9a, c). In comparison, the reconstruction scenario

(Fig. 4.9b, d) shows a more continuous area of larger temperature variation range at the southern riverbank induced by the annually cycling canal temperatures which represents a more direct hydraulic contact caused by the canal bed reconstruction. The snapshot of the vertical temperature distribution at 30th June 2014 (Fig. 4.9e, f) illustrates that in the reconstruction scenario, the warm water from the canal could penetrate much deeper into the aquifer, almost reaching the model bottom, with less damping during its propagation. Further to the right-hand side, in the flow direction towards the pumping wells, the colder water from the previous winter has been dampened less and clearly shows a still lower temperature then for the scenario without reconstruction. Especially at the right side of the streambed, a better connection from the surface water into the aquifer has opened and acts as a shortcut towards the water works. Generally, the periodic temperature signal travelled further before it became flat, both in the vertical and horizontal directions. It is the evident that the reconstruction has driven substantial changes to water flow and heat transport at the surface-water/groundwater interface.

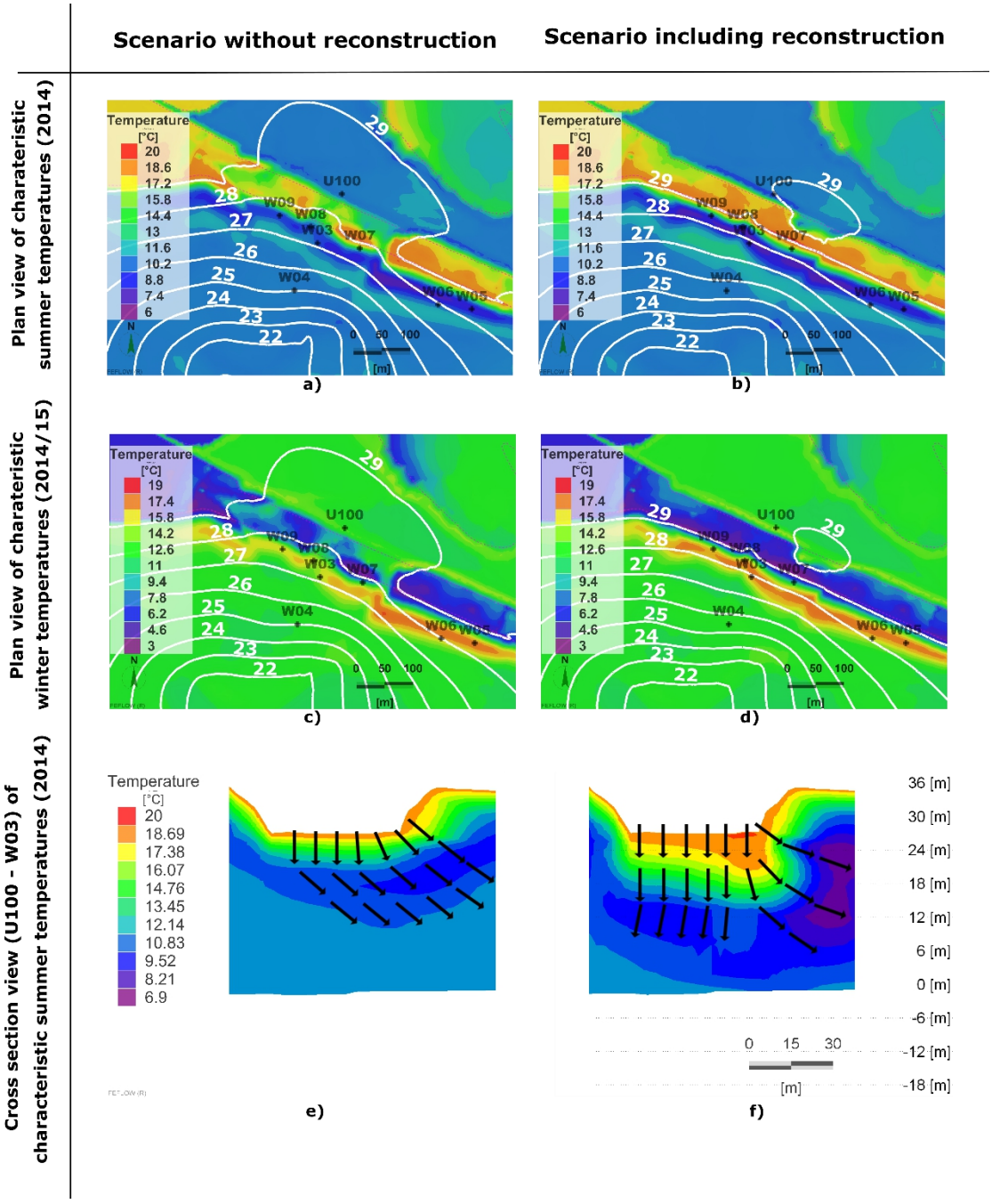

Fig. 4.9 Spatial temperature distribution (color-coded according to legends) and water head isolines (white) of the aquifer below WI-GT for a characteristic summer (30th June 2014) snapshot (a–b) and winter (31st December 2014) snapshot (c–d). Also shown is fluid flux and spatial temperature distribution of a cross-section between U100 and W03 for the characteristic summer snapshot (e, f). The fluxes are indicated by arrows representing fluid flow directions. All temperature patterns are shown for the model scenario without (a, c, e) and for the model scenario including canal reconstruction (b, d, f).

Chapter 5 Discussion and Conclusion

The 5.1.5 section of this chapter is adopted from the published article in Hydrogeology Journal named 'Impact of river reconstruction on groundwater flow during bank filtration assessed by transient three-dimensional modelling of flow and heat transport' by Wang et al. (2020), which can be accessed online as https://doi.org/10.1007/s10040-019-02063-3.

5.1 Discussion

5.1.1 Flow field

The study mainly painted the picture of an RBF field built on a heterogeneous geological composition and further evaluated the change brought by the river reconstruction project. As a general background of the study, the flow field was first investigated in chapter 3. Just considering the stable isotope results, a rough image on the stratification of the water source for shallow and deep aquifer can be described. The plotting result of the stable isotope data (^{18}O and Deuterium) before and during the reconstruction can distinguish the deeper wells of $W03_{LOW}$ and U100 from the other wells and the canal, while the assignment of $W04_{LOW}$ is ambiguous. This indicated that the remnant groundwater from further north also contributed to the pumping wells by flowing through the deeper aquifer, passing by $W03_{LOW}$, and further converged with the canal originated water at $W04_{LOW}$. For all the near-bank wells, surface water infiltrating from the nearby waterbody is dominant. The study of the water chemistry type confirmed the abovementioned conclusion, that the deeper wells of $W03_{LOW}$ and U100 were categorized as calcium bicarbonate water, while the near-bank wells together with the SW was classified as the calcium sulfate water. $W04_{LOW}$ showed ambiguity between those two types again, which is analogous to the result of stable isotope analysis. Furthermore, with the long sampling duration, the extension of the piper plot result into the post-reconstruction period demonstrated that on the southern bank side, the water in the deep aquifer was altered from the original type of calcium bicarbonate to calcium sulfate, which is closer to the hydrochemical type of the SW. This revealed a possible change of the flow field caused by the reconstruction leading to more canal-originated water flowing through the deep aquifer. This could be attributed to the increasing hydraulic connection between the canal and the aquifer, which can be well depicted by the general water head increase in all the observation wells. It started together with the reconstruction, rose to a new plateau of around 0.5 m higher, and then variated locally in its development. Afterward, no clear decreasing trend was observed, while W07 acted as an exception, which showed an earlier rise before reconstruction and then further dropped. Thus, it could be concluded that the reconstruction improved the water connection between the canal and the aquifer. Furthermore, the infiltrated water took a larger contribution in the flow of the deeper aquifer, replaced the remnant groundwater coming from the north.

Additional to the qualitative conclusions from the water quality analysis, a quantitative interpretation of the change caused by the reconstruction was enabled by employing a 3-D numerical model. Initially, a steady-state model supplied a calibrated catchment-scale flow field and checked the feasibility and consistency of the geological model. Based on the set of calibrated parameters, a transient model was implemented that allowed for the development of the bank filtration groundwater system to be tracked over several years, including the reconstruction period. During the calibration process, the abovementioned hydraulic head jump in observation wells was taken into consideration by a specific change of the hydraulic conductivity at the reconstructed area. This has proved to be a useful tool to quantify the effect of the reconstruction by being added directly to compare two model scenarios 'with' and 'without' reconstruction. This went far beyond just interpreting the measured time series. A key benefit of this modelling approach is that it eliminates the effects of changing hydrologic boundary conditions that otherwise would add uncertainty to the interpretation of the situation after reconstruction with inherently varying drivers hampering hard conclusions based only on experimental data. The increased hydraulic connection between the canal and the aquifer led to some spatial rearrangement of well catchments and an increase in the already high share of bank filtration water abstracted by the waterworks. This modelling result echoed the conclusion from the abovementioned water quality analysis. Furthermore, different from the description of merely a trend along the time axis in the water quality analysis, a quantification of the change could be achieved.

5.1.2 Redox zonation

The direct influence of the geological heterogeneity can be observed by the distinct pattern on the redox zonation, which is depicted by the electron acceptors. Among all near-bank wells, an anaerobic condition was consistently dominant, except $W07_{HIGH}$, where the seasonal change of the redox environment can still be observed. The DO and nitrate in $W07_{HIGH}$ peaked in winter and dropped as low as the other wells in summer (Fig. 3.7, 3.8), which simply portrayed the enlargement and shrinking of the oxic/suboxic zone along its flow path. Similar results have been shown in other studies (Kedziorek et al., 2008; Su et al., 2018). For other near-bank wells, a seasonal variation may also exist. However, it may have been squeezed into very limited space, which was not sufficient to reach the wells. Hence, the constant anaerobic condition was prevailing throughout the whole sampling period. A similar result was found in the investigation of the Oderbruch polder by Massmann et al. (2004), where the system reached the anaerobic environment within one day after infiltrating. The abovementioned redox zonation dynamic for shallow near-bank wells could be simply illustrated, both spatially and temporally. Shown in Fig. 5.1, the purple dashed line stands for the approximate boundary of the oxic/suboxic in the wintertime, where a much broader

dimension is along the flow path of $W07_{HIGH}$. For the rest of the near-bank area, the oxic/suboxic boundary is simplified as a straight line parallel to the canal (Fig. 5.1), although in reality, it might be shaped as a curve line and vary locally. For the summertime, the redox zone would shrink back and become denser. Therefore, in Fig. 5.1, the brown, dashed line closer to the canal is used to represent the boundary of the oxic/suboxic zone. Further beyond the oxic/suboxic zone, the potential on the dissolution of iron and manganese as the following electron acceptors was evaluated by ETC values. This demonstrated that both iron and manganese could be released among all observation wells but $W07_{HIGH}$. However, manganese solely rose in $W09_{HIGH}$ and $W09_{LOW}$, which hinted at prevailing scarcity of manganese but an existence of manganese-rich areas along the flow path to the wells of W09. Further mixing with the water through other flow paths, the manganese level in the distant well was diluted. In contrast, the increase of iron (II) was shown everywhere, except $W07_{HIGH}$, which indicated a ubiquitous iron (III) dissolution in the RBF field. For sulfate, a lower level was shown in the deep wells than in the shallow wells, albeit, compared with the sulfate concentration in the canal, there was no direct evidence showing the reaction of sulfate during the propagation.

The reconstruction could have changed the distribution of the redox zonation, however, the mechanism behind could be complex. As it was shown in the flow field and thermal field modelling, the reconstruction drove the surface water infiltrating at a higher rate and consequently increased the propagation distance of the annual temperature cycle (Fig. 4.9). Therefore, it created two opposite conditions for the relevant biochemical reaction, 1) a relatively shorter residence time which may impede the reaction, and 2) a higher temperature during the warm seasons which could boost the reaction. Another important controlling factor is the biochemical reaction zone at the riverbed, which supplied a relatively stable environment and substrate. The influence brought by the dredging and the newly paved material was hard to predict and conceptualize in the modelling study. Thus, given the current accuracy level and the uncertainty caused by the great geological heterogeneity, it was difficult to consider all the above mentioned influential factors in the modelling study. Per contra, as an alternative option, the simple interpretation of the water quality analysis with a statistic test could supply a conclusive evaluation of the substantial change for different solutes, and further show the trend by comparing the median value. In this study, the change in the redox environment was depicted mainly by iron and manganese concentration since both DO and nitrate were mostly consumed throughout the sampling period. As it was written in Chapter 3, the significant difference of the iron concentration was shown in most of the wells, except both wells of W07, $W03_{HIGH}$, $W04_{HIGH}$, while the global drop of the median level was observed except for $W07_{LOW}$ (Tab. 3.2). However, for manganese, the contradictory substantial change could be reflected by the increasing median concentration at most distant

wells and $W09_{LOW}$. Therefore, instead of a global trend, the redox change should be considered well by well.

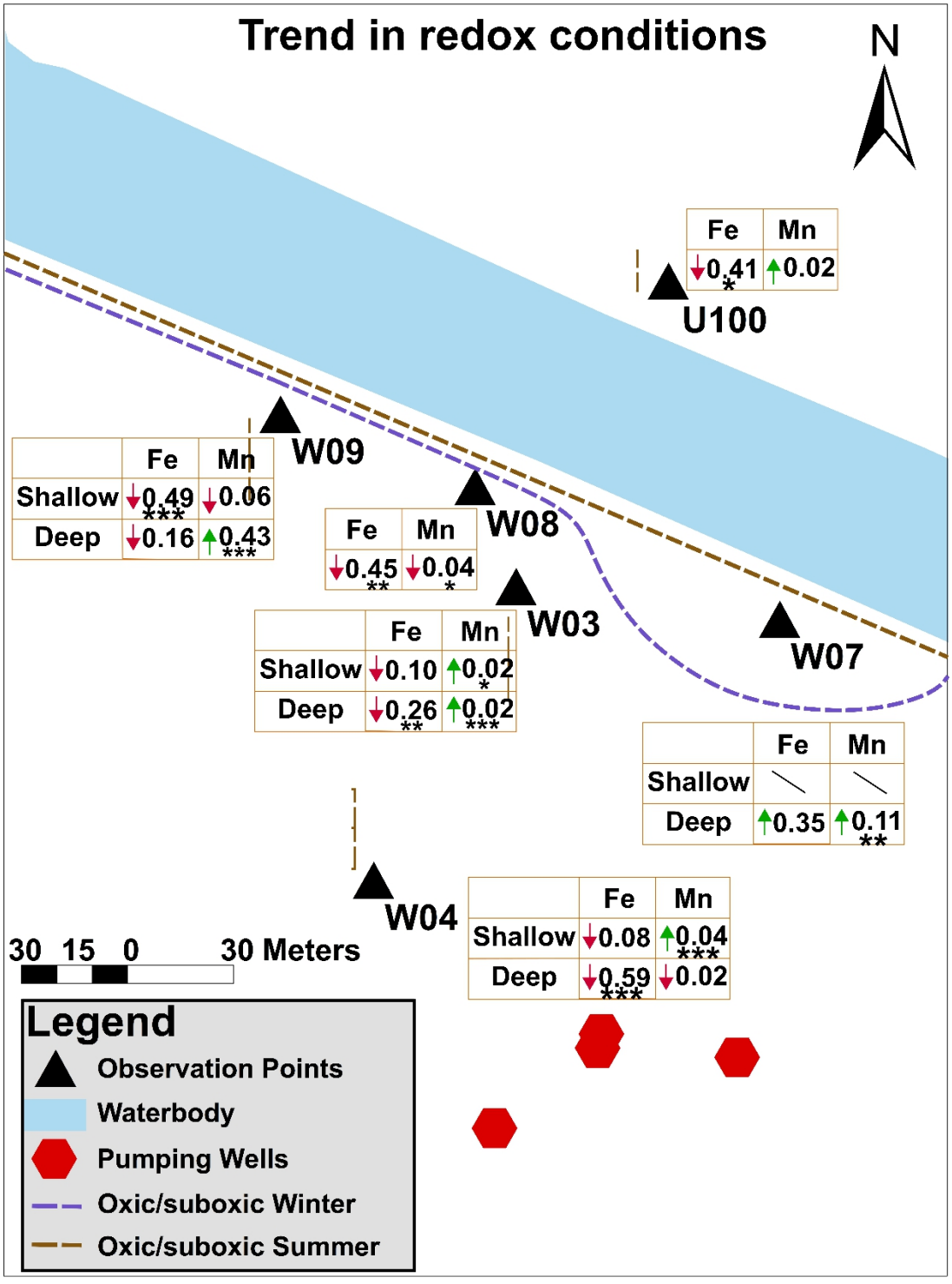

Fig. 5.1 The change of the median dissolved concentrations of manganese and iron in the observation wells after reconstruction, subdivided for the upper and lower part of the aquifer, and the seasonal change of the oxic zone in the near-bank area. The upward/ downward arrow stands for the increase/ decrease in median concentration increase, while the number stands for value. The '*' stands for the

level of significance. The dashed lines stand for the boundary of the oxix/suboxic zone at the depth of shallow aquifer in summer and winter respectively.

The change of the median Mn (II) and Fe (II) concentration was shown in Fig. 5.1. For near-bank wells, in $W07_{HIGH}$ and $W07_{LOW}$, the more reductive condition was shown by a larger DO consumption in the wintertime ($W07_{HIGH}$) and the rising median iron and manganese concentration ($W07_{LOW}$). In $W09_{LOW}$, a declining median level of iron was observed, however, the change was not statistically significant. Oppositely, the significant ($P<0.0001$) change with declining manganese median level suggested a more reductive environment (Fig. 5.1). In W08 and $W09_{HIGH}$, the declining median level of both iron and manganese indicated a more oxic environment. For distant and deep wells, the median level change between manganese and iron was mostly opposite. Taking the statistic significance in consideration, the more reductive environment was observed in $W03_{HIGH}$, $W04_{HIGH}$, while the more oxic environment was observed in $W04_{LOW}$ and U100. The ambiguity was within $W03_{LOW}$, where both the Mn and iron showed significant change with opposite median level change trend. Altogether, this hinted that the redox change was quite site specific. By further considering the small absolute change in median value (iron < 0.6 mg/L, manganese < 0.45 mg/L), the influence was not drastic.

5.1.3 Treatment efficiency

Besides the evaluation of the redox zonation, the improvement of the water quality by the RBF site was also evaluated. For inorganic matter, the influence of the reconstruction is different for each solute species. Both before and after the reconstruction, the removal of nitrate was quite complete. Except for $W07_{HIGH}$, most of the observation values were below the detection limit. It hinted that the current setback distance is large enough for the removal of nitrate, even after the reconstruction project. For sulfate, the rising median value after the reconstruction suggested a rising trend among all wells. However, due to the increase of the sulfate level in the canal, the increment can simply be the response of the RBF system. For iron (II), as one of the main cations, a global decrease in the median value could be found after the reconstruction (Tab. 3.2), and the largest drop was observed at the most distant well $W04_{LOW}$. For manganese, after the reconstruction, there was a substantial difference in most of the wells with increasing median value. However, as discussed in 5.1.2, the absolute change was tiny (smaller than 0.43 mg/L). And for the most distant well $W04_{LOW}$, there was even a drop in the median concentration (from 0.28 mg/L to 0.26 mg/L). Therefore, no extra concern should be considered in controlling the iron (II) and manganese concentration after reconstruction. The only value that rose concern was the ammonium level in well $W03_{LOW}$, where the median value has doubled after the reconstruction. With a parsimonious estimation,

the nominal retardation factor was estimated between 4.5 and 8.1. However, due to the data gap, the peaking time could be even earlier, and a smaller retardation factor could be expected. By estimation, the peak of the ammonium will reach $W04_{LOW}$ latest by February 2024. However, the peaking concentration could be further dampened by sorption and diluted.

For organic matter, a seasonal pattern of DOC was observed neither in the canal nor in the observation wells. The removal happened more intensively in the near-bank area. After reconstruction, a significant change of DOC level in the surface water ($P<0.05$) was observed with a decrease in median level, but not in the observation wells ($P>0.05$). Further estimation with the median DOC level showed the removal efficiency at $W04_{LOW}$ decreased slightly from 42% to 38%, while a much larger variation range was observed in the near-bank area. Among them, the highest level was measured in November and December 2013, when the reconstruction was ongoing. It might be attributed to a time slot when the old reaction layer was removed, and the new one was not yet fully formed. Besides DOC, POC was also involved in the redox reaction as an extra electron donor, which was consistent with previous studies (Doussan et al., 1997; Grischek et al., 1998). However, a clear quantification on the portion that POC and DOC took separately was hard to evaluate. As it was shown in Fig. 3.17, the median value of the estimated CH_2O consumption was mostly higher than the maximum DOC level in the surface water. This suggested that the POC could even be a more dominant contributor in the redox reactions. Similar results were also shown in different studies (e.g., Doussan et al., 1997; Grischek et al., 1998). This suggested an additional source of POC compensated the deficiency caused by the removal of the riverbed. As it was mentioned in the introduction (chapter 1.3.2), it could be contributed by the infiltrated surface water or the aquifer matrix (Grischek et al., 1998; Hoppe-Jones et al., 2010).

5.1.4 Rehabilitation and reclogging process

Besides the general view about comparing the results before and after reconstruction, another important issue to be addressed is how the RBF system performed during the change. Specified by Hiscock and Grischek (2002), the colmation layer acts as the biologically active zone with the function of ‘intensive degradation and adsorption processes’. It is also an important pool of organic carbon for the series of bioreaction (Bretschko and Moser, 1993; Grischek et al., 1998). Due to the deep dredging depth (2 m), not only the old colmation layer but also a large part of the former hyporheic zone was removed. Therefore, a sudden change would act on the water treatment efficiency, and a period of time would be required before a new balance was reached. A vital question to be answered is the performance of the RBF site before reaching this time point. The recovery from the reconstruction would consist of the rebalance of the hydraulic connectivity and the rehabilitation of its treatment capacity.

The main process for the rebalance of the hydraulic connectivity would be clogging or to say reclogging in this case. As it was discussed in the introduction, main studies on this process were limited to lab experiments. Eleven studies are reviewed and summarized in Fig. 5.2. Among them, most cases indicated a clogging time in tens of days, while the decrease in hydraulic conductivity could vary from one to three orders of magnitude. However, since the plotting in Fig. 5.2 stands for the performance of the combined layer along the whole experiment period, the drastic initial drop happened much faster at the top layer. Some studies showed the hydraulic conductivity in the top layer was reduced by three orders of magnitude within 15 days (Engesgaard et al., 2006; Taylor and Jaffé, 1990; Vandevivere and Baveye, 1992), by one order of magnitude within seven days (Schälchli, 1992; Schiff and Johnson, 1958). Within one day, an initial hydraulic conductivity decrease of 80% during 2 hours was also shown in the experiment for sand column due to the particle mobilization driven by the hydrodynamic forces (Pavelic et al., 2011). In an extreme case investigated by Du et al. (2014), the impermeable surface clogging was formed within 3 hours, which drove the hydraulic conductivity to almost zero. To connect with this study, the reconstruction process was carried out along the whole year. Therefore, such a fast clogging could happen in parallel with the reconstruction process. Even in the relatively shorter time slot between the completion of the dredging and replenish of the new filling material, the bare riverbed may also form a clogging layer due to the quick initial clogging speed. Furthermore, Ragusa et al. (1994) found that hydraulic conductivity would strongly decrease with increasing turbidity, which is similar to condition caused by dredging operation in this study. In summary, the increase of the permeability on the riverbed may be compensated by an immediate reclogging process. Besides the removal of the clogging layer, a special feature in this study was the removal of the impermeable glacial tills below the riverbed. Not being continuous, it created geological windows, which allowed hydraulic connections and reconstruction increased this connection. Besides an instant response of the short-term clogging during the reconstruction, a long-term clogging effect also happened. In this study, it was not observed except for W07, which kept the decreasing trend throughout the whole period after the reconstruction. This implied the reclogging effect happened just locally at the infiltration area contributing to W07. Similar long-term clogging was observed by Wett (2006), where the clogging layer built-up was observed by one year with one order of magnitude decrease in hydraulic conductivity.

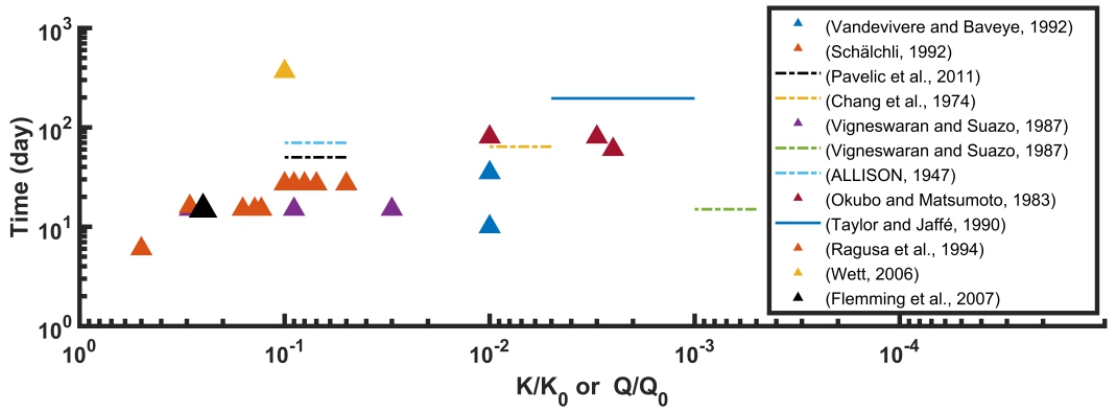

Fig. 5.2 Review of previous studies on the clogging process expressed by the ratio of hydraulic conductivity or infiltration rate. K_0 and Q_0 stand for initial hydraulic conductivity and infiltration rate. The dashed line stands for the decrease of K or Q could be further smaller, but not accessible from the literature.

For the rehabilitation of treatment capacity, no studies about riverbed reconstruction could be taken as a reference for the RBF site, while the scouring effect from the natural flooding has been discussed in the intro. However, a similar problem has been met in slow sand filters. During the filtration process, a layer (mentioned as 'schmutzdecke' or 'dirty skin') composed of 'dirt and living and dead micro and macro-organisms' would grow on the filter surface and may act as a barrier enhancing the filtration efficiency (Ray et al., 2003; Cleasby, J.L., 1990). Due to its increasing impedance to the infiltration rate, a periodical cleaning process (once in 1 to 6 months, according to Cleasby (1990)) will occur at the end of each operation cycle (Ray et al., 2003). It mainly includes the removal of the top layer (scraping) and replenishment of the filter bed (resanding) (Cullen and Letterman, 1985). The cleaning process was always succeeded by a ripening period, which varies from 6 hours to 2 weeks (mostly below two days, according to Cullen and Letterman (1985)), aiming at the recovery of the treatment capacity. To connect with this study, instead of a quick impulse like cleaning in slow sand filtration site or flooding, the dredging and the replenishment of the riverbed lasted for one year. Therefore, the much faster ripening process would happen in parallel with the continuous reconstruction work. This is similar to the abovementioned short-term reclogging process.

Reflected by the DO level, a stable aerobic respiration rate and the in-time recovery of the related processes could be concluded during the whole reconstruction period. It could also be found in other investigations. Normally, the electron transport system (ETS) activity was used to measure the respiration process of DO consumption. In a field study, Claret (1998) found the ETS active bacterial abundances reached the peaking value in three to five days in the downwelling zone below the riverbed. Another field investigation by Sabater and Romaní

(1996) showed that the ETS activity per unit area at the newly buried unglazed clay tiles increased drastically on the fourth day and then behaved without significant difference with the old tiles. For nitrate, the conclusion would be hard to draw due to the under-sampling (only three sampling events during the reconstruction period). However, as it was shown in Fig.3.9b, d, f, the nitrate value of $W07_{LOW}$ W08 and $W09_{LOW}$ peaked during the reconstruction time, which may hint the instability of the sub-oxic zonation in the near-bank wells and the decrease of the denitrification efficiency during the ripening period. The reason might be attributed to the absence of the biofilm within the clogging, which may not only supply the reactant but also a reaction environment. Within the aerobic zone, the biofilm would allow the happening of denitrification process by creating a micro-environment - anaerobic pocket (Storey et al., 1999). Therefore, a relatively lower nitrate removal efficiency could be expected before the full development of the biofilm. It can lead to a breakthrough of the nitrate in the near-bank wells. However, with sufficient setback distance, the escaped nitrated might be further utilized along the later flow path. This also hinted at a possibility that the regrowth of the species based on aerobic respiration is faster than the anaerobic species after the reconstruction. For the following electron acceptors, no noticeable change was observed in manganese and iron, which might be attributed to under-sampling. The peak DOC level was observed in the near-bank wells of W08, $W09_{LOW}$ and $W09_{HIGH}$ during November and December 2013. The concentration was between 7.9 and 9.3 mg/L, which is around 38% to 63% higher than the median DOC level. This suggested a possibility of the preferential flow and the breakthrough of the DOM matter during the ripening period.

Different from the rise of the nitrate and DOC, which mainly happened during the reconstruction period in the near-bank wells, the continuous high ammonium concentration was observed hundreds of days after the completion of the reconstruction at the deep distant well $W03_{LOW}$. As it was explained in chapter 3.5.4, this breakthrough can be traced back to the removal of the clogging layer and deep hyporheic zone during the reconstruction period. Besides acting as the primary reaction zone for nitrification and anammox, the original clogging layer and the hyporheic area may also largely retain the further propagation of ammonium by its high Cation Exchange Capacity. In pace with the later reconstruction, the old colmation layer was largely removed, while the newly paved riverbed was not yet capable of keeping the newly produced ammonium by sorption. Therefore, the ammonium escaped from the hyporheic area before reacting and propagated further downstream. Different from nitrate, which could react along the whole traveling path, the decrease of ammonium needs either oxygen or nitrate as co-reactant. Hence, after passing the oxic and suboxic zone, the ammonium would rather become a persistent solute in the groundwater field. This breakthrough of ammonium can give a hint for the future reconstruction work on RBF sites. When the CEC level of the new filling material is comparable with the old one can strongly

influence the ammonium level. This is especially true for RBF sites with great ammonium increase near the riverbed area, e.g., the RBF site at Seine river, France (Doussan et al., 1998) or high background concentration in the SW, e.g., the RBF site at Yamuna river, India (Groeschke et al., 2017). However, the CEC level of the riverbed is positively correlated with the mass fraction of clay and organic matter (McBratney et al., 2002; Seyed Jalali et al., 2019). Therefore, after the pavement, it may gradually increase by the sedimentation and reclogging process. The span between the reconstruction and the point when the comparable CEC level was reached would be the time window for the possible ammonium leakage.

In summary, the fast recovery was due to the aerobic respiration, where no obvious DO breakthrough was observed. For nitrate, a possible breakthrough in the near-bank wells happened, albeit it was uncertain due to limited data availability. However, it could be further reacted along with further groundwater flow. The longest recovery time would be the ammonium treatment capacity, which is based on both the rehabilitation of the microsystem and the CEC level in the riverbed area. The infiltrated ammonium may become persistent along the following flow path and influence the final water quality. The change of the ammonium concentration is however hard to evaluate due to the missing of the peak in sampling.

5.1.5 Heat transport model

Featured as a naturally occurring periodic signal with easy and rapid measurement, the time series of temperature shows greater sensitivity to variations during transport and is above potential environmental noise when compared to conventional or pulse tracers (Constantz, 2008; Cox et al., 2007; Mahinthakumar et al., 2005). Munz et al. (2017) illustrated that by taking heat transport into consideration, the model non-uniqueness could be better constrained and the accuracy of flux estimation across the interface between surface water and groundwater could be improved. Delsman et al. (2016) demonstrated that conditioning the model to temperature measurements could worsen other model results such as electrical conductivity and salinity but also recognized that this could be mainly caused by errors in the model structure itself. Few studies so far have used heat as a natural tracer for the numerical modelling of bank filtration. One of them is Henzler et al. (2016), who especially investigated its details with 3-D modelling of flow and heat transport in areas with geological heterogeneity.

In this study, by employing a 3-D numerical model for transient water flow and heat transport incorporating the heterogeneous geological structure, it was only partly possible to match both the seasonal temperature patterns and water heads at the same time. However, substantial

deviations can be used to trace back shortcomings of the model structure, and heat transport can help as an additional test to evaluate model performance and realizing model limitations. The head simulation results at W09 showed the lowest root mean square error and the highest Pearson's correlation coefficient (see section 'Steady-state flow modelling'), but also substantial deviation between observed and simulated temperatures. The poor match in the temperature pattern of W09 indicated an overestimation of water flux, which could not be compensated by reasonably adapting the thermal parameters (Fig. 4.7f g); i.e., the hydraulic connections in the geological structural model, especially between the canal and the two aquifer layers leading to W09, did not represent the real situation well, and could be adapted based on this insight resulting from temperature observations and heat transport modelling.

5.2 Conclusion and outlook

With an intensive and long-term monitoring program, it was possible to observe the seasonal behavior of the bank filtration system, as well as its development, during and after the reconstruction of the ND canal as the main supply of bank filtration water towards the pumping wells of the waterworks. Evidenced by both the stable isotope analysis (^{18}O and Deuterium) and the piper plot results, a simple two-layered stratification of the flow field could be shown. Additionally, an increasing contribution of canal-originated water in the deep aquifer can be demonstrated by shift of piper plot distribution in deep wells. This could be due to the artificial decolmation which had substantially increased the hydraulic connection between the canal and the aquifer. The change started to take effect directly at the beginning of reconstruction, intensified during the reconstruction period, and had a clear effect after it was accomplished. With the help of a 3-D flow and heat transport numerical model, the conclusion could be reached that, on average, the bank filtration rate along the canal has increased on average by 23%. Furthermore, the increasing flow rate substantially changed the subsurface travel time distribution towards shorter travel times. Flow paths with traveling times below 200 days increased by around 10 % and those below 300 days by 15 %. Correspondingly, for the thermal field, the seasonal temperature cycle brought by the SW propagated further in the scenario with reconstruction (reality).

The geological heterogeneity has strongly influenced the distribution of the redox zonation, leading to a continuously dominant anaerobic condition in most of the wells. This is true except for $W07_{HIGH}$, where the seasonal dynamic between oxic/suboxic and anaerobic condition could be observed. The influence of the reconstruction on the redox condition varies locally, however, inasmuch as the small concentration level, this change in the redox environment was mostly very small. The current setback distance is sufficient for a complete removal of nitrate and at the same time kept the manganese and iron from largely increasing.

After reconstruction, no deteriorating effect on the water treatment efficiency was observed. For most of the concerning water quality items, the median level kept constant or even dropped after the reconstruction. Although a few substantial differences were found, the absolute increase was still quite small as measured by its low concentration. An exceptional case was the continuous high ammonium level, which was observed hundreds of days after the reconstruction. A plausible explanation was that the reconstruction removed the clogging layer, which previously retained the ammonium for further reaction. By estimation, this peak of the ammonium would further reach $W04_{LOW}$ before February 2024.

As it was discussed in this study, the rehabilitation time in the repaved riverbed may vary for different degradable substances, while the possibility of the breakthrough increases along with the length of the time window. The under-sampling, both temporally and spatially, very much limited the characterization of the recovery process (e.g., for nitrate and ammonium removal in this study). Spatially, the number and the distribution of the wells inhibited forming a fine resolution of the monitoring network. To highlight the recovery process in the riverbed, it is better to install observation points right below the reconstruction bottom directly after the repavement or at the bank with very little distance to the waterbody, lining up horizontally along the flow gradient. Currently, the near-bank wells are of more than ten meters away from the canal and thus the concentration curve has been strongly dampened. For the vertical direction, instead of intensive drilling, a good compromise could be setting up multi-level sampling, which could improve the sampling resolution with a limited number of observation wells. Temporally, for the regular monitoring on the RBF site, the logger-recorded water head and the biweekly sampling frequency for temperature are sufficient for describing the temporal dynamic. However, the recovery time may vary from hours to days. Therefore, more intensive sampling events are required during this period. Before the reconstruction, a pre-monitoring on the riverbed is also essential, including general analysis of the pore water, the local biomass, and the CEC level. This can help to forecast the possible breakthrough and estimate the degree of rehabilitation.

Generally, the glacial tills could be confining layers by its complex composition, medium particle characteristics and heterogeneous distribution at subsurface (Dragon, 2006; Henzler et al., 2014; Odling et al., 2015; Shaw et al., 2013). The heterogeneity caused permeable channels for surface water infiltration locating at different depths for different wells even though the wells share a similar distance to the adjacent river. The discrepancy of permeability induced by geological heterogeneity can generate a disparity in redox reactions and redox zonation at RBF sites. Low hydraulic conductivity may strongly squeeze the range of redox zones as the wells of W08 and W09, while oppositely, the high hydraulic conductivity may extend it as W07. A similar result has been observed in an RBF site at the

Lot river, France (Kedziorek et al., 2008), where a distant well is more oxic than the near-bank well. For future research of the RBF site built on the heterogeneous geological condition, instead of studying a single cross-section along the flow direction, extra wells representing the heterogeneity should also be considered. This would be especially useful for RBF site planning. Taking our study site as an example, the safe setback distance would be underestimated by considering the redox condition of W08 and W09 only, where the treatment efficiency for nitrate and DOC is quite similar to the most distant well W04. However, along the flow path of W07, the shorter setback distance may not guarantee the full removal of nitrate. From another perspective, with a shorter setback distance, a larger contribution would be from the infiltrated water, and less pristine groundwater would be abstracted. Therefore, a better understanding of the local heterogeneity could help the planner to optimize the balance between the infiltration quantity and quality.

Calibration performance limited the model accuracy on reflecting the flow field and thermal field. It could be attributed to both 1) the insufficient or incomplete interpretation of the geological conditions and 2) the calibration accuracy. Heterogeneity brought great difficulty and uncertainty when considering the geological condition. Therefore, further detailed investigation would be required, especially in the area where the modelling result deviated largely from the observation. Autocalibration may also reach a better parameter composition for the model, however, due to the large calculation load, it could be applied only for the steady state model. Other simplifications and assumptions might also contribute to the inaccuracy in the model simulation. For example, considering the fixed groundwater recharge, or not considering the influence from the temperature on the viscosity, which would require another set of underlying equations and thus modelling environment. Pumping well settings in the model might also contribute to the possible error in calibration. As the current pumping rate distribution in a well is decided by the K_f-value of different layers, a clogging of the well screen may modify the real situation to show a different local flow field.

References

Abd Rashid, N.A., Roslan, M.H., Abd Rahim, N., Abustan, I., Adlan, M.N., 2015. Artificial barrier for riverbank filtration as improvment of soil permeability and water quality. J. Teknol. 74, 51–58.

Abdel-Lah, A.K., 2013. Riverbank Filtration for Water Supply in Semi Arid Environment. J. Eng. Sci. Assiut Univ. Fac. Eng. 41, 3, May, 2013 41, 840–850.

Abu-Hamdeh, N.H., 2003. Thermal properties of soils as affected by density and water content. Biosyst. Eng. 86, 97–102.

Anderson, M.P., 2005. Heat as a ground water tracer. Ground Water. 43, 951–968

Andreae, M.O., Schimel, D.S., Robertson, G.P., 1991. Exchange of trace gases between terrestrial ecosystems and the atmosphere. Plant Growth Regul. 10, 383–384.

Aravena, R., Robertson, W., 1998. USe of multiple isotope tracers to evaluate denitrification in groundwater; study of N from septic system plume. Ground Water. 36, 975-982

Archwichai, L., Saraphirom, P., Pholkern, K., Schäfer, S., Pavelic, P., Grischek, T., Wirojanagud, W., Srisuk, K., Soares, M., 2015. Riverbed clogging experiments at potential river bank filtration sites along the Ping River, Chiang Mai, Thailand. Environ. Earth Sci. 73, 7699–7709.

Ascott, M.J., Lapworth, D.J., Gooddy, D.C., Sage, R.C., Karapanos, I., 2016. Impacts of extreme flooding on riverbank filtration water quality. Sci. Total Environ. 554–555, 89–101.

Barcelona, M.J., Holm, T.R., 1991. Oxidation-reduction capacities of aquifer solids. Environ. Sci. Technol. 25, 1565–1572.

Barkow, I.S., Oswald, S.E., Lensing, H.J., Munz, M., 2020. Seasonal dynamics modifies fate of oxygen, nitrate, and organic micropollutants during bank filtration — temperature-dependent reactive transport modeling of field data. Environ Sci Pollut Res (2020). https://doi.org/10.1007/s11356-020-11002-9

Battin, T.J., Sengschmitt, D., 1999. Linking sediment biofilms, hydrodynamics, and river bed clogging: Evidence from a large river. Microb. Ecol. 37, 185–196.

Berger, P., 2002. Removal of Cryptosporidium Using Bank Filtration, in: Riverbank Filtration: Understanding Contaminant Biogeochemistry and Pathogen Removal. Springer Netherlands, Dordrecht, pp. 85–121.

Blavier, J., Verbanck, M.A., Craddock, F., Liégeois, S., Latinis, D., Gargouri, L., Flores Rua, G., Debaste, F., Haut, B., 2014. Investigation of riverbed filtration systems on the Parapeti river, Bolivia. J. Water Process Eng. 1, 27–36.

Böhlke, J.K., Smith, R.L., Miller, D.N., 2006. Ammonium transport and reaction in contaminated groundwater: Application of isotope tracers and isotope fractionation studies. Water Resour. Res. 42, 1–19.

Bourg, A.C.M., Bertin, C., 1994. Seasonal and Spatial Trends in Manganese Solubility in an Alluvial Aquifer. Environ. Sci. Technol. 28, 868–876.

Bourg, A.C.M., Bertin, C., 1993. Biogeochemical processes during the infiltration of river water into an alluvial aquifer. Environ. Sci. Technol. 27, 661–666.

Bourg, A.C.M., Darmendrail, D., Ricour, J., 1989. Geochemical filtration of riverbank and migration of heavy metals between the Deûle River and the Ansereuilles alluvion-chalk aquifer (Nord, France). Geoderma 44, 229–244.

Bouwer, H., 2002. Artificial recharge of groundwater: Hydrogeology and engineering. Hydrogeol. J. 10, 121–142.

Bradley, P.M., Barber, L.B., Duris, J.W., Foreman, W.T., Furlong, E.T., Hubbard, L.E., Hutchinson, K.J., Keefe, S.H., Kolpin, D.W., 2014. Riverbank filtration potential of pharmaceuticals in a wastewater-impacted stream. Environ. Pollut. 193, 173–180.

Bravo, H.R., Jiang, F., Hunt, R.J., 2002. Using groundwater temperature data to constrain parameter estimation in a groundwater flow model of a wetland system. Water Resour. Res. 38, 28-1-28–14.

Bretschko, G., Moser, H., 1993. Transport and retention of matter in riparian ecotones. Hydrobiologia 251, 95–101.

Brugger, A, Reitner, B., Kolar, I., Querec, N., Herndl, G.J., 2001. Seasonal and spatial distribution of dissolved and particulate organic carbon and bacteria in a bank of an oligotrophic river, the Enns River, Austria. Freshw. Biol. 46, 997–1016.

Brugger, Albert, Reitner, B., Kolar, I., Queric, N., Herndl, G.J., 2001. Seasonal and spatial distribution of dissolved and particulate organic carbon and bacteria in the bank of an impounding reservoir on the Enns River, Austria. Freshw. Biol. 46, 997–1016.

Brunet, R.C., Garcia-Gil, L.J., 1996. Sulfide-induced dissimilatory nitrate reduction to ammonia in anaerobic freshwater sediments. FEMS Microbiol. Ecol. 21, 131–138.

Burow, K.R., Constantz, J., Fujii, R., 2005. Heat as a tracer to estimate dissolved organic carbon flux from a restored wetland. Ground Water 43, 545–556.

Buss, S.R., Herbert, A.W., Morgan, P., Thornton, S.F., Smith, J.W.N., 2004. A review of ammonium attenuation in soil and groundwater. Q. J. Eng. Geol. Hydrogeol. 37, 347–359.

Cady, P., Boving, T.B., Choudri, B.S., Cording, A., Patil, K., Reddy, V., 2013. Attenuation of Bacteria at a Riverbank Filtration Site in Rural India. Water Environ. Res. 85, 2164–2174.

Casanova, J., Devau, N., Pettenati, M., 2016. Managed Aquifer Recharge: An Overview of Issues and Options, in: Jakeman, A.J., Barreteau, O., Hunt, R.J., Rinaudo, J.-D., Ross, A. (Eds.), Integrated Groundwater Management: Concepts, Approaches and Challenges. Springer International Publishing, Cham, pp. 413–434.

Ceazan, M.L., Thurman, E.M., Smith, R.L., 1989. Retardation of Ammonium and Potassium Transport Through a Contaminated Sand and Gravel Aquifer: The Role of Cation Exchange. Environ. Sci. Technol. 23, 1402–1408.

Champ, D.R., Gulens, J., Jackson, R.E., 1979. Oxidation–reduction sequences in ground water flow systems. Can. J. Earth Sci. 16, 12–23.

Chapelle, F.H., 2001. Ground-Water Microbiology and Geochemistry, 2nd ed. John Wiley and Sons, Inc.

Claret, C., 1998. Hyporheic biofilm development on artificial substrata, as a tool for assessing trophic status of aquatic systems: First results. Ann. Limnol. 34, 119–128.

Cleasby, J.L. (1990). "Filtration." Water quality and treatment, F.W. Pontius, ed., McGraw Hill, Inc., New York.

Colombani, N., Giambastiani, B.M.S., Mastrocicco, M., 2015. Combined use of heat and saline tracer to estimate aquifer properties in a forced gradient test. J. Hydrol. 525, 650–657.

Constantz, J., Stewart, A.E., Niswonger, R., Sarma, L., 2002. Analysis of temperature profiles for investigating stream losses beneath ephemeral channels. Water Resour. Res. 38, 52-1-52–13.

Constantz, J. (2008) 'Heat as a tracer to determine streambed water exchanges', Water Resources Research, 44(4). doi: 10.1029/2008WR006996.

Cox, M. H., Su, G. W. and Constantz, J. (2007) 'Heat, chloride, and specific conductance as ground water tracers near streams', Ground Water, 45(2), pp. 187–195. doi: 10.1111/j.1745-6584.2006.00276.x.

Cullen, T.R., Letterman, R.D., 1985. Effect of Slow Sand Filter Maintenance on Water Quality. J. / Am. Water Work. Assoc. 77, 48–55.

Cunningham, A.B., Anderson, C.J., Bouwer, H., 1987. Effects of Sediment-Laden Flow on Channel Bed Clogging. J. Irrig. Drain. Eng. 113, 106–118.

Dash, R.R., Bhanu Prakash, E.V.P., Kumar, P., Mehrotra, I., Sandhu, C., Grischek, T., 2010. River bank filtration in Haridwar, India: removal of turbidity, organics and bacteria. Hydrogeol. J. 18, 973–983.

Dash, R.R., Mehrotra, I., Kumar, P., Grischek, T., 2008. Lake bank filtration at Nainital, India: water-quality evaluation. Hydrogeol. J. 16, 1089–1099.

Delsman, J. R. et al. (2016) 'Global sampling to assess the value of diverse observations in conditioning a real-world groundwater flow and transport model', Water Resources Research, 52(3), pp. 1652–1672. doi: 10.1002/2014WR016476.

De Vet, W.W.J.M., Van Genuchten, C.C.A., Van Loosdrecht, M.C.M., Van Dijk, J.C., 2010. Water quality and treatment of river bank filtrate. Drink. Water Eng. Sci. 3, 79–90.

DeSimone, L.A., Howes, B.L., 1998. Nitrogen transport and transformations in a shallow aquifer receiving wastewater discharge: A mass balance approach. Water Resour. Res. 34, 271–285.

Diersch, H.-J.G., Kolditz, O., 2002. FEFLOW Reference Manual. DHI-Wasy, Berlin.

Dillon, P., Miller, M., Fallowfield, H., Hutson, J., 2002. The potential of riverbank filtration for drinking water supplies in relation to microsystin removal in brackish aquifers. J. Hydrol. 266, 209–221.

Dillon, P., 2005. Future management of aquifer recharge. Hydrogeol. J. 13, 313–316.

Dillon, P., Toze, S., Page, D., Vanderzalm, J., Bekele, E., Sidhu, J., Rinck-Pfeiffer, S., 2010. Managed aquifer recharge: rediscovering nature as a leading edge technology. Water Sci. Technol. 62, 2338–2345.

Döll, P., Müller Schmied, H., Schuh, C., Portmann, F.T., Eicker, A., 2014. Global-scale assessment of groundwater depletion and related groundwater abstractions: Combining hydrological modeling with information from well observations and GRACE satellites. Water Resour. Res. 50, 5698–5720.

Doettling, V., 2014. Numerische 3D-Grundwasserströmungsmodellierung im Bereich des Uferfiltratswasserwerks Potsdam-Nedlitz. (Numerical 3D groundwater flow modeling in the bank filtration water plant, Potsdam-Nedlitz). Master Thesis, Institute of Applied Geosciences, Karlsruhe Institute of Technology.

Doherty, J., 2015. Calibration and Uncertainty Analysis for Complex Environmental Models. Watermark Numerical Computing, Brisbane, Australia. ISBN: 978-0-9943786-0-6.

Domenico, P.A., Schwartz, F.W., 1998. Physical and Chemical Hydrogeology, 2nd ed. New York: John Wiley & Sons Inc.

Doussan, C., Ledoux, E., Detay, M., 1998. River-Groundwater Exchanges, Bank Filtration, and Groundwater Quality: Ammonium Behavior. J. Environ. Qual. 27, 1418.

Doussan, C., Poitevin, G., Ledoux, E., Delay, M., 1997. River bank filtration: Modelling of the changes in water chemistry with emphasis on nitrogen species. J. Contam. Hydrol. 25, 129–156.

Dragon, K., 2006. Application of factor analysis to study contamination of a semi-confined aquifer (Wielkopolska Buried Valley aquifer, Poland). J. Hydrol. 331, 272–279.

Drewes, J.E., Fox, P., 1999. Fate of natural organic matter (NOM) during groundwater recharge using reclaimed water. Water Sci. Technol. 40, 241–248.

Drewes, J.E., Heberer, T., Rauch, T., Reddersen, K., 2003. Fate of Pharmaceuticals During Ground Water Recharge. Groundw. Monit. Remediat. 23, 64–72.

Du, X., Fang, Y., Wang, Z., Hou, J., Ye, X., 2014. The prediction methods for potential suspended solids clogging types during managed aquifer recharge. Water (Switzerland) 6, 961–975.

Duque, C., Calvache, M.L., Engesgaard, P., 2010. Investigating river-aquifer relations using water temperature in an anthropized environment (Motril-Salobreña aquifer). J. Hydrol. 381, 121–133.

Engelhardt, I., Prommer, H., Schulz, M., Vanderborght, J., Schüth, C., Ternes, T.A., 2014. Reactive transport of iomeprol during stream-groundwater interactions. Environ. Sci. Technol. 48, 199–207.

Engesgaard, P., Seifert, D., Herrera, P., 2006. Bioclogging in Porous Media: Tracer Studies, in: Hubbs, S.A. (Ed.), Riverbank Filtration Hydrology. Springer Netherlands, Dordrecht, pp. 93–118.

Escalante EF, Calero R, de Borja González Herrarte F, Sauto JSS, del Pozo Campos E, Carvalho T (2015) MAR technical solutions: re- view and bata base. MARSOL

demonstrating managed aquifer re- charge as a solution to water scarcity and drought; MARSOL Deliverable 13-1; TRAGSA, Madrid, Spain

Escobar, I.C., Randall, A.A., 2001. Assimilable organic carbon (AOC) and biodegradable dissolved organic carbon (BDOC): Complementary measurements. Water Res. 35, 4444–4454.

Farnsworth, C.E., Hering, J.G., 2011. Inorganic geochemistry and redox dynamics in bank filtration settings. Environ. Sci. Technol. 45, 5079–5087.

Ferguson, G., Woodbury, A.D., 2005. The effects of climatic variability on estimates of recharge from temperature profiles. Ground Water 43, 837–842.

Fetter, C.W., 2001. Applied Hydrogeology. Appl. Hydrogeol. 4th edn. Prentice Hall, New Jersey.

Fetter, C.W., Boving, T., Kreamer, D., 2018. Contaminant Hydrogeology. Waveland Press, Inc.

Fiedler, C.J., Schönher, C., Proksch, P., Kerschbaumer, D.J., Mayr, E., Zunabovic-Pichler, M., Domig, K.J., Perfler, R., 2018. Assessment of microbial community dynamics in river bank filtrate using high-throughput sequencing and flow cytometry. Front. Microbiol. 9, 1–15.

Freeze, R.A., Cherry, J.A., 1979. Groundwater. Prentice-Hall, New Jersey.

Fukada, T., Hiscock, K.M., Dennis, P.F., Grischek, T., 2003. A dual isotope approach to identify denitrification in groundwater at a river-bank infiltration site. Water Res. 37, 3070–3078.

Ghodeif, K., Paufler, S., Grischek, T., Wahaab, R., Souaya, E., Bakr, M., Abogabal, A., 2018. Riverbank filtration in Cairo, Egypt—part I: installation of a new riverbank filtration site and first monitoring results. Environ. Earth Sci. 77, 270.

Giordano, M., 2009. Global Groundwater? Issues and Solutions. Annu. Rev. Environ. Resour. 34, 153–178.

Gleeson, T., Wada, Y., Bierkens, M.F.P., Van Beek, L.P.H., 2012. Water balance of global aquifers revealed by groundwater footprint. Nature 488, 197–200.

Goldschneider, A.A., Haralampides, K.A., MacQuarrie, K.T.B., 2007. River sediment and flow characteristics near a bank filtration water supply: Implications for riverbed clogging. J. Hydrol. 344, 55–69.

Gollnitz, W.D., Whitteberry, B.L., Vogt, J.A., 2004. Riverbank Filtration: Induced Infiltration and Groundwater Quality. J. Am. Water Works Assoc. 96, 98–110.

Grau-Martínez, A., Torrentó, C., Carrey, R., Rodríguez-Escales, P., Domènech, C., Ghiglieri, G., Soler, A., Otero, N., 2017. Feasibility of two low-cost organic substrates for inducing denitrification in artificial recharge ponds: Batch and flow-through experiments. J. Contam. Hydrol. 198, 48–58.

Greskowiak, J., Prommer, H., Massmann, G., Johnston, C.D., Nützmann, G., Pekdeger, A., 2005. The impact of variably saturated conditions on hydrogeochemical changes during artificial recharge of groundwater. Appl. Geochemistry 20, 1409–1426.

Grischek, T., Bartak, R., 2016. Riverbed Clogging and Sustainability of Riverbank Filtration. Water 8, 604.

Grischek, T., Hiscock, K.M., Metschies, T., Dennis, P.F., Nestler, W., 1998. Factors affecting denitrification during infiltration of river water into a sand and gravel aquifer in Saxony, Germany. Water Res. 32, 450-460.

Grischek, T., Paufler, S., 2017. Prediction of iron release during riverbank filtration. Water (Switzerland) 9, 317.

Groeschke, Maike, Frommen, T., Taute, T., Schneider, M., 2017. The impact of sewage-contaminated river water on groundwater ammonium and arsenic concentrations at a riverbank filtration site in central Delhi, India. Hydrogeol. J. 25, 2185–2197.

Groeschke, M., Frommen, T., Taute, T., Schneider, M., 2017. The impact of sewage-contaminated river water on groundwater ammoniumcasual connection and arsenic concentrations at a riverbank filtration site in central Delhi, India | L'impact d'une eau

fluviale contaminée par des eaux usées sur les concentrations en . Hydrogeol. J. 25, 2185–2197.
Gross-Wittke, A., Gunkel, G., Hoffmann, A., 2010. Temperature effects on bank filtration: Redox conditions and physical-chemical parameters of pore water at lake Tegel, Berlin, Germany. J. Water Clim. Chang. 1, 55–66.
Grünheid, S., Amy, G., Jekel, M., 2005. Removal of bulk dissolved organic carbon (DOC) and trace organic compounds by bank filtration and artificial recharge. Water Res. 39, 3219–3228.
Gupta, A., Ronghang, M., Kumar, P., Mehrotra, I., Kumar, S., Grischek, T., Sandhu, C., Knoeller, K., 2015. Nitrate contamination of riverbank filtrate at Srinagar, Uttarakhand, India: A case of geogenic mineralization. J. Hydrol. 531, 626–637.
Gupta, V., Johnson, W.P., Shafieian, P., Ryu, H., Alum, A., Abbaszadegan, M., Hubbs, S.A., Rauch-Williams, T., 2009. Riverbank Filtration: Comparison of Pilot Scale Transport with Theory. Environ. Sci. Technol. 43, 669–676.
Gutiérrez, J.P., van Halem, D., Uijttewaal, W.S.J., del Risco, E., Rietveld, L.C., 2018. Natural recovery of infiltration capacity in simulated bank filtration of highly turbid waters. Water Res. 147, 299–310.
Hamann, E., Stuyfzand, P.J., Greskowiak, J., Timmer, H., Massmann, G., 2016. The fate of organic micropollutants during long-term/long-distance river bank filtration. Sci. Total Environ. 545–546, 629–640.
Heberer, T., Mechlinski, A., Fanck, B., Knappe, A., Massmann, G., Pekdeger, A., Fritz, B., 2004. Field Studies on the Fate and Transport of Pharmaceutical Residues in Bank Filtration. Groundw. Monit. Remediat. 24, 70–77.
Hecht-Méndez, J., Molina-Giraldo, N., Blum, P., Bayer, P., 2010. Evaluating MT3DMS for heat transport simulation of closed geothermal systems. Ground Water 48, 741–756.
Henzler, A.F., Greskowiak, J., Massmann, G., 2016. Seasonality of temperatures and redox zonations during bank filtration – A modeling approach. J. Hydrol. 535, 282–292.
Henzler, A.F., Greskowiak, J., Massmann, G., 2014. Modeling the fate of organic micropollutants during river bank filtration (Berlin, Germany). J. Contam. Hydrol. 156, 78-92.
Heron, G., Christensen, T.H., Tjell, J.C., 1994. Oxidation Capacity of Aquifer Sediments. Environ. Sci. Technol. 28, 153–158.
Hiscock, K.M., 2005. Hydrogeology: Principles and Practice, Environmental and Engineering Geoscience. Blackwell, Oxford, UK.
Hiscock, K.M., Grischek, T., 2002. Attenuation of groundwater pollution by bank filtration. J. Hydrol. 266, 139–144.
Hoehn, E., Cirpka, O.A., 2006. Assessing hyporheic zone dynamics in two alluvial flood plains of the Southern Alps using water temperature and tracers. Hydrol. Earth Syst. Sci. Discuss. 3, 335–364.
Hoffmann, A., Gunkel, G., 2011. Bank filtration in the sandy littoral zone of Lake Tegel (Berlin): Structure and dynamics of the biological active filter zone and clogging processes. Limnologica 41, 10–19.
Holley, C., Sinclair, D., Lopez-Gunn, E., Schlager, E., 2016. Conjunctive Management Through Collective Action, in: Jakeman, A.J., Barreteau, O., Hunt, R.J., Rinaudo, J.-D., Ross, A. (Eds.), Integrated Groundwater Management: Concepts, Approaches and Challenges. Springer International Publishing, Cham, pp. 229–252.
Hölting, B., Coldewey, W.G., 2013. Hydrogeologie. Spektrum Akademischer Verlag, Heidelberg.
Hoppe-Jones, C., Oldham, G., Drewes, J.E., 2010. Attenuation of total organic carbon and unregulated trace organic chemicals in U.S. riverbank filtration systems. Water Res. 44, 4643–4659.
Hu, B., Teng, Y., Zhai, Y., Zuo, R., Li, J., Chen, H., 2016. Riverbank filtration in China: A review and perspective. J. Hydrol. 541, 914–927.

Hua, G., Reckhow, D.A., Abusallout, I., 2015. Correlation between SUVA and DBP formation during chlorination and chloramination of NOM fractions from different sources. Chemosphere 130, 82–89.
Hunt, R.J., Coplen, T.B., Haas, N.L., Saad, D.A., Borchardt, M.A., 2005. Investigating surface water-well interaction using stable isotope ratios of water. J. Hydrol. 302, 154–172.
Jacobs, L.A., von Gunten, H.R., Keil, R., Kuslys, M., 1988. Geochemical changes along a river-groundwater infiltration flow path: Glattfelden, Switzerland. Geochim. Cosmochim. Acta 52, 2693–2706.
Jekel, M., Gruenheid, S., 2005. Bank filtration and groundwater recharge for treatment of polluted surface waters. Water Sci. Technol. Water Supply 5, 57–66.
Kalbus, E., Reinstorf, F., Schirmer, M., 2006. Measuring methods for groundwater – surface water interactions: a review. Hydrol. Earth Syst. Sci 10, 873–887.
Karan, S., Engesgaard, P., Rasmussen, J., 2014. Dynamic streambed fluxes during rainfall-runoff events. Water Resour. Res. 50, 2293–2311.
Kedziorek, M.A.M., Bourg, A.C.M., 2009. Electron trapping capacity of dissolved oxygen and nitrate to evaluate Mn and Fe reductive dissolution in alluvial aquifers during riverbank filtration. J. Hydrol. 365, 74–78.
Kedziorek, M.A.M., Geoffriau, S., Bourg, A.C.M., 2008. Organic matter and modeling redox reactions during river bank filtration in an alluvial aquifer of the Lot River, France. Environ. Sci. Technol. 42, 2793-2798.
Keery, J., Binley, A., Crook, N., Smith, J.W.N., 2007. Temporal and spatial variability of groundwater-surface water fluxes: Development and application of an analytical method using temperature time series. J. Hydrol. 336, 1–16.
Keswick, B.H., Gerba, C.P., 1980. Viruses in groundwater. Environ. Sci. Technol. 14, 1290–1297.
Koch, F.W., Voytek, E.B., Day-Lewis, F.D., Healy, R., Briggs, M.A., Lane, J.W., Werkema, D., 2016. 1DTempPro V2: New Features for Inferring Groundwater/Surface-Water Exchange. Groundwater 54, 434–439.
Kohfahl, C., Massmann, G., Pekdeger, A., 2009. Sources of oxygen flux in groundwater during induced bank filtration at a site in Berlin, Germany. Hydrogeol. J. 17, 571–578.
Kohfahl, C., Massmann, G., Pekdeger, A., 2008. Sources of oxygen flux in groundwater during induced bank filtration at a site in Berlin, Germany. Hydrogeol. J. 17, 571–578.
Korom, S.F., 1992. Natural denitrification in the saturated zone: A review. Water Resour. Res. 28, 1657–1668.
Kovačević, S., Radišić, M., Laušević, M., Dimkić, M., 2017. Occurrence and behavior of selected pharmaceuticals during riverbank filtration in The Republic of Serbia. Environ. Sci. Pollut. Res. 24, 2075–2088.
Krauskopf, K.B. & Bird, D.K. (1995) Introduction to Geo- chemistry, 3rd edn. McGraw-Hill, New York.
Kuehn, W., 2000. Riverbank filtration: an overview. Journal of the American Water Works Association 92, 60.
Kundzewicz, Z.W., Döll, P., 2009. Will groundwater ease freshwater stress under climate change? Hydrol. Sci. J. 54, 665–675.
Kwon, D.-Y., 2015a. Study on water quality improvement by bank filtration. Desalin. Water Treat. 54, 1385–1392.
Kwon, D.-Y., 2015b. Study on water quality improvement by bank filtration. Desalin. Water Treat. 54, 1385–1392.
Lee, J.-H., Hamm, S.-Y., Cheong, J.-Y., Kim, H.-S., Ko, E.-J., Lee, K.-S., Lee, S.-I., 2009. Characterizing riverbank-filtered water and river water qualities at a site in the lower Nakdong River basin, Republic of Korea. J. Hydrol. 376, 209–220.
Lee, Sang-il, Lee, Sang-sin, 2010. Development of site suitability analysis system for riverbank filtration. Water Sci. Eng. 3, 85–94.

Leenheer, J.A., Croué, J.-P., 2003. Peer Reviewed: Characterizing Aquatic Dissolved Organic Matter. Environ. Sci. Technol. 37, 18A-26A.

Levy, J., Birck, M.D., Mutiti, S., Kilroy, K.C., Windeler, B., Idris, O., Allen, L.N., 2011. The impact of storm events on a riverbed system and its hydraulic conductivity at a site of induced infiltration. J. Environ. Manage. 92, 1960–1971.

Li, C., Li, B., Bi, E., 2019. Characteristics of hydrochemistry and nitrogen behavior under long-term managed aquifer recharge with reclaimed water: A case study in north China. Sci. Total Environ. 668, 1030–1037.

Liao, Z., Osenbrück, K., Cirpka, O.A., 2014. Non-stationary nonparametric inference of river-to-groundwater travel-time distributions. J. Hydrol. 519, 3386–3399.

Livingston, A., 2009. Towards Pragmatic Action for Addressing Groundwater Overexploitation in India. World Bank.

Löffler, D., Römbke, J., Meller, M., Ternes, T.A., 2005. Environmental fate of pharmaceuticals in water/sediment systems. Environ. Sci. Technol. 39, 5209–5218.

Luce, C.H., Tonina, D., Gariglio, F., Applebee, R., 2013. Solutions for the diurnally forced advection-diffusion equation to estimate bulk fluid velocity and diffusivity in streambeds from temperature time series. Water Resour. Res. 49, 488–506.

Ludwig, U., Grischek, T., Nestler, W., Neumann, V., 1997. Behaviour of different molecular-weight fractions of DOC of Elbe river water during river bank infiltration. Acta Hydrochim. Hydrobiol. 25, 145–150.

Maeng, S.K., Ameda, E., Sharma, S.K., Grützmacher, G., Amy, G.L., 2010. Organic micropollutant removal from wastewater effluent-impacted drinking water sources during bank filtration and artificial recharge. Water Res. 44, 4003-4014.

Mahinthakumar, G. K., Moline, G. R. and Webb, O. F. (2005) 'An analysis of periodic tracers for subsurface characterization', Water Resources Research, 41(12), 1–13. doi: 10.1029/2005WR004190.

Mallen, G., Geyer, S., Trettin, R., Strauch, G., Gehre, M., Grischek, T., 1998. Contribution from carbon and sulphur isotopes to the evaluation of biogeochemical processes in groundwater systems controlled by river bank filtration: An example from the Torgau aquifer (Saxony, Germany). IAEA, International Atomic Energy Agency (IAEA).

Masbruch, M.D., Gardner, P.M., Brooks, L.E., n.d. Hydrology and Numerical Simulation of Groundwater Movement and Heat Transport in Snake Valley and Surrounding Areas, Juab, Millard, and Beaver Counties, Utah, and White Pine and Lincoln Counties, Nevada.

Massmann, G., Greskowiak, J., Dünnbier, U., Zuehlke, S., Knappe, A., Pekdeger, A., 2006. The impact of variable temperatures on the redox conditions and the behaviour of pharmaceutical residues during artificial recharge. J. Hydrol. 328, 141–156.

Massmann, G., Nogeitzig, A., Taute, T., Pekdeger, A., 2008a. Seasonal and spatial distribution of redox zones during lake bank filtration in Berlin, Germany. Environ. Geol. 54, 53–65.

Massmann, G., Pekdeger, A., Merz, C., 2004. Redox processes in the Oderbruch polder groundwater flow system in Germany. Appl. Geochemistry 19, 863–886.

Massmann, G., Sültenfuß, J., Dünnbier, U., Knappe, A., Taute, T., Pekdeger, A., 2008b. Investigation of groundwater residence times during bank filtration in Berlin: a multi-tracer approach. Hydrol. Process. 22, 788–801.

Massmann, G., Tichomirowa, M., Merz, C., Pekdeger, A., 2003a. Sulfide oxidation and sulfate reduction in a shallow groundwater system (Oderbruch Aquifer, Germany). J. Hydrol. 278, 231–243.

Massmann, G., Tichomirowa, M., Merz, C., Pekdeger, A., 2003b. Sulfide oxidation and sulfate reduction in a shallow groundwater system (Oderbruch Aquifer, Germany). J. Hydrol. 278, 231–243.

Mastrocicco, M., Colombani, N., Castaldelli, G., Jovanovic, N., 2011. Monitoring and modeling nitrate persistence in a shallow aquifer. Water. Air. Soil Pollut. 217, 83–93.

McBratney, A.B., Minasny, B., Cattle, S.R., Vervoort, R.W., 2002. From pedotransfer functions to soil inference systems. Geoderma 109, 41–73.
Miettinen, I.T., Martikainen, P.J., Vartianinen, T., 1994. Humus transformation at the bank filtration water plant, in: Water Science and Technology. pp. 179–187.
Miettinen, I.T., Vartiainen, T., Martikainen, P.J., 1996. Bacterial enzyme activities in ground water during bank filtration of lake water. Water Res. 30, 2495–2501.
Munz, M., Oswald, S.E., Schäfferling, R., Lensing, H.J., 2019. Temperature-dependent redox zonation, nitrate removal and attenuation of organic micropollutants during bank filtration. Water Res. 162, 225–235.
Munz, M., Oswald, S.E., Schmidt, C., 2017. Coupled Long-Term Simulation of Reach-Scale Water and Heat Fluxes Across the River-Groundwater Interface for Retrieving Hyporheic Residence Times and Temperature Dynamics. Water Resour. Res. 53, 8900–8924.
Munz, M., Oswald, S.E., Schmidt, C., 2016. Analysis of riverbed temperatures to determine the geometry of subsurface water flow around in-stream geomorphological structures. J. Hydrol. 539, 74–87.
Munz, M., Schmidt, C., 2017. Estimation of vertical water fluxes from temperature time series by the inverse numerical computer program FLUX-BOT. Hydrol. Process. 31, 2713–2724.
Mustafa, S., Bahar, A., Aziz, Z.A., Suratman, S., 2016. Modelling contaminant transport for pumping wells in riverbank filtration systems. J. Environ. Manage. 165, 159–166.
Mutiti, S., Levy, J., 2010. Using temperature modeling to investigate the temporal variability of riverbed hydraulic conductivity during storm events. J. Hydrol. 388, 321–334.
NASA's Land Processes Distributed Active Archive Center (LP DAAC) (2019) The ASTER global digital elevation model (GDEM) version 3(ASTGTM). https://doi.org/10.5067/ASTER/ASTGTM.003
Nützmann, G., Levers, C., Lewandowski, J., 2014. Coupled groundwater flow and heat transport simulation for estimating transient aquifer-stream exchange at the lowland River Spree (Germany). Hydrol. Process. 28, 4078–4090.
Odling, N.E., Perulero Serrano, R., Hussein, M.E.A., Riva, M., Guadagnini, A., 2015. Detecting the vulnerability of groundwater in semi-confined aquifers using barometric response functions. J. Hydrol. 520, 143–156.
Ojha, C.S.P., Thakur, A.K., Singh, V.P., 2013. Modelling of River Bank Filtration : Experience from RBF site in India 2, 46–55.
Oren, O., Gavrieli, I., Burg, A., Guttman, J., Lazar, B., 2007. Manganese mobilization and enrichment during soil aquifer treatment (SAT) of effluents, the Dan Region Sewage Reclamation Project (Shafdan), Israel. Environ. Sci. Technol. 41, 766–772.
Othman, S.Z., Adlan, M.N., Selamat, M.R., 2015. A study on the potential of riverbank filtration for the removal of color, iron, turbidity and E.Coli in Sungai Perak, Kota Lama Kiri, Kuala Kangsar, Perak, Malaysia. J. Teknol. 74, 89–95.
Pan, W., Huang, Q., Huang, G., 2018. Nitrogen and organics removal during riverbank filtration along a reclaimed water restored river in Beijing, China. Water (Switzerland) 9, 786.
Paufler, S., Grischek, T., Bartak, R., Ghodeif, K., Wahaab, R., Boernick, H., 2018. Riverbank filtration in Cairo, Egypt: part II—detailed investigation of a new riverbank filtration site with a focus on manganese. Environ. Earth Sci. 77, 318.
Pavelic, P., Dillon, P.J., Mucha, M., Nakai, T., Barry, K.E., Bestland, E., 2011. Laboratory assessment of factors affecting soil clogging of soil aquifer treatment systems. Water Res. 45, 3153–3163.
Piper, A.M., 1944. A graphic procedure in the geochemical interpretation of water - analyses. Eos, Trans. Am. Geophys. Union 25, 914–928.
Polomčić, D., Hajdin, B., Stevanović, Z., Bajić, D., Hajdin, K., 2013. Groundwater management by riverbank filtration and an infiltration channel: the case of Obrenovac,

Serbia. Hydrogeol. J. 21, 1519-1530.
Prommer, H., Stuyfzand, P.J., 2005. Identification of temperature-dependent water quality changes during a deep well injection experiment in a pyritic aquifer. Environ. Sci. Technol. 39, 2200–2209.
Ragusa, S.R., de Zoysa, D.S., Rengasamy, P., 1994. The effect of microorganisms, salinity and turbidity on hydraulic conductivity of irrigation channel soil. Irrig. Sci. 15, 159–166.
Rau, G.C., Andersen, M.S., McCallum, A.M., Roshan, H., Acworth, R.I., 2014. Heat as a tracer to quantify water flow in near-surface sediments. Earth-Science Rev. 129, 40–58.
Ray, C., 2008. Worldwide potential of riverbank filtration. Clean Technol. Environ. Policy 10, 223–225.
Ray, C., 2004. Modeling RBF Efficacy for Mitigating Chemical Shock Loads. J. Am. Water Works Assoc. 96, 114–128.
Ray, C. (Ed.), 2002a. Riverbank Filtration: Understanding Contaminant Biogeochemistry and Pathogen Removal. Springer Netherlands, Dordrecht.
Ray, C., 2002b. Effect of Biogeochemical, Hydrogeological, and Well Construction Factors on Riverbank Filtrate Quality, in: Ray, C. (Ed.), Riverbank Filtration: Understanding Contaminant Biogeochemistry and Pathogen Removal. Springer Netherlands, Dordrecht, pp. 1–16.
Ray, C., Grischek, T., Schubert, J., Wang, J.Z., Speth, T.F., 2002a. A Perspective of Riverbank Filtration. J. Am. Water Works Assoc. 94, 149–160.
Ray, C., Melin, G., Linksy, R.B., 2003. Riverbank Filtration Improving Source-water Quality, Environmental Science and Engineering (Subseries: Environmental Science), Water Science and Technology Library. Kluwer Academic Publishers, Dordrecht.
Ray, C., Soong, T., Lian, Y., Roadcap, G., 2002b. Effect of flood-induced chemical load on filtrate quality at bank filtration sites. J. Hydrol. 266, 235–258.
Reeves, J., Hatch, C.E., 2016. Impacts of three-dimensional nonuniform flow on quantification of groundwater-surface water interactions using heat as a tracer. Water Resour. Res. 52, 6851–6866.
Regnery, J., Barringer, J., Wing, A.D., Hoppe-Jones, C., Teerlink, J., Drewes, J.E., 2015. Start-up performance of a full-scale riverbank filtration site regarding removal of DOC, nutrients, and trace organic chemicals. Chemosphere 127, 136–142.
Richardson, S.D., Plewa, M.J., Wagner, E.D., Schoeny, R., DeMarini, D.M., 2007. Occurrence, genotoxicity, and carcinogenicity of regulated and emerging disinfection by-products in drinking water: A review and roadmap for research. Mutat. Res. - Rev. Mutat. Res. 636, 178–242.
Robert A. Berner, 1981. A New Geochemical Classification of Sedimentary Environments. SEPM J. Sediment. Res. 51, 359–365.
Romero-Esquivel, L.G., Grischek, T., Pizzolatti, B.S., Mondardo, R.I., Sens, M.L., 2017. Bank filtration in a coastal lake in South Brazil: water quality, natural organic matter (NOM) and redox conditions study. Clean Technol. Environ. Policy 19, 2007–2020.
Romero, L.G., Mondardo, R.I., Sens, M.L., Grischek, T., 2014. Removal of cyanobacteria and cyanotoxins during lake bank filtration at Lagoa do Peri, Brazil. Clean Technol. Environ. Policy 16, 1133–1143.
Ronan, A.D., Prudic, D.E., Thodal, C.E., Constantz, J., 1998. Field study and simulation of diurnal temperature effects on infiltration and variably saturated flow beneath an ephemeral stream. Water Resour. Res. 34, 2137–2153.
Sabater, S., Romaní, A.M., 1996. Metabolic changes associated with biofilm formation in an undisturbed Mediterranean stream. Hydrobiologia 335, 107–113.
Sandhu, C., Grischek, T., Börnick, H., Feller, J., Sharma, S.K., 2019. A water quality appraisal of some existing and potential riverbank filtration sites in India. Water (Switzerland) 11, 1–17.
Sandhu, C., Grischek, T., Kumar, P., Ray, C., 2011a. Potential for Riverbank filtration in India. Clean Technol. Environ. Policy 13, 295–316.

Sandhu, C., Grischek, T., Schoenheinz, D., Prasad, T., Thakur, A.K., 2011b. Evaluation of Bank Filtration for Drinking Water Supply in Patna by the Ganga River, India, in: NATO Science for Peace and Security Series C: Environmental Security. pp. 203–222.
Schälchli, U., 1992. The clogging of coarse gravel river beds by fine sediment. Hydrobiologia 235–236, 189–197.
Schiff, L., Johnson, C.E., 1958. Some methods of alleviating surface clogging in water spreading with emphasis on filters. Eos, Trans. Am. Geophys. Union 39, 292–297.
Schijven, J., Berger, P., Miettinen, I., 2003. Removal of Pathogens, Surrogates, Indicators, and Toxins Using Riverbank Filtration, in: Ray, C., Melin, G., Linsky, R.B. (Eds.), Riverbank Filtration: Improving Source-Water Quality. Springer Netherlands, Dordrecht, pp. 73–116.
Schijven, J.F., 2002. Virus Removal by Soil Passage at Field Scale and Groundwater Protection, in: Ray, C. (Ed.), Riverbank Filtration: Understanding Contaminant Biogeochemistry and Pathogen Removal. Springer Netherlands, Dordrecht, pp. 55–84.
Schijven, J.F., Hassanizadeh, S.M., 2000. Removal of Viruses by Soil Passage: Overview of Modeling, Processes, and Parameters. Crit. Rev. Environ. Sci. Technol. 30, 49–127.
Schubert, J., 2006. Significance of Hydrologic Aspects on RBF Performance, in: Hubbs, S.A. (Ed.), Riverbank Filtration Hydrology. Springer Netherlands, Dordrecht, pp. 1–20.
Schubert, J., 2002. Hydraulic aspects of riverbank filtration—field studies. J. Hydrol. 266, 145–161.
Schubert, J., 1992. Sicherheit der Trinkwassergewinnung aus Uferfiltrat bei Stoßbelastungen. Abschlussbericht des Teilprojekts 3 zum BMFT-Verbundvorhaben 02-WT88141. Stadtwerke Düsseldorf.
Seibert, S., Prommer, H., Siade, A., Harris, B., Trefry, M., Martin, M., 2014. Heat and mass transport during a groundwater replenishment trial in a highly heterogeneous aquifer. Water Resour. Res. 50, 9463–9483.
Seyed Jalali, S.A., Navidi, M.N., Seyed Mohammadi, J., Meymand, A.Z., Mohammad Esmail, Z., 2019. Prediction of Soil Cation Exchange Capacity Using Different Soil Parameters by Intelligent Models. Commun. Soil Sci. Plant Anal. 50, 2123–2139.
Shamrukh, M., Abdel-Wahab, A., 2011. Water pollution and Riverbank filtration for water supply along River Nile, Egypt. NATO Sci. Peace Secur. Ser. C Environ. Secur. 103, 5–28.
Shamrukh, M., Abdel-Wahab, A., 2008. Riverbank filtration for sustainable water supply: application to a large-scale facility on the Nile River. Clean Technol. Environ. Policy 10, 351–358.
Shamsuddin, M.K.N., Sulaiman, W.N.A., Suratman, S., Zakaria, M.P., Samuding, K., 2014. Groundwater and surface-water utilisation using a bank infiltration technique in Malaysia. Hydrogeol. J. 22, 543–564.
Sharma, B., Uniyal, D.P., Dobhal, R., Kimothi, P.C., Grischek, T., 2014. A sustainable solution for safe drinking water through bank filtration technology in Uttarakhand, India. Curr. Sci. 107, 1118–1124.
Sharma, L., Greskowiak, J., Ray, C., Eckert, P., Prommer, H., 2012. Elucidating temperature effects on seasonal variations of biogeochemical turnover rates during riverbank filtration. J. Hydrol. 428–429, 104–115.
Sharma, S.K., Amy, G., 2009. Bank filtration : A sustainable water treatment technology for developing countries. 34th WEDC Int. Conf. 715.
Shaw, G.D., White, E.S., Gammons, C.H., 2013. Characterizing groundwater-lake interactions and its impact on lake water quality. J. Hydrol. 492, 69–78.
Sheets, R., Darner, R.., Whitteberry, B.., 2002. Lag times of bank filtration at a well field, Cincinnati, Ohio, USA. J. Hydrol. 266, 162–174.
Singer, P.C., 1999. Humic substances as precursors for potentially harmfuacl disinfection by-products. Water Sci. Technol. 40, 25–30.
Singh, P., Kumar, P., Mehrotra, I., Grischek, T., 2010. Impact of riverbank filtration on

treatment of polluted river water. J. Environ. Manage. 91, 1055–1062.
Sontheimer, H., 1980. Experience with riverbank filtration along the Rhine river. J. Am. Waterworks Assoc. 72, 386–390.
Sontheimer, H., 1991. Trinkwasser aus dem Rhein?: Bericht ueber ein vom Bundsminister fuer Forschung und Technologie gefoerdertes Verbundforschungsvorhaben zur Sicherheit der Trinkwassergewinnung aus Rheinuferfiltrat bei Stossbelastungen, Academia Verlag, St. Augustin.
Srisuk, K., Archwichai, L., Pholkern, K., Saraphirom, P., Chusanatus, S., Munyou, S., 2012. Groundwater Resources Development by Riverbank Filtration Technology in Thailand. Int. J. Environ. Rural Dev. 3, 155–161.
Stallman, R.W., 1965. Steady one-dimensional fluid flow in a semi-infinite porous medium with sinusoidal surface temperature. J. Geophys. Res. 70, 2821–2827.
Stepien, D.K., Regnery, J., Merz, C., Püttmann, W., 2013. Behavior of organophosphates and hydrophilic ethers during bank filtration and their potential application as organic tracers. A field study from the Oderbruch, Germany. Sci. Total Environ. 458–460, 150–159.
Stonestrom, D.A., Constantz, J., 2003. Heat as a tool for studying the movement of ground water near streams, U.S. Geological Survey Circular 1260.
Stonestrom, D.A., and K.W. Blasch. 2003. Determining temperature and thermal properties for heat-based studies of surface-water ground-water interactions. U. S. Geol. Surv. 73-80.
Storey, R.G., Fulthorpe, R.R., Williams, D.D., 1999. Perspectives and predictions on the microbial ecology of the hyporheic zone. Freshw. Biol. 41, 119–130.
Strock, J.S., 2008. Ammonification. Encycl. Ecol. 162–165.
Su, X., Lu, S., Gao, R., Su, D., Yuan, W., Dai, Z., Papavasilopoulos, E.N., 2017. Groundwater flow path determination during riverbank filtration affected by groundwater exploitation: a case study of Liao River, Northeast China. Hydrol. Sci. J. 62, 2331-2347
Su, X., Lu, S., Yuan, W., Woo, N.C., Dai, Z., Dong, W., Du, S., Zhang, X., 2018b. Redox zonation for different groundwater flow paths during bank filtration: a case study at Liao River, Shenyang, northeastern China. Hydrogeol. J. 26, 1573–1589.
Suzuki, S., 2008. Percolation measurements based on heat flow through soil with special reference to paddy fields. J. Geophys. Res. 65, 2883–2885.
Taylor, S.W., Jaffé, P.R., 1990. Biofilm growth and the related changes in the physical properties of a porous medium: 3. Dispersivity and model verification. Water Resour. Res. 26, 2171–2180.
The Council of the European Union, 1998. Council Directive 98/83/EC of 3 November 1998 on the quality of water intended for human consumption. Official Journal of the European Communities doi:2004R0726-v.7.of.05.06.2013.
The Council of the European Union, 2000. Directive 2000/60/EC of the European Parliament and of the Council of 23 October 2000 establishing a framework for Community action in the field of water policy. Official Journal of the European Parliament. https://doi.org/10.1039/ap9842100196.
Thullner, M., Zeyer, J., Kinzelbach, W., 2002. Influence of microbial growth on hydraulic properties of pore networks. Transp. Porous Media 49, 99–122.
Todd, D.K., Mays, L.W., 2005. Groundwater hydrology. New York: Wiley.
Tufenkji, N., Ryan, J.N., Elimelech, M., 2002. Peer Reviewed: The Promise of Bank Filtration. Environ. Sci. Technol. 36, 422A-428A.
Tuinhof, A., Heederik, J.P., 2002. Management of Aquifer Recharge and Subsurface Storage Seminar. Making Better use of Our Largest Reservoir, Management of Aquifer Recharge and Subsurface Storage Seminar.
Ulrich, C., Hubbard, S.S., Florsheim, J., Rosenberry, D., Borglin, S., Trotta, M., Seymour, D., 2015. Riverbed Clogging Associated with a California Riverbank Filtration System: An Assessment of Mechanisms and Monitoring Approaches. J. Hydrol. 529, 1740–1753.

Umar, D.A., Ramli, M.F., Aris, A.Z., Sulaiman, W.N.A., Kura, N.U., Tukur, A.I., 2017. An overview assessment of the effectiveness and global popularity of some methods used in measuring riverbank filtration. J. Hydrol.550, 497-515.

Environmental Protection Agency (1992) Consensus Method for Determining Groundwaters Under the Direct Influence of Surface Water Using Microscopic Particulate Analysis (MPA), EPA 9009-92- 029, Washington, D.C

U.S. Environmental Protection Agency (1998) National Primary Drinking Water Regulations. Interim Enhanced Surface Water Treatment Rule (IESWTR). Fed Reg. 63: 69478.

Van De Graaf, A.A., De Bruijn, P., Robertson, L.A., Jetten, M.S.M., Kuenen, J.G., 1997. Metabolic pathway of anaerobic ammonium oxidation on the basis of 15N studies in a fluidized bed reactor. Microbiology 143, 2415–2421.

van Driezum, I.H., Chik, A.H.S., Jakwerth, S., Lindner, G., Farnleitner, A.H., Sommer, R., Blaschke, A.P., Kirschner, A.K.T., 2018. Spatiotemporal analysis of bacterial biomass and activity to understand surface and groundwater interactions in a highly dynamic riverbank filtration system. Sci. Total Environ. 627, 450–461.

van Driezum, I.H., Derx, J., Oudega, T.J., Zessner, M., Naus, F.L., Saracevic, E., Kirschner, A.K.T., Sommer, R., Farnleitner, A.H., Blaschke, A.P., 2019. Spatiotemporal resolved sampling for the interpretation of micropollutant removal during riverbank filtration. Sci. Total Environ. 649, 212–223.

Vandenbohede, A., Van Houtte, E., 2012. Heat transport and temperature distribution during managed artificial recharge with surface ponds. J. Hydrol. 472–473, 77–89.

Vandenbohede, A., Van Houtte, E., Lebbe, L., 2008. Groundwater flow in the vicinity of two artificial recharge ponds in the Belgian coastal dunes. Hydrogeol. J. 16, 1669–1681.

Vandevivere, P., Baveye, P., 1992. Saturated Hydraulic Conductivity Reduction Caused by Aerobic Bacteria in Sand Columns. Soil Sci. Soc. Am. J. 56, 1.

VDI 4640/1, 2010. VDI 4640-Thermal Use of Underground, Blatt 1: Fundamentals, Approvals, Environmental Aspects. Verein Deutscher Ingenieure, Düsseldorf, Germany.

Vogt, T., Hoehn, E., Schneider, P., Cirpka, O.A., 2009. Untersuchung der Flusswasserinfiltration in voralpinen Schottern mittels ZeitreihenanalyseInvestigation of bank filtration in gravel and sand aquifers using time-series analysis. Grundwasser 14, 179–194.

Wada, Y., Van Beek, L.P.H., Van Kempen, C.M., Reckman, J.W.T.M., Vasak, S., Bierkens, M.F.P., 2010. Global depletion of groundwater resources. Geophys. Res. Lett. 37, 1–5.

Wang, C., Wang, P.F., Hu, X., 2007. Removal of CODCr and nitrogen in severely polluted river water by bank filtration. Environ. Technol. 28, 649–657.

Wang, L., Ye, X., Du, X., 2016. Suitability Evaluation of River Bank Filtration along the Second Songhua River, China. Water 8, 176.

Wang, W., Oswald, S.E., Gräff, T., Lensing, H.-J., Liu, T., Strasser, D., Munz, M., 2019. Impact of river reconstruction on groundwater flow during bank filtration assessed by transient three-dimensional modelling of flow and heat transport. Hydrogeol. J. https:\\dx.doi.org/10.1007/s10040-019-02104-x

Weishaar, J.L., Fram, M.S., Fujii, R., Mopper, K., 2003. Evaluation of Specific Ultraviolet Absorbance as an Indicator of the Chemical Composition and Reactivity of Dissolved Organic Carbon 37, 4702–4708.

Weiss, W.J., Bouwer, E.J., Aboytes, R., LeChevallier, M.W., O'Melia, C.R., Le, B.T., Schwab, K.J., 2005. Riverbank filtration for control of microorganisms: Results from field monitoring. Water Res. 39, 1990–2001.

Wett, B., 2006. Monitoring Clogging of a RBF-System at the River Enns, Austria, in: Hubbs, S.A. (Ed.), Riverbank Filtration Hydrology. Springer Netherlands, Dordrecht, pp. 259–280.

Wett, B., Jarosch, H., Ingerle, K., 2002. Flood induced infiltration affecting a bank filtrate well at the River Enns, Austria. J. Hydrol. 266, 222–234.

Wilcoxon, F., 1945. Individual Comparisons by Ranking Methods. Biometrics Bull. 1, 80.

Wilderer, P.A., Förstner, U., Kuntschik, O.R., 2013. The Role of Riverbank Filtration along the Rhine River for Municipal and Industrial Water Supply. Artif. Recharg. Groundw. 509–528.

Winston, R.B., 2000. Graphical User Interface for MODFLOW , Version 4: Open-File Report 00-315 34.

World Health Organization (WHO), 2003. Ammonia in Drinking-water. Heal. San Fr. 2, http://www.who.int/water_sanitation_health/dwq/che.

Wu, Y., Hui, L., Wang, H., Li, Y., Zeng, R., 2007. Effectiveness of riverbank filtration for removal of nitrogen from heavily polluted rivers: A case study of Kuihe River, Xuzhou, Jiangsu, China. Environ. Geol. 52, 19–25.

Xie, Y., Cook, P.G., Shanafield, M., Simmons, C.T., Zheng, C., 2016. Uncertainty of natural tracer methods for quantifying river-aquifer interaction in a large river. J. Hydrol. 535, 135–147.

Zamora, C.M., Essaid, H.I., McCarthy, K.A., Wilson, J.T., Vogel, J.R., 2008. Using Heat to Characterize Streambed Water Flux Variability in Four Stream Reaches. J. Environ. Qual. 37, 1010.

Zhang, Y., Hubbard, S., Finsterle, S., 2011. Factors Governing Sustainable Groundwater Pumping near a River. Ground Water 49, 432–444.

Zheng, W., Lichwa, J., D'Alessio, M., Ray, C., 2009. Fate and transport of TNT, RDX, and HMX in streambed sediments: Implications for riverbank filtration. Chemosphere 76, 1167–1177.

Appendix

Figure. S1 Model cross-section of aquifer vs. glacial till layers in transects (a) U100-W03-W04, (b) canal bank-W07 and (c) canal bank-W09.

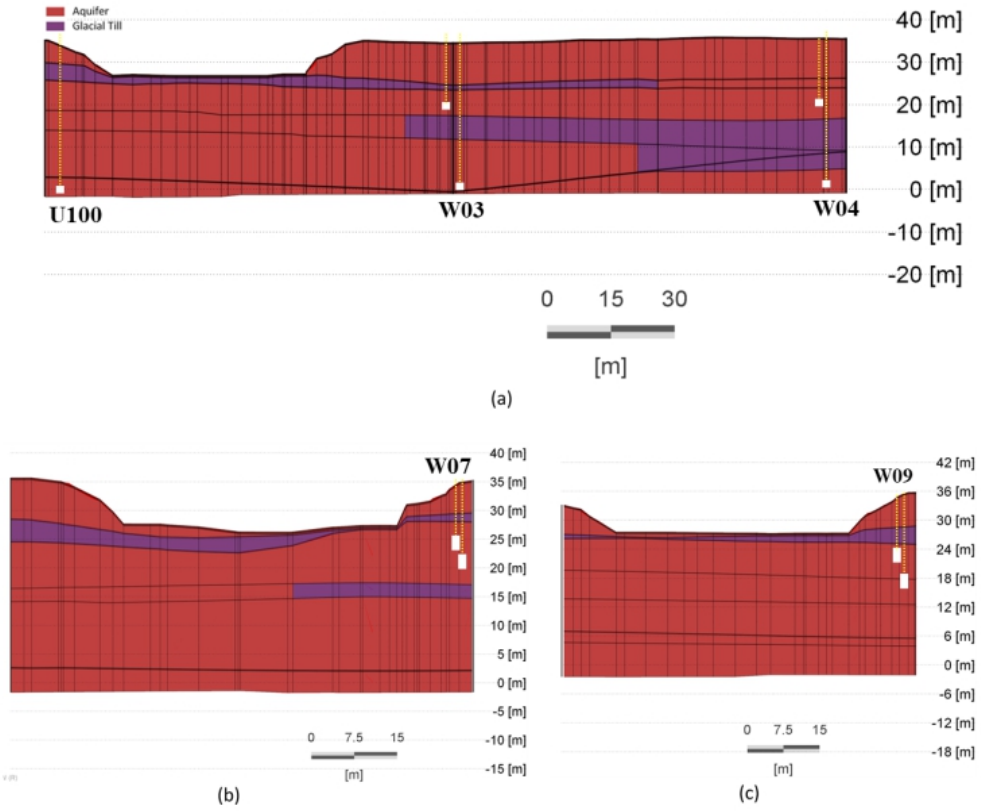

Table S1 Sampling schedule for each of the wells and resulting number of samples for each resultind data set as used in Tab. 3.1 and 3.2. The '+' stands for available water chemistry data and 'X' stands for the available DOC data.

	U100	$W03_{HIGH}$	$W03_{LOW}$	$W04_{HIGH}$	$W04_{LOW}$	$W07_{HIGH}$	$W07_{LOW}$	W08	$W09_{HIGH}$	$W09_{LOW}$	Canal
16/07/2007		X+	X+								
15/08/2007				X+	X+						
15/10/2007		X+	X+								
15/11/2007				X+	X+						
15/01/2008		X+	X+								
18/02/2008				X+	X+						
15/04/2008		X+	X+								
15/05/2008				X+	X+						
15/07/2008		X+	X+								
15/08/2008				X+	X+						
15/10/2008		X+	X+								
18/11/2008				X+	X+						
15/01/2009		X+	X+								
16/02/2009				X+	X+						
16/03/2009											X+
15/04/2009		X+	X+								
15/05/2009				X+	X+						
15/06/2009											X+
15/07/2009		X+	X+								X+
17/08/2009	X+			X+	X+						X+
15/09/2009											X+
15/10/2009		X+	X+								X+

16/11/2009	X+			X+	X+							X+
15/12/2009												X+
14/01/2010		X+	X+									X+
15/02/2010	X+			X+	X+							X+
15/03/2010												X+
15/04/2010		X+	X+									X+
17/05/2010	X+			X+	X+							X+
15/06/2010												X+
15/07/2010		X+	X+									X+
16/08/2010				X+	X+							X+
15/09/2010	X+					X+	X+	X+	X+	X+	X+	X+
18/10/2010		X+	X+									X+
15/11/2010				X+	X+							X+
15/12/2010												X+
17/01/2011												X+
15/03/2011	X+					X+	X+	X+	X+	X+	X+	X+
14/04/2011		X+	X+									X+
13/05/2011				X+	X+							X+
15/06/2011	X+					X+	X+	X+	X+	X+	X+	X+
18/07/2011		X+	X+									X+
15/09/2011	X+					X+	X+	X+	X+	X+	X+	X+
14/10/2011		X+	X+									X+
15/11/2011				X+	X+							X+
16/12/2011												X+
13/01/2012												X+
15/03/2012	X+					X+	X+	X+	X+	X+	X+	X+
16/04/2012		X+	X+									X+
15/05/2012				X+	X+							X+
19/06/2012												X+
16/07/2012												X+
17/09/2012	X+					X+	X+	X+	X+	X+	X+	X+
15/10/2012		X+	X+									X
15/11/2012				X+	X+							X
17/12/2012												X+
15/01/2013												X
13/03/2013	X+					X+	X+	X+	X+	X+	X+	X+
15/04/2013		X+	X+									X
15/05/2013				X+	X+							X
13/06/2013	X+					X+	X+	X+	X+	X+	X+	X+
15/07/2013	X	X+	X+			X	X	X	X	X	X	X
14/08/2013						X	X					
15/08/2013	X			X+	X+					X	X	X
16/08/2013		X							X			
16/09/2013	X+	X				X+	X+	X+	X+	X+	X+	
17/09/2013				X	X							X+
14/10/2013	X	X+	X+	X	X	X	X	X	X	X	X	X
17/11/2013	X	X		X+	X+	X	X	X	X	X	X	X
11/12/2013	X+	X				X+	X+	X+	X+	X+	X+	
12/12/2013				X	X							X+
13/01/2014		X+	X+	X	X	X	X	X	X	X	X	
14/01/2014	X											X
17/02/2014		X				X	X	X	X	X	X	X
18/02/2014	X			X+	X+							
12/03/2014		X				X+	X+	X+	X+			X+
13/03/2014	X+			X	X						X+	
14/04/2014		X+	X+	X	X							X
12/05/2014				X+	X+							X
16/06/2014	X					X	X	X	X	X	X	X
14/07/2014		X	X									X
18/08/2014				X	X							X
15/09/2014	X					X	X	X	X	X	X	X
13/10/2014		X	X									X
17/11/2014				X	X							X
05/10/2015	X+	X+	X+	X+	X+	X+	X+	X+	X+	X+	X+	X+
03/11/2015	X+	X+	X+	X+	X+	X+	X+	X+	X+	X+	X+	X+
15/12/2015		X+	X+	X+	X+	X+	X+	X+	X+			X+
12/01/2016	X+	X+	X+	X+	X+	X+	X+	X+	X+	X+	X+	X+
16/02/2016	X+	X+	X+	X+	X+	X+	X+	X+	X+	X+	X+	X+
15/03/2016	X+	X+	X+	X+	X+	X+	X+	X+	X+	X+	X+	X+
12/04/2016		X+	X+	X+	X+	X+	X+	X+	X+	X+	X+	X+
10/05/2016	X+	X+	X+			X+	X+	X+	X+	X+	X+	X+
14/06/2016		X+	X+	X+		X+	X+	X+	X+	X+	X+	X+
18/07/2016		X+	X+	X+	X+	X+	X+	X+	X+	X+	X+	X+
30/08/2016	X+	X+	X+	X+	X+	X+	X+	X+	X+	X+	X+	X+
04/10/2016			X+	X+	X+	X+	X+	X+	X+		X+	X+
08/11/2016						X+	X+	X+			X+	X+
14/12/2016			X+	X+	X+	X+	X+	X+	X+		X+	X+

18/01/2017			**X+**	**X+**	**X+**	**X+**	**X+**	**X+**		**X+**	**X+**
15/02/2017			**+**	**+**	**+**	**+**	**+**	**+**		**+**	
Tot. X	**30**	**43**	**40**	**44**	**43**	**34**	**34**	**34**	**29**	**33**	**77**
Before Reconst. X	**12**	**20**	**20**	**19**	**19**	**8**	**8**	**8**	**8**	**8**	**45**
After Reconst.X	**18**	**23**	**20**	**25**	**24**	**26**	**26**	**26**	**21**	**25**	**32**
Tot.+	**22**	**35**	**39**	**37**	**36**	**27**	**27**	**27**	**21**	**26**	**58**
Before Reconst. +	**12**	**20**	**20**	**19**	**19**	**8**	**8**	**8**	**8**	**8**	**40**
After Reconst. +	**10**	**15**	**18**	**17**	**16**	**18**	**18**	**18**	**13**	**17**	**18**

Table. S2 The engineering schedule of the canal.

Section	Removal of the old structure	Dredging
Southwest	17/06/2013 - 22/07/2013	22/07/2013 - 13/09/2013
Northeast	30/09/2013 - 11/10/2013	14/10/2013 - 08/11/2013
Northwest	07/11/2013 - 20/11/2013	07/11/2013 - 20/12/2013
Southeast	19/02/2014 - 11/03/2014	05/03/2014 - 19/05/2014